NORTHWESTERN UNIVERSITY

Development of Theranostic and Bioresponsive Small Molecule

Magnetic Resonance Imaging Contrast Agents

A DISSERTATION

SUBMITTED TO THE GRADUATE SCHOOL

IN PARTIAL FULFILLMENT OF THE REQUIREMENTS

for the degree

DOCTOR OF PHILOSOPHY

Department of Chemistry

By

Casey Adams,

EVANSTON, ILLINOIS

March 2022

Abstract

Development of Theranostic and Bioresponsive Small Molecule

Magnetic Resonance Imaging Contrast Agents

Casey Adams

Biomedical imaging is an essential part of medicine that enables the non-invasive observation of biological phenomena. This, in turn, allows for more accurate and earlier diagnoses, monitoring of therapies, and even fundamental research into biological processes. Molecular imaging, a fast-growing subdiscipline of biomedical imaging, seeks to image biochemical processes at the cellular level and beyond. There are a variety of imaging modalities used in molecular imaging, such as fluorescence, positron emission tomography (PET), single photon emission computed tomography (SPECT), computed tomography (CT), and magnetic resonance imaging (MRI), each of which have benefits and drawbacks. MRI is a uniquely powerful imaging modality, as it is safe, has unlimited depth penetration (can image any part of the body), and provides unparalleled soft tissue contrast and anatomical information. However, it suffers from poor sensitivity, and therefore contrast agents are commonly used to enhance the signal. Gd(III) based contrast agents (GBCAs) result in brighter contrast where present and have multiple parameters that affect their relaxivity (i.e. how well they behave as contrast agents). Targeting groups can be added to GBCAs to image biological targets of interest and bioresponsive groups can be added that change the relaxivity of Gd(III) in response to a stimulus, providing a way of imaging biochemical processes. As such, there is a wide variety of ways in which GBCAs can be

used for molecular imaging.

The first two uses of GBCAs described in this thesis (chapters 2 and 3) involve Gd-Pt theranostic agents. Theranostics enable simultaneous imaging and therapy through combining a therapeutic with a diagnostic. In the first case, Gd(III)-Pt(II) theranostics were developed to image chemoresistance to Pt(II) drugs (e.g. cisplatin), which are among the most important cancer therapeutics. By coupling a GBCA to a cisplatin-like moiety, we were able to image agent accumulation differences in chemosensitive and chemoresistant tumors using MRI. Decreased drug accumulation is a hallmark of chemoresistance, therefore this method is a promising first step towards the ability to image Pt(II) chemoresistance. Future work will involve optimizing these Gd(III)-Pt(II) agents and performing more in depth *in vivo* experiments to establish the ability of the agents to predict chemoresistance.

Chapter 3 describes the development of Gd(III)-Pt(IV) theranostic agents. Pt(IV) complexes are commonly used in prodrug strategies because they are non-toxic in the IV oxidation state but can be reduced by biologically relevant reducing agents to an active cytotoxic Pt(II) complex. By coupling a GBCA to a Pt(IV) cisplatin prodrug, we were able to deliver Gd(III) intracellularly, whereas all clinically used GBCAs are limited to the extracellular space. Because the agent releases cisplatin, it was significantly more cytotoxic than the Gd(III)-Pt(II) agents previously described. Therefore, these Gd(III)-Pt(IV) agents are a promising platform for effective tandem chemotherapy and MR imaging. Future work will involve incorporating additional diagnostic and therapeutic moieties onto the Gd(III)-Pt(IV) agents for multimodal imaging and combination therapy.

Chapter 4 describes the development of a Ca(II) responsive GBCA with high cellular uptake and NIR fluorescence capability. The agent increases its relaxivity >100% (at 7 T) in the presence of Ca(II), enabling detection of intracellular Ca(II) flux. A derivative of a NIR fluorescent dye, IR-783, was incorporated to target organic anion transporter polypeptides (OATPs) on cells. We found that the incorporation of IR-783 drastically increased the cellular accumulation of the agent (>10 fmol/cell), resulting in significant intracellular contrast enhancement, especially when Ca(II) flux was induced. *In vivo* experiments imaging neuronal activity in mouse brains are currently underway.

Acknowledgments

My PhD journey at Northwestern University these past four years has undoubtedly been one of the most transformative and developmental times in my life. The adventure began as a cross country trip, cramming my entire life into a Subaru Outback. I had no knowledge of Illinois nor any connections, yet I packed up and headed off to start my new life. I set out with a heart heavy from nostalgia and sadness at leaving my home; however, looking back now, coming to Northwestern was the best decision of my life. It is a surreal feeling to be finishing my PhD, and of course, it feels as though time has flown by. I am filled with thankfulness and appreciation for so many people, and I want to take time to mention those who first come to mind.

Before the plethora of thanks and praise due to many people at Northwestern, I need to thank my amazing mentors in high school and college who guided me down this path. Ms. McCaffrey-Clark, you challenged me when I needed it most and instilled in me a discipline, rigor, and interest in chemistry I rely on to this day. You went above and beyond to help me academically and in my personal life, and I will always look up to you as one of my foundational mentors. Josh Farrell, you first introduced me to bioinorganic chemistry, facilitated so many life-changing opportunities for me beyond Holy Cross (Sandia, MGH), and were instrumental in my decision to attend Northwestern. You told me I would love it here, and you were right! Eszter Boros, working under you at MGH was essential for my development as a scientist and one of my fondest academic experiences. You are a brilliant scientist and a kind and guiding mentor; your enthusiasm for science is infectious, and you provided me with the skills and confidence I needed when entering graduate school. You are a friend and a mentor, and I am eager to see what amazing things you

accomplish as a professor!

There are so many people to thank at Northwestern, but I want to begin with Tom Meade, who has given me a home these past four years and been so instrumental in my PhD journey. Tom, I thank you so much for having full confidence in me, providing me with complete independence to pursue my own original projects, and supporting me in all endeavors both inside and outside the lab. Your kindness and flexibility are unique among PIs, and the environment you have created in lab has allowed me to thrive. Yours was the only lab I really considered joining, and I would not change that decision for anything. To my committee members, Professor Samuel Stupp and Professor Vadim Backman, I thank you for your time, as well as the advice and insight you provided during my qualifying examination and PhD benchmarks.

To the members of the Meade lab, I thank you for making my time at Northwestern truly enjoyable and prosperous. It is rare to have a lab environment where everyone gets along so well, and so much of what I learned came from scientific discussions with each of you. Ruby, thank you for mentoring me in my first year. The work we accomplished together taught me so much and set up the remainder of my graduate research for success. Shaunna, it was a pleasure to share an office with you for three years. I learned so much about inorganic chemistry and MRI through discussions with you, and you always went above and beyond to give feedback on grants, manuscripts, etc. I always enjoyed your sense of humor, and you made lab a place I enjoyed coming to. Hao, I thank you for being a great friend and inspiring me as a scientist. You are one of the most gifted researchers I have worked with. Brainstorming ideas with you and defending them against your bombardments of questions challenged me to be the best I can be. Beyond science, your infectious laugh and outgoing personality always made the lab a brighter place. Meghan and Megan, I could

not have asked for better classmates to join the Meade lab with. It has been a pleasure to take this journey with you both and grow as scientists and adults (yikes) together! Special thanks to Meghan Dukes for taking over many of the responsibilities for organizing lab events—it is much appreciated! Chris, thank you for your help with bio related techniques and technology related questions over the years; I wish you all the best in your postdoc position. Andrew, thank you for your never-ending willingness to help with any lab related task. You have literally kept the lab running at times and I appreciate that very much! Hyun, Matt, and Jian, it has been great to get to know you these past couple of months, and I wish you all the best in the Meade lab and beyond.

I also want to thank some of the great organizations at Northwestern that have helped me develop outside of science and made my experience here so rich and diverse. Thank you to INVO and the wonderful people I worked with (Sonia Kim, Sarah Kamper, etc.) for providing me with an invaluable internship experience in technology transfer. Thank you also to the Kellogg School of Management and the Management for Scientists and Engineers program. I am blown away by the number of amazing opportunities at Northwestern, and the ones I was fortunate enough to participate in made my experience here so much more valuable.

Finally, I want to thank my family, both immediate and extended, who have shown constant support these past four years and beyond. Mom, you have expressed a genuine interest in my research from the very beginning, striving to understand it with no scientific background and remembering details of my projects I had even forgotten! You have helped me in so many distinct ways in graduate school, and I am truly thankful. Sam, you likewise have consistently helped me and offered advice on problems big and small. You are both amazing, accomplished women who have inspired me and showed me how to succeed through example. Dad, it was always an ego

boost to hear "wow, how the hell did you come up with that?" You always said I got my scientific mind from you (debatable), and you would have made a fine scientist in a different life. Nan, nothing makes me happier than hearing the pride and love in your voice when I tell you about my accomplishments. I love you all and thank you for the support!

List of Abbreviations

General

CA ....Contrast agent

CNR ....Contrast-to-noise ratio

CT ....Computed tomography

EPR ....Enhanced permeability and retention

eq or equiv..................Equivalents

ESI.............................Electrospray ionization

FBS ....Fetal bovine serum

FL...............................Fluorescence

FOV............................Field of view

FT...............................Fourier transform

GBCA ....Gd(III)-based contrast agent

HPLC ....High-performance liquid chromatography

HR-MS ....High resolution mass spectrometry

ICP-MS ....Inductively coupled plasma mass spectrometry

IP................................Intraperitoneal

IR................................Infrared

IS ....Inner-sphere

IV ....Intravenous

LG ....Leaving group

MEM ....Minimum essential media

MR ....Magnetic resonance

MRI...........................Magnetic resonance imaging

MS.............................Mass spectrometry

NIR............................Near infrared region

NMR ....Nuclear magnetic resonance

NMRD........................Nuclear magnetic relaxation dispersion

NSF ....Nephrogenic systemic fibrosis

OS ....Outer Sphere

PET ....Positron emission tomography

PG ....Protecting group

PRE ....Paramagnetic relaxation enhancement

RARE.........................Rapid acquisition rapid echo

RDS...........................Rate-determining step

RF..............................Radio frequency

RPMI.........................Roswell Park Memorial Institute Medium

RT. ....Room temperature

SBM ....Solomon, Bloembergen, and Morgan

SPECT.......................Single-photon emission computed tomography

TLC ....Thin layer chromatography

TE..............................Echo time

TR ....Repetition time

UV.............................Ultraviolet

UV-Vis........................Ultraviolet-Visible

ZFS............................Zero field splitting

Chemicals

ACN ....Acetonitrile

$AgNO_3$........................Silver nitrate

Ag_2O ....Silver oxide

BBr_3............................Boron tribromide

β-gal ....Beta-galactosidase

$CDCl_3$.........................Deuterated chloroform

CDI.............................Carbonyldiimidazole

CD_3OD........................Deuterated methanol

CHAPS......................(3-((3-Cholamidopropyl) dimethylammonio)-1-propanesulfonate)

$CHCl_3$.........................Chloroform

Cs_2CO_3 ....Cesium carbonate

$CuSO_4.5H_2O$ ....Copper(II) sulfate pentahydrate

DCM ....Dichloromethane

DIPEA........................*N,N*-Diisopropylethylamine

DMEM ....Dulbecco's modified eagle medium

DMF...........................Dimethylformamide

DMSO........................Dimethyl sulfoxide

D_2O ....Deuterated water

DO3A.........................1,4,7,10-Tetraazacyclododecane-1,4,7-trisacetic acid

DOTA ....1,4,7,10-Tetraazacyclododecane-1,4,7,10-tetracetic acid

DPBS.........................Dulbecco′s phosphate buffered saline

DTT...........................Dithiothreitol

EDC...........................1-Ethyl-3-(3-dimethylaminopropyl)carbodiimide hydrochloride

Et$_2$O...........................Diethyl ether

EtOAc/EA ....Ethyl acetate

EtOH ....Ethanol

FA ....Formic acid

GSH........................... Glutathione

GdCl$_3$ ....Gadolinium(III) chloride

HCl............................Hydrochloric acid

HEPES ....2-[4-(2-Hydroxyethyl)piperazin-1-yl]ethanesulfonic acid

HNO$_3$.........................Nitric acid

H$_2$O ....Water

H$_2$O$_2$ ....Hydrogen peroxide

KBr............................Potassium bromide

K$_2$CO$_3$ ....Potassium carbonate

KI ....Potassium iodide

KOH...........................Potassium hydroxide

Ln(III) ....Lanthanide (III) ion

MeCN........................Acetonitrile

MeOH ....Methanol

NaBH$_4$........................Sodium borohydride

NaCl ....Sodium chloride

Na$_2$CO$_3$........................Sodium carbonate

NaHCO$_3$........................Sodium bicarbonate

Na$_2$SO$_4$........................Sodium sulfate

NaI........................Sodium iodide

NaOH ....Sodium hydroxide

NaOMe........................Sodium methoxide

Na$_2$SO$_4$........................Sodium sulfate

NH$_4$Cl........................Ammonium chloride

NH$_4$OH........................Ammonium hydroxide

NHS........................N-hydroxysuccinimide

PBr$_3$........................Phosphorus tribromide

PBS ....Phosphate buffered saline

PPh$_3$........................Triphenylphosphine

TEA........................Triethylamine

TFA........................Trifluoroacetic acid

THF........................Tetrahydrofuran

TIPS ....Triisopropylsilane

Tris ....2-Amino-2-(hydroxymethyl)propane-1,3-diol

Units

°C ....degrees Celsius

AU..............................absorbance units

Å................................angstroms

cm..............................centimeters

cm^{-1} ....wavenumbers

g.................................grams

hr ....hours

K.................................Kelvin

M................................molar

mA.............................milliamperes

mg ....milligrams

MHz ....megahertz

MΩ.............................megaohm

m ....meters

mg ....milligrams

min ....minutes

mL..............................milliliters

mM.............................millimolar

mm ....millimeters

mmol ....millimoles

mol ....moles

ms ....milliseconds

mV ....millivolts

ng ....nanograms

nM ....nanomolar

nm ....nanometers

ns ....nanoseconds

ppb ....parts per billion

ppm ....parts per million

ps ....picoseconds

psi ....pound per square inch

s ....seconds

T ....Tesla

V ....volts

µg ....micrograms

µL ....microliters

µM ....micromolar

µm ....micrometers

µs ....microsecond

Symbols

B_0 ....external magnetic field

D ....diffusion coefficient

IC_{50} ....half maximal inhibition concentration

J ....coupling constant

K ....binding constant

K_d ....dissociation constant

k_{ex} ....exchange rate

M ....net magnetization vector

q ....water coordination number

r_1 ....longitudinal relaxivity

r_2 ....transverse relaxivity

S ....spin

T_1 ....longitudinal (spin-lattice) relaxation time

T_{1e} ....longitudinal electronic relaxation time

T_{1m} ....longitudinal relaxation time of bound water

T_2 ....transverse (spin-spin) relaxation time

$1/T_1$ ....longitudinal relaxation rate

$1/T_{1,d}$ ....diamagnetic component of the longitudinal relaxation rate

$1/T_{1,obs}$ ....observed longitudinal relaxation rate

$(1/T_{1,p})^{IS}$ ....inner-sphere paramagnetic component of the longitudinal relaxation rate

γ ....gyromagnetic ratio

Δr_1 ....change in longitudinal relaxivity

Δ_t ....trace of the zero field splitting tensor

ε ....molar extinction coefficient

λ..................................wavelength

τ_c..................................total correlation time of dipole-dipole relaxation

τ_m..................................mean residence lifetime of bound water

τ_R..................................rotational correlation time

Δ_v..................................correlation time for the modulation of zero field splitting

ω..................................Larmor frequency

Φ..................................fluorescence quantum yield

ω_0...................................Larmor frequency of water

Table of Contents

List of Figures

List of Schemes

List of Tables

CHAPTER 1

Introduction & Background

1.1 Introduction

At the most fundamental level, biomedical imaging enables the noninvasive observation of biological phenomena. The importance of being able to visualize the inner workings of the body cannot be overstated. Modern biomedical imaging techniques are essential in modern medicine; they allow clinicians to detect and diagnose diseases earlier and more accurately and monitor the progress of treatment, all of which significantly improve patient prognoses.

Molecular imaging, which aims to visualize specific biochemical processes in the body in real time, is a rapidly advancing and exciting subdiscipline of biomedical imaging with enormous potential. Molecular imaging has the potential to provide detailed insights into complex biological pathways and disease mechanisms in a living organism. As such, the information gathered from molecular imaging can advance our diagnostic capabilities, aid in drug discovery, enable personalized and precision medicine, track therapies, and discover biochemical interactions and pathways hitherto unknown.[1-4]

There are a wide variety of biomedical imaging modalities that are used for molecular imaging, each of which have strengths and weaknesses. Most imaging modalities rely on contrast agents, which, as the name suggests, provides the signal that is detected. In molecular imaging, the contrast agent is typically designed to target or interact with something of biological interest to provide information about it in real time. Two of the most important aspects of a given imaging modality are sensitivity and depth penetration. Sensitivity relates to how easily a signal can be detected; in short, a more sensitive modality requires less signal to be detectable. Depth penetration relates to how readily the signal can pass through biological media. Depth penetration affects the resolution of images, and in many cases, hinders detection of the signal entirely. These two factors,

among others, are essential to understand when determining which imaging modality is best for a given task.[1]

Table 1.1. Summary of discussed molecular imaging modalities (modified from ref 1).

Modality	Spatial Resolution	Sensitivity	Benefits	Limitations
Fluorescence	<1 µm *in vitro* 2-3 mm *in vivo* (preclinical)	10^{-9}-10^{-12} M	Cheap, ubiquitous, good safety profile	Low depth penetration (limited clinical utility)
PET/SPECT	1-2 mm (preclinical) 5-10 mm (clinical)	10^{-10}-10^{-12} M	Unlimited depth penetration	Ionizing radiation, costly, no anatomical information
CT	50-200 µm (preclinical) 0.5-1 mm (clinical)	Not determined	Unlimited depth penetration, ubiquitous in clinic	Ionizing radiation, limited molecular imaging utility
MRI	25-100 µm (preclinical) 1 mm (clinical)	10^{-5}-10^{-3} M	Unlimited depth penetration, no ionizing radiation, best in class soft tissue contrast	Low sensitivity, long image acquisition times, expensive

1.2 Optical Fluorescence Imaging

Optical imaging (fluorescence being the most common type) utilizes the luminescent properties of certain molecules, termed fluorophores. Fluorophores work by absorbing light of a certain wavelength (dependent on the specific fluorophore) and subsequently releasing light at a different wavelength. Fluorescence imaging is one of the most common imaging modalities for

molecular imaging and has seen widespread use in *in vitro* and preclinical *in vivo* settings.[5-6]

Fluorescence imaging is so commonly used for a few reasons. First, there are countless fluorescent moieties that exist. With such a broad scope of available compounds, it is possible to select a fluorophore for nearly any purpose. Furthermore, fluorophores can be drastically affected by subtle chemical modifications, enabling the design of bioresponsive fluorophores that change fluorescent properties in response to a biological stimulus. Finally, Fluorescence imaging has excellent sensitivity, with fluorophore concentrations in the nanomolar (10^{-9} M) to picomolar (10^{-12} M) range detectable.[1] With such excellent sensitivity, fluorophores can be used to visualize biological targets that are not present in high amount. As such, it is no surprise that fluorescence imaging is the gold standard imaging modality for *in vitro* cell work. In the cellular setting of confocal microscopy, fluorescence imaging has excellent spatial resolution, with sub-micron resolution possible (diffraction limited to about ~200 nm).[7] This enables detailed images of subcellular structures, which is extraordinarily useful in the study of structural biology and biochemical processes.

However, the limitations of fluorescence imaging become apparent when *in vivo* settings are considered. One of the most significant drawbacks of fluorescence imaging is its limited depth penetration. Light in the UV-Vis range does not penetrate well through biological tissue (limited to <1 cm), which significantly limits its utility in imaging animals, and makes non-invasive imaging in humans impossible. Even if the light can penetrate through tissue, it severely affects the spatial resolution (2-3 mm).[1] To help overcome this issue, researchers have developed fluorophores that emit at longer wavelengths, such as the near infrared region (NIR).[8] NIR light penetrates through tissue better, and as such, have enabled fluorescence imaging in many

preclinical experiments, such as those in mice.[9] Though non-invasive fluorescence imaging in humans is far-fetched, fluorophores have seen use in a few areas in the clinic, such as fluorescence-guided surgery.[10] Fluorescence guided surgery uses a fluorophore to target tissue that is intended to be resected; the fluorescence signal helps the surgeon visualize what tissue should be removed. Thus, though fluorescence imaging is most useful in the *in vitro* realm, unique uses in the clinic are emerging.

1.3 Nuclear Imaging Techniques

Nuclear imaging techniques, such as positron emission tomography (PET) and single photon emission computed tomography (SPECT), utilize electromagnetic radiation released from radioactive nuclei. Both PET and SPECT radiotracers ultimately release high energy gamma ray radiation, albeit through different mechanisms. While SPECT radiotracers (^{123}I, ^{99m}Tc, ^{133}Xe, ^{111}In, etc.) directly release a single photon of gamma radiation, PET radiotracers (^{18}F, ^{11}C, ^{64}Cu, ^{68}Ga, etc.) first emit a positron.[11] The positron, which is the antiparticle of an electron, undergoes an annihilation event when it collides with an electron, which produces two gamma ray photons 180° apart.

Both PET and SPECT utilize gamma radiation, which is sufficiently energetic to penetrate through biological tissue in humans. This unlimited depth penetration means both modalities are relevant for biomedical imaging in the clinic. There are FDA approved PET and SPECT radiotracers commonly used, such as ^{18}F-fluorodeoxyglucose (FDG), which is a common PET radiotracer for cancer imaging.[12] In addition to the outstanding depth penetration, PET and SPECT have excellent sensitivity (10^{-10}–10^{-12} M).[1] With the ability to be detected at very low

concentrations anywhere in the body, nuclear radiotracers have an impressive scope of possible uses in molecular imaging. Additionally, each specific radiotracer has a distinct half-life, therefore the radiotracer used can be selected to match the indication. For example, immunoPET imaging uses long lived positron emitters such as ^{89}Zr ($t_{1/2}$ of ~3 days) to match the long half-lives of antibodies.[13]

Despite the beneficial aspects and clinical promise of nuclear techniques, they do have several limitations. First, the excellent depth penetration comes at the cost of using harmful ionizing radiation. Though only small quantities of radiotracer are necessary, repeat exposure to gamma radiation is a significant safety concern. As such, there are questions about the ability to monitor diseases long-term using nuclear techniques. Second, both techniques have poor spatial resolution and lack any anatomical information. As such, they can be coupled with a second imaging modality (MRI or CT) to provide anatomical information that contextualizes the PET or SPECT signal.[14] Third, the cost of PET and SPECT imaging is higher than most other imaging modalities.[1] Not only are the scanners expensive, but the radioactive material can be a bottleneck as well. For instance, short lived isotopes such as ^{11}C require an onsite cyclotron. Because of the high cost, PET and SPECT are not yet ubiquitous in the clinic. Still, the versatility of nuclear techniques and ability to image nearly any molecular target in the body make them essential molecular imaging tools.

1.4 Computed Tomography

Unlike nuclear techniques, computed tomography (CT) provides detailed anatomical images. CT uses x-rays to take a series of images at different angles, which are then compiled into

cross-sectional slices that, when combined, provide 3D images. Because x-rays attenuate differently depending on the density of the tissue they pass through, different tissue types will have different contrast in a CT image. As such, CT can provide detailed anatomical information on a variety of different tissue types and is useful for imaging nearly any part of the body.[1,3] CT is used extensively in the clinic for a variety of purposes, such as brain imaging, detection of tumors, detection of clots, etc. Especially dense tissue, such as bones, appear very bright on a CT image because they attenuate x-rays to a high degree, and as such, it is an excellent modality for visualizing bone abnormalities. Contrast agents can be used to enhance the observed contrast in CT images. CT contrast agents are compounds that block x-rays from passing through, thus increasing the contrast where they are present.[15] Iodine-based compounds are typically injected into the blood and used to image blood vessels while barium-based compounds are used orally to image the GI tract.

Like PET and SPECT, CT uses ionizing radiation (x-rays), and therefore there are safety concerns related to regular CT imaging of a patient.[1] Though CT imaging is an undeniably indispensable imaging technique in the clinic, it is not used as frequently for molecular imaging or imaging in the preclinical setting, perhaps due to the restrictions on CT contrast agents (i.e. they must be heavy elements with high electron density).

1.5 Magnetic Resonance Imaging

Magnetic resonance imaging (MRI) is unique among the other imaging modalities discussed and has several benefits that make it one of the most powerful and commonly used biomedical imaging techniques. MRI operates on the same principle as nuclear magnetic resonance

(NMR). In short, a sample is placed in a strong external magnetic field (B_0) such that spin active nuclei (^1H in the vast majority of cases of MRI) align with or against the magnetic field. Alignment with the external magnetic field is slightly energetically favorable, resulting in a net magnetization vector (M_0) that is aligned with the external magnetic field (Figure 1.1.) Radio frequency pulses are applied that knock the net magnetization vector out of alignment with the external magnetic field. The excited nuclei that have been knocked out of alignment subsequently relax through two mechanisms: T_1 (longitudinal) relaxation, which is the time it takes for M_0 to regrow in the direction of B_0, and T_2 (transverse) relaxation, which is the time it takes for the net magnetization in the XY plane (i.e. the magnetization that resulted from M_0 being knocked out of alignment with B_0) to return to zero.[16-17]

The signal detected is proportional to how quickly the excited nuclei relax back to equilibrium, which in turn is affected by the environment the nuclei are in. Most MR imaging deals with ^1H nuclei (protons), which are ubiquitous in all tissues and water in the body. The ^1H nuclei in different tissues (muscle, fat, brain, etc.) are in very different environments, and therefore have distinct relaxation properties. This results in inherent contrast differences between different biological tissue types, which provides MRI with excellent soft tissue contrast and anatomical information. Additionally, there are no safety concerns with MRI (without contrast agent) because radio frequency is used. Radio frequency also has limitless depth penetration, making MRI very well suited for clinical imaging.[1]

The main drawback of MRI as a molecular imaging modality is its low sensitivity. Because tissue has endogenous contrast in MRI (i.e. a contrast agent does not produce the signal) the background signal is very high when imaging a specific target. Furthermore, because the energy

difference between parallel and antiparallel alignment with B_0 is very small, M_0 is smaller than it otherwise would be. Therefore, the signal from one cycle of excitation and relaxation is quite small, and many scans must be acquired to obtain a suitable image. As such, image acquisition time of MRI is longer than the other imaging modalities discussed.[1, 16-17]

To increase the utility of MRI as a molecular imaging modality, contrast agents can be employed to increase the relaxation rate (T_1 or T_2) of excited nuclei, ultimately enhancing the contrast where the agent is present. Gadolinium (Gd(III)) is a commonly used T_1-weighted contrast agent, meaning it increases the T_1 relaxation rate (lowers the relaxation time), resulting in brighter contrast in a T_1-weighted image.[16-17] Gd(III)-based contrast agents (GBCAs) will be discussed in greater detail in subsequent sections. T_2 contrast agents increase the T_2 relaxation rate, resulting in darker contrast in T_2-weighted images. Superparamagnetic iron oxide nanoparticles (SPIONS) are common T_2 contrast agents. Because of the low sensitivity of MRI, contrast agent concentrations in the high micromolar to millimolar (10^{-5}-10^{-3} M) are necessary to significantly enhance the observed contrast.[1] This is a significant limitation, yet there are many ways in which MRI contrast agents can report on biological processes and phenomena.

T_1 (longitudinal) relaxation

T_2 (transverse) relaxation
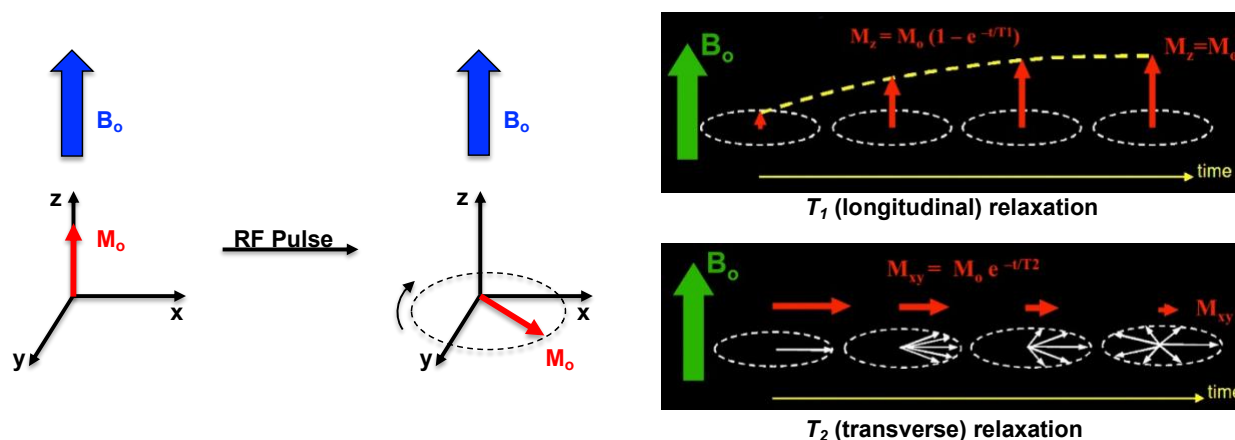
Scheme 1.1. Depiction of the process that occurs during MRI. Spin active nuclei (most typically ^{1}H) will align with an applied external magnetic field (B_0) such that there is a net magnetization vector (M_0) aligned with B_0 (termed the Z direction). When radiofrequency (RF) pulses are applied, M_0 gets knocked out of alignment with B_0. The excited ^{1}H nuclei then relax back to equilibrium through two mechanisms, T_1 and T_2, where T_1 is the time it takes for M_0 to regrow in the Z direction and T_2 is the time it takes for the net magnetization in the XY plane to return to zero. This process is repeated during image acquisition in MRI. (T_1 and T_2 relaxation pictures from mriquestions.com).

1.6 Gd(III)-Based MRI Contrast Agents (GBCAs)

Gd(III)-based contrast agents (GBCAs) are very commonly used tools in ^{1}H MRI. Nearly 40% of all clinical MRI scans employ a GBCA to enhance the contrast of an area of interest.[16-17] Gd(III) works as a contrast agent by increasing the relaxation rate of excited ^{1}H nuclei. Gd(III) is ideally suited to this role because of its unique electronic and magnetic properties. Gd(III) has a half-filled 4f subshell, making it highly paramagnetic with the largest stable spin (S=7/2) and giving it a symmetric S state that results in a slow electronic relaxation time (T_{1e}).[16-17] The T_{1e} of Gd(III) is well in tune (on the same order of magnitude, depending on the magnetic field strength) with the Larmor frequency of protons, which is the frequency at which protons precess around the applied external magnetic field.[16-17] As a result, Gd(III) is well suited to facilitate energy transfer from the excited protons, which increases their T_1 relaxation rate. This is observed as brighter contrast in a T_1-weighted image wherever the Gd(III) is present.

Free Gd(III) ions that are not coordinated by an organic ligand are toxic in biological systems. As such, it is necessary to form a stable (thermodynamically and kinetically) complex so that the Gd(III) does not interfere with biological processes and cause toxic side effects.[16-17] There are several GBCAs that are approved for clinical use by the FDA (Figure 1.2.) Each of these FDA approved agents are based on octadentate (eight-coordinate) ligands that allow one water molecule

to bind directly to the Gd(III) ion.[17] The ligands are either linear and based on diethylenetriamine pentaacetate (DTPA) or macrocyclic with three acetic acid arms (DO3A) or four (DOTA). DTPA and DO3A/DOTA based ligands bind Gd(III) to form highly thermodynamically stable and kinetically inert complexes. However, in recent years, concerns about Gd(III) dissociating from its ligand in the body have been raised.[18-19] Of note, some patients developed nephrogenic systemic fibrosis (NSF). Further analysis showed that three agents (Magnevist, Omniscan, and Optimark), all of which use a linear ligand, were associated with increased chances of developing NSF; however, this only occurs after repeat exposure in patients with severely compromised kidney function (pre-existing kidney failure). Because of the association between linear complexes and NSF, as well as the increased stability of macrocyclic complexes compared to their linear analogues (macrocyclic effect), there has been a strong trend towards the exclusive use of macrocyclic GBCAs.

More recently, data has shown that patients with repeat contrast enhanced MR scans can have detectable amounts of Gd(III) remain in their bodies, including in the brain, for months or years after imaging.[20-21] Gd(III) retention in the body has not yet been linked to any adverse health effects in patients with normal kidney function, yet this observation prompted the FDA to issue a warning. Still, GBCAs (especially macrocyclic ones) are considered very safe, with severe adverse events observed in only 1 in every 40,000 injections.[22] As such, the FDA asserts their benefits continue to outweigh any potential risks.

The safety concerns of GBCAs, though minimal, have spurred research into developing T_1 contrast agents that use paramagnetic ions other than Gd(III), such as Mn(II) and Fe(III).[23-29] Iron and manganese are naturally present in biological systems, therefore researchers suggest CAs

using these paramagnetic ions may be safer alternatives. Although Gd(III) is typically a more efficient CA compared to Fe(III) and Mn(II), certain complexes have been developed that have relaxivities comparable to clinically used GBCAs.[23-25] Additionally, Fe(III) and Mn(II) are both redox active, whereas Gd(III) is not under any reasonable conditions, thus opening the door for redox mediated molecular imaging probes.[23-29] Though GBCAs will likely remain the gold-standard for clinical use, it is likely research into alternative contrast agents will continue to increase in the coming years.

Gd-DOTA
(Dotarem)

Gd-HP-DO3A
(ProHance)

Gd-DO3A-butrol
(Gadavist)

Gd-DTPA
(Magnevist)

Gd-DTPA-BMA
(Omniscan)

Gd-DTPA-BMEA
(Optimark)

Gd-BOPTA
(Multihance)

MS-325
(Ablavar)

Gd-EOB-DTPA
(Eovist)
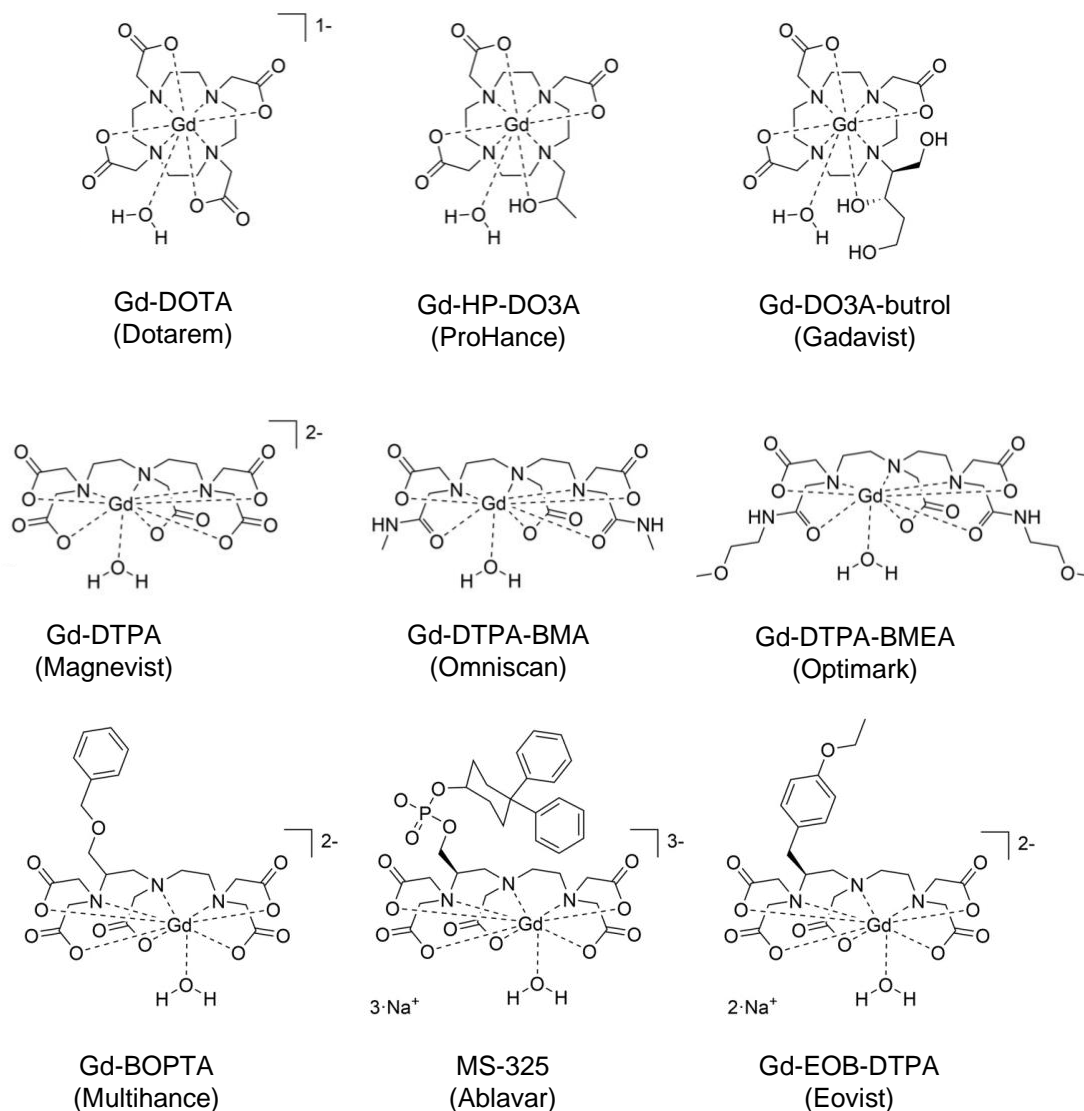
Figure 1.1. FDA approved Gd(III)-based contrast agents (GBCAs). All approved contrast agents are based on the linear ligand, DTPA, or macrocyclic ligands, DO3A or DOTA. All FDA approved GBCAs are octadentate with one inner sphere water bound. Figure modified from reference 17.

1.7 Relaxation Theory of GBCAs

In MRI, ^{1}H nuclei have an intrinsic relaxation time (T_1 and T_2), which is the basis of the diamagnetic portion of the observed signal. The intrinsic T_1 and T_2 of a proton depends on the environment it is in, which ultimately results in contrast differences in distinct tissues in the body without the use of an exogenous contrast agent. When an exogenous contrast agent is used, such as a GBCA, the paramagnetic ion generates fluctuating magnetic fields through Brownian motion, which speeds up the relaxation rate of nearby protons. This increase in relaxation rate due to the contrast agent is known as paramagnetic relaxation enhancement (PRE).[16-17]

There are a number of factors that contribute to the PRE effect that a GBCA has on protons, many of which can be altered through chemical modification or biochemical interaction of the Gd(III) complex. This is the basis for developing bioresponsive MR contrast agents.[16] Since GBCAs are rarely used as T_2 contrast agents, this discussion will focus exclusively on T_1 relaxation.

The typical measure the effectiveness of a contrast agent is T_1 relaxivity (r_1). Relaxivity is the slope of the line of a plot of $1/T_1$ (R_1 or relaxation rate) vs. concentration of the contrast agent. In short, a higher relaxivity contrast agent is one that more efficiently increases the relaxation rate of protons, resulting in a higher PRE and brighter observed MR contrast. As equation 1.1 shows, the observed relaxation rate can be increased by either increasing the relaxivity or the concentration of the contrast agent. Equation 1.2 shows that the relaxivity of a contrast agent is broken into an inner sphere portion and outer sphere portion, the contributions of each are ~50% of the total PRE. There are several parameters that affect the inner sphere portion of relaxivity. The number of water molecules directly bound to Gd(III) (q) is directly proportional to relaxivity (Eq 1.3.) In other

words, relaxivity increases as more water can directly bind to Gd(III). Additionally, relaxivity is maximized when the dipole-dipole relaxation correlation time (τ_c) is equal to the inverse Larmor frequency of water protons. Equation 1.4 shows three key parameters that affect τ_c: τ_R (the rotational correlation time), τ_m (water residency time), and T_{1e} (electronic relaxation time of Gd(III)). The Larmor frequency of protons is dependent on the external magnetic field strength, therefore different parameters dominate relaxivity at low field strength (0.5-3 T) and high field strength (7-9.4 T). Figure 1.2 shows the different water coordination spheres of a small molecule GBCA as well as some of the key parameters discussed. Each of these parameters, and how they are used to develop bioresponsive GBCAs, will now be discussed in greater detail.[16-17]

$$\frac{1}{T_{1,obs}} = \frac{1}{T_{1,d}} + \boldsymbol{r_1}[\text{Gd(III)}] \qquad \text{Eq. 1.1}$$

$$r_1 = r_1^{OS} + r_1^{IS} \qquad \text{Eq. 1.2}$$

$$r_1^{IS} = \frac{q/[\text{H}_2\text{O}]}{T_{1m} + \tau_m} \qquad \text{Eq. 1.3}$$

$$\frac{1}{\tau_c} = \frac{1}{\tau_R} + \frac{1}{\tau_m} + \frac{1}{T_{1e}} \qquad \text{Eq. 1.4}$$

q: # of bound water τ_R : Rotational correlation time τ_m : Water residency time T_{1e} : Electronic relaxtion time of Gd(III)
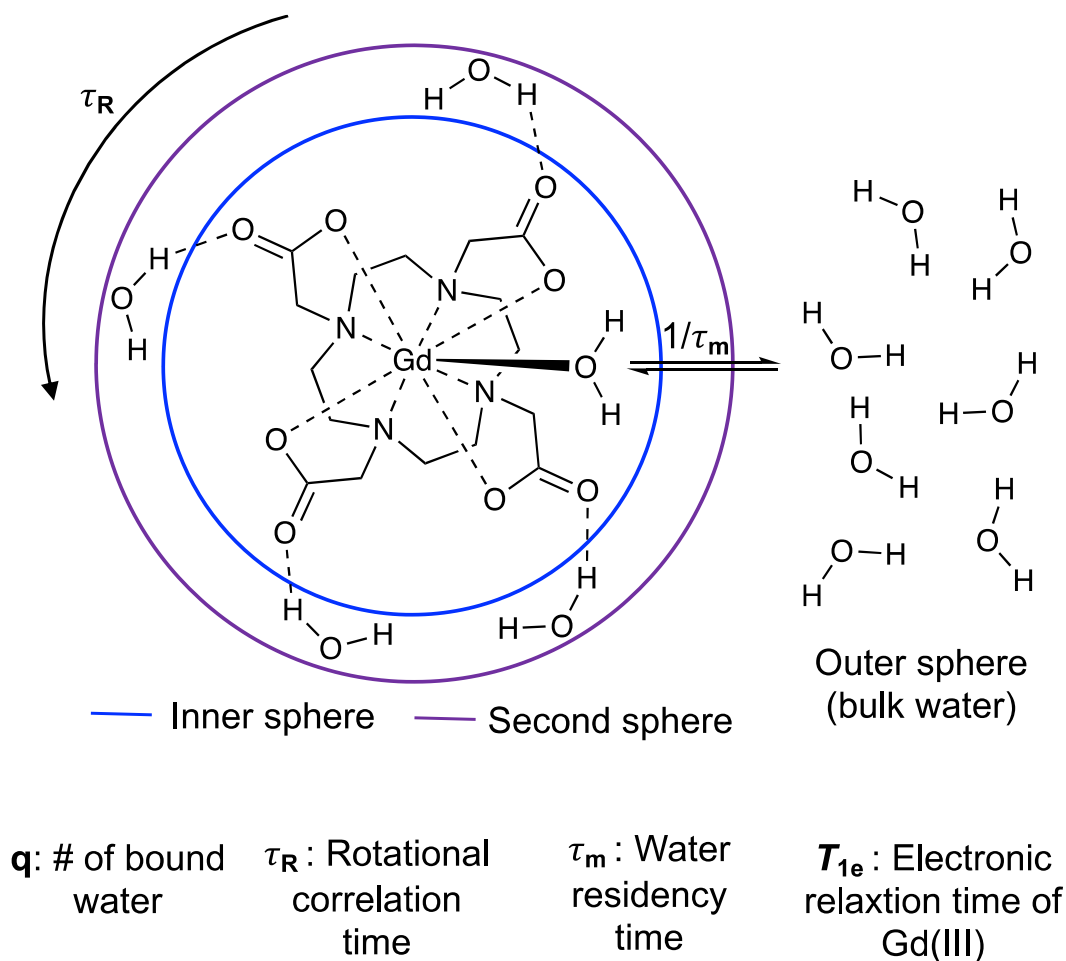
Figure 1.2. Different water coordination spheres of a small molecule GBCA and some of the key parameters affecting relaxivity. Inner sphere (IS) water bound directly to Gd(III) is q, and relaxivity is directly proportional to this parameter. Second sphere water refers to water hydrogen bonded to the complex but not directly coordinated to Gd(III). τ_R is the rotational correlation time of the complex, which is related to how fast it rotates in solution. T_m is the water residency time, which is related to how fast the bound water exchanges with the bulk water. T_{1e} is the electronic relaxation time of Gd(III), which affects all coordination spheres and is dependent on magnetic field strength. In total, inner sphere contributions contribute about 50% of the total relaxivity.

Hydration number (q) and q-modulated activatable agents:

The hydration number, the number of water molecules directly bound to Gd(III), is directly proportional to the inner sphere relaxivity. As previously stated, all FDA approved GBCAs are q

of 1, and they have relaxivities between 3.5-5.5 mM^{-1}s^{-1} at 1.5 T.[16-17] If q is increased, the relaxivity increases in a linear fashion; however, increasing q comes at the cost of decreasing the denticity of the ligand, resulting in a less stable complex. Therefore, q values greater than 2 are not commonly seen. The hydration number provides a straightforward means of developing activatable GBCAs at any magnetic field strength. q-modulated GBCAs start with a low hydration number, usually q=0, due to an extra chemical group ("arm") that binds to Gd(III) and blocks water coordination. The arm is designed to respond to or interact with some sort of biological stimulus (enzyme, ion, etc.) such that it no longer binds Gd(III) and opens up one or more water coordination sites to increase q to 1 or 2 (Scheme 1.2.) The increase in relaxivity going from the "off" to "on" states provides a readout of the biological activity that occurred. However, because inner sphere contributions are only ~50% of the total relaxivity, the "off" state of a q-modulated agent is never truly off. As such, it can be difficult to tease out high concentrations of "off" agent vs. activation of the agent to its brighter "on" state. Nevertheless, it is a powerful strategy for developing activatable GBCAs because it can be used regardless of magnetic field strength, and therefore is relevant for clinical and preclinical applications alike. Over the past two decades, q-modulated agents have been developed that report on Ca^2 flux, reporter genes for gene therapy, pH, Zn^{2+}, K^+, $Cu^{1+/2+}$, Fe^{2+}, and redox activity.[30-34]
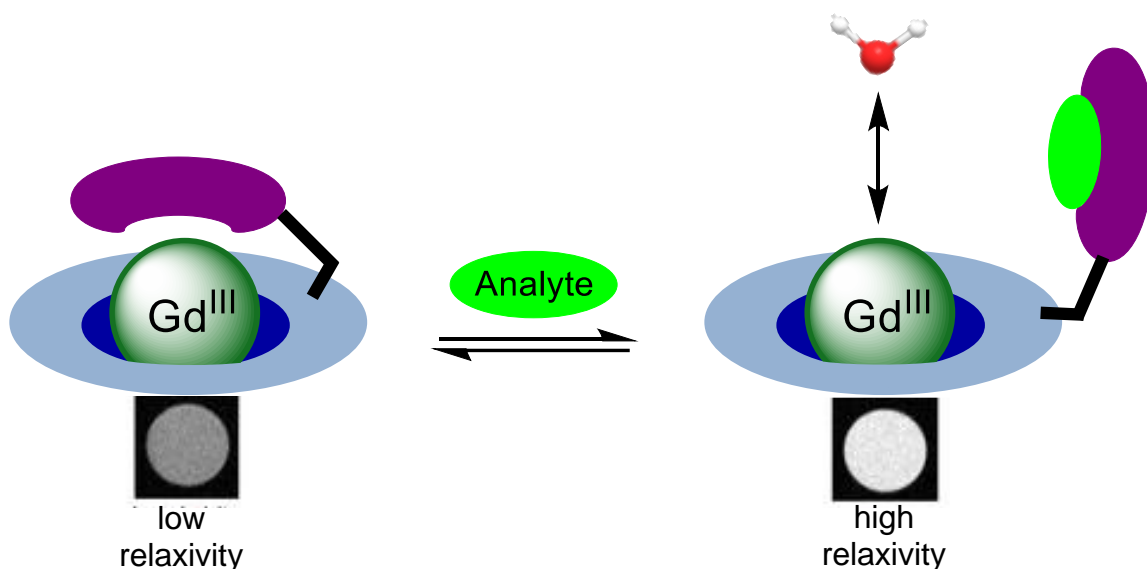
Scheme 1.2 Depiction of how q-modulated activatable GBCAs work. Initially, a chemical group binds to Gd(III), blocking water coordination (q=0) and resulting in a low relaxivity "off" state. The chemical group then interacts with some biological analyte of interest such that it no longer binds Gd(III), opening up one or more water coordination sites (q=1 or 2) and resulting in a higher relaxivity "on" state.

Water residency time (τ_m):

   The water that is directly bound to Gd(III) exchanges rapidly with the bulk water, imparting the strong PRE effect to the surrounding area. Typical small molecule GBCAs have a τ_m of ~100 ns (~10 million water molecules exchanged per second). The ligand of the GBCA can be designed to change τ_m, and indeed research has been done to "optimize" τ_m. For example, researchers have designed Gd-DTPA derivatives with substituted ligand backbones that affect the water exchange rate.[35] However, τ_m is a difficult parameter to use as a bioactivatable strategy, and it is sufficiently fast for small molecule agents where it is not the limiting factor of relaxivity at relevant magnetic field strengths.

Rotational correlation time (τ_R) and τ_R-modulated agents:

The rotational correlation time (τ_R) is related to how fast the Gd(III) complex rotates in solution. For most small molecule GBCAs, the τ_R is ~0.1 ns, which is very fast compared to other parameters (T_{1e} and τ_m) seen in Eq. 1.4.[16-17] Therefore, the relaxivity of small molecule GBCAs is typically limited by the fast τ_R, and as a result, slowing τ_R is a very effective way to produce significant increases in relaxivity.[16] τ_R modulation is usually most effective at low field; however, as the magnetic field strength increases τ_R no becomes less of a limiting factor, and therefore τ_R-modulation strategies are usually ineffective at high field (7-9.4 T).[16]

In short, the τ_R-modulation strategy involves slowing the rotation of the Gd(III) complex. This is usually accomplished by making the contrast agent larger or designing the contrast agent to bind to something large to slow the rotation. Nanoparticles are commonly employed as a means of increasing τ_R.[36] GBCAs conjugated to nanoparticles often demonstrate drastic increases in τ_R and relaxivity, especially at low field. Gold nanoparticles, nanodiamonds, and silica nanoparticles have all been used as vehicles for GBCAs.[37-44] Furthermore, nanoparticles enable loading of many Gd(III) complexes per particle, which increases contrast through concentration.

Another common τ_R-modulation strategy includes binding to large biomacromolecules such as proteins and DNA. When the small molecule GBCA binds to a large biomacromolecule, it slows the rotation of the complex and an increase in τ_R results.[16-17] This strategy is used in some clinically approved GBCAs, such as Ablavar. Ablavar binds to albumin, a ubiquitous serum protein, which significantly increases the relaxivity of the agent as well as the half-life. In fact, when bound to albumin, Ablavar has a relaxivity 10 times higher than Gd-DTPA at 0.5 T,

highlighting just how significant an increase in τ_R can be for small molecule GBCAs.[17] Agents of these type are termed blood pool agents because they stay in the blood complexed with serum proteins and circulate for extended periods of time, making them very useful for imaging blood vessels (angiography).

Blood pool agents already have clinical utility; however, there are many reports of τ_R-modulated GBCAs used for other purposes. For example, GBCAs can be used to target receptor proteins, bind DNA, and self-aggregate in response to some biological stimulus, usually enzymatic cleavage (Scheme 1.3.)[45-50] If the GBCA interacts with its biological stimulus with high specificity, the observed contrast enhancement due to a τ_R-modulated relaxivity increase provides a readout in real time of that event.
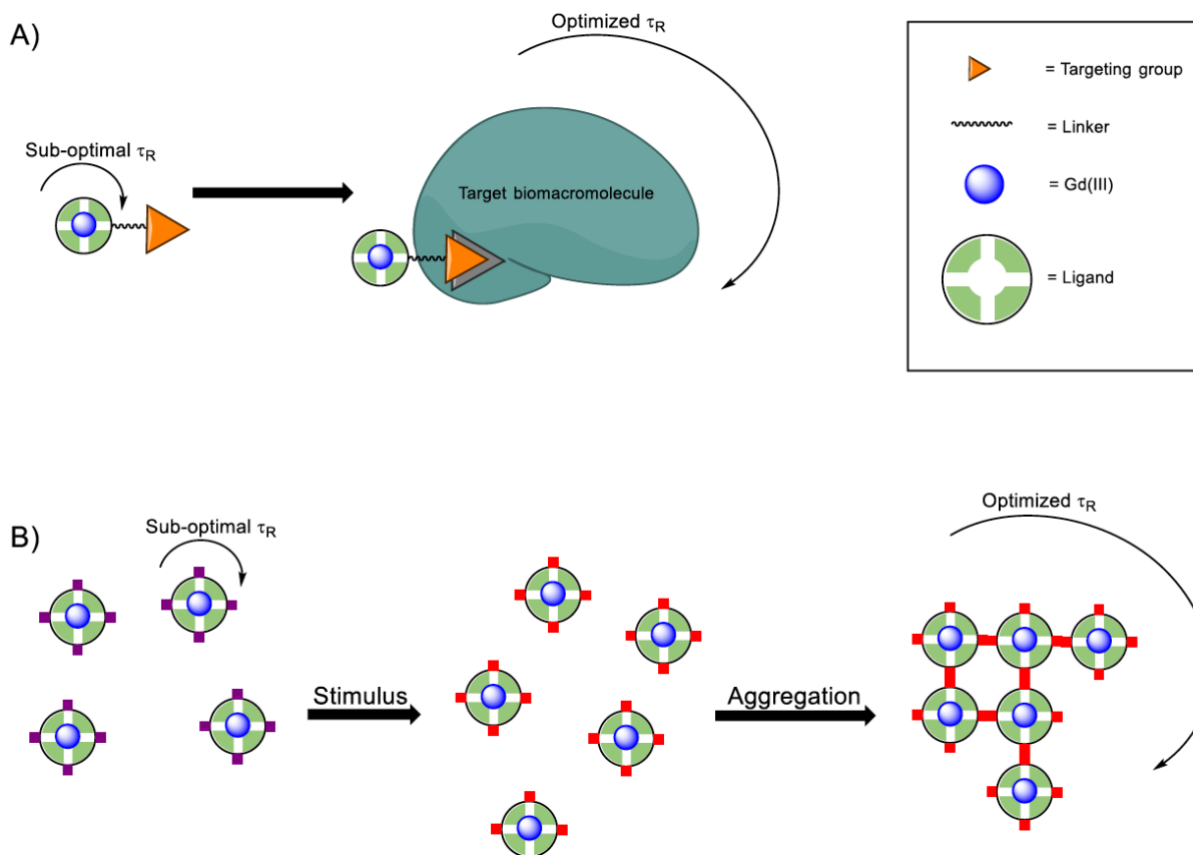
Scheme 1.3. Common strategies for τ_R-modulated GBCAs. (A) A small molecule GBCA can be designed to bind to a larger biomacromolecule. Upon binding, the τ_R increases, resulting in a increase in relaxivity at low magnetic field strength. If the GBCA targets that macromolecule with high specificity, the relaxivity increase provides contrast enhancement as a readout of the binding event. (B) Small molecule GBCAs can be designed to respond to a biological stimulus such that they self-aggregate, forming larger structures that have increased τ_R. Here, the increase in observed contrast gives a readout of the event that triggered aggregation. Figure graciously borrowed from: Krueger, Ruby. **2018**. *Towards detection of intracellular calcium flux by magnetic resonance imaging*. PhD Thesis, Northwestern University.

Because most biological targets are much larger than small molecule GBCAs, agents usually experience an increase in τ_R when they bind to their targets. In addition to the increase in τ_R, this strategy can also increase accumulation of the agents, which in turn can increase the observed contrast by increasing the local concentration of the agent. As previously discussed, large particles (Gd(III)-protein conjugates, nanoparticles, etc.) typically have longer half-lives and

circulate in the body longer, further increasing the accumulation and retention of the GBCA compared to a small molecule complex alone. Therefore, τ_R-modulation often goes hand in hand with increased accumulation of the agent, though that is not necessarily the case.

Electronic spin-lattice relaxation time (T_{1e}) of Gd(III):

The slow (~10^{-9} s) T_{1e} of Gd(III) that is inherently in tune with the Larmor frequency of protons is a fundamental property that makes Gd(III) such a great contrast agent for ^{1}H MRI.[16-17] T_{1e}, like Larmor frequency, is dependent on magnetic field strength. Unlike other parameters discussed like q and τ_R, T_{1e} affects all coordination spheres (both inner and outer) that contribute to relaxivity. As such, T_{1e} modulation offers a way of producing a truly "off" state for an activatable GBCA. If the T_{1e} can be changed such that it is no longer in tune with the Larmor frequency of protons, Gd(III) would cease to be an effective contrast agent (r_1 near 0). However, this is difficult because T_{1e} is not affected by simple chemical modifications or coordination differences in Gd(III) because it is a property stemming from the non-bonding 4f electrons. Instead, the proposed T_{1e} modulation strategy involves coupling Gd(III) to another paramagnetic metal ion with a fast T_{1e} (Fe, Cu, Co, Ru) through one or more shared bridging ligands that enables magnetic coupling (e.g. via superexchange). If magnetic coupling occurs between the Gd(III) and transition metal ion, the T_{1e} of Gd(III) can be sped up to the point where it no longer effectively relaxes protons. If the coupling can be broken through some process (e.g. redox of the transition metal to a diamagnetic complex) the T_{1e} of Gd(III) is restored and the agent returns to a normal relaxivity. Through this process, extremely large turn-on responses are possible due to the very low relaxivity off state. Preliminary proof of concept work has been accomplished in this area, yet probe design is

exceptionally difficult due to the requirements for coordinating Gd(III), accommodating a transition metal ion, incorporating a suitable bridging ligand, etc.[51] T_{1e} modulation is a fascinating strategy with enormous potential for activatable agents, but will likely be difficult to use in practical biological applications.

1.8 Theranostics and GBCAs

Theranostics are dual purpose agents that combine a therapeutic with a diagnostic, thus the name theranostic (sometimes seen as theragnostic).[52] Theranostics are powerful tools that deliver a therapy while simultaneously providing information on the course of therapy that otherwise would not be possible. For instance, theranostics can enable non-invasive visualization of where the therapy has been delivered (i.e. validation that the therapy has gone to its intended target), monitoring of treatment, monitoring of off-target toxicity, reporting of drug activation in prodrug strategies, etc. Any molecular imaging modality can be used in a theranostic, and indeed theranostic agents incorporating fluorophores, PET/SPECT radiotracers, and MRI contrast agents have all been reported.[52-54] Nanoparticles are commonly used in theranostics because contrast agents, therapeutics, targeting groups, etc. can all be easily conjugated.[55] The wide scope of nanoparticle materials and possible diagnostic and therapeutic groups makes for a near limitless combination of nanotheranostics. Many platforms include more than one diagnostic for multimodal imaging and more than one therapeutic for combination therapy. There are many examples of Gd(III) used in nanoparticle-based theranostics for MRI in the literature.[52] Although nanoparticles are the most common type of theranostic, small molecule agents are still quite prevalent, some of which incorporate GBCAs for MRI.[52] One common strategy is the use of a

prodrug, which is an inactive form of a therapeutic that becomes activated in response to some stimulus.[50,56] Theranostic GBCAs will be discussed in further detail in chapters 2 and 3.

1.9 Considerations for GBCAs

There are several key factors to consider when designing a GBCA to be used for molecular imaging. One of the most important factors (and often a limiting factor) is the abundance of the biological target of interest. Since relatively high concentrations of Gd(III) are necessary to appreciably enhance the observed contrast (10^{-5}-10^{-3} M), targets that have micromolar or nanomolar concentrations in the body are not suitable targets. Unfortunately, many biological targets of interest (receptors, extracellular/intracellular proteins, etc.) are at concentrations too low to be feasibly imaged by MR. Again, nanoparticles can be useful in this regard, as one nanoparticle can deliver hundreds of Gd(III) complexes per particle, shifting the window of what is feasible by one or two orders of magnitude.

Another key consideration is the location of the target of interest. Extracellular targets are generally quite accessible, as are many cell-surface targets; however, many biological targets are intracellular. GBCAs using a clinically approved ligand (DTPA or DO3A/DOTA derivative) are quite water soluble and do not readily penetrate cells. Therefore, delivering a GBCA intracellularly, especially in high enough amount to significantly enhance the contrast, is a difficult task. A variety of groups can be incorporated onto GBCAs to aid in cellular delivery, including cell penetrating peptides (CPPs), groups that target transporter proteins, and nanoparticles that can be endocytosed. Still, efficient intracellular delivery of GBCAs is a hurdle that must be carefully considered when designing a molecular imaging probe.

In addition to location of the target, the timeframe of the biochemical event of interest must be considered. Image acquisition takes minutes, therefore very fast biological processes are not likely feasible to image using MRI. However, special pulse sequences can be developed to help speed up image acquisition. On the other end of the spectrum, processes that occur very slowly can be difficult to image because over time the contrast agent will clear out of the body. In those instances, it is difficult to quantify signal that is coming from imaging the biological process vs. the signal that is lost due to agent clearance. As previously mentioned, quantification of activatable GBCAs is especially difficult because the "off" state is never truly $r_1=0$.

In summary, GBCAs are powerful and versatile tools in the molecular imaging toolkit. MRI is a unique imaging modality that offers safe and non-invasive imaging in any biological system (cells all the way to humans) with extraordinary soft-tissue contrast and anatomical information. Gd(III) complexes have a variety of parameters that can be manipulated to develop activatable agents that report on biochemical processes, and although there are limitations with sensitivity, time scale, and targeting, there are numerous ways in which GBCAs have and will be used for molecular imaging purposes.

1.10 Scope of Thesis

This thesis discusses the development of new theranostic and bioresponsive MR contrast agents, each of which utilize a Gd(III) complex. Chapter 2 discusses Gd(III)-Pt(II) theranostic agents that are used to image Pt(II) chemoresistance in tumors. Pt(II) chemotherapeutics (e.g. cisplatin) are some of the oldest and most widely used cancer drugs available, yet they have significant issues with off-target toxicity and chemoresistance. Though many chemoresistance

mechanisms are possible, and indeed usually multiple are at play, decreased drug accumulation is observed in nearly every case. Therefore, the goal of this project is to couple a Gd(III) complex to a Pt(II) drug to enable non-invasive visualization of the complex in tumors. If a tumor is Pt(II) sensitive, the theranostic agent should accumulate in normal amounts and contrast enhancement will be observed. If a tumor is Pt(II) resistant, the thernostic agent will accumulate to a lesser amount; therefore, this can be used as a proxy to tell if a tumor is likely chemoresistant by using MRI. This method could potentially be used to image for innate chemoresistance before starting therapy or to monitor for the onset of chemoresitance throughout therapy. In either case, detecting chemoresistance earlier helps patients get the most effective treatments possible and avoid undue toxicity.

Chapter 3 discusses the development of Gd(III)-Pt(IV) prodrugs, which can be used for tandem MRI and chemotherapy. Pt(IV) prodrugs are commonly used in preclinical research (and some are in clinical trials) because Pt(IV) is non-toxic, but can be reduced by biologically relevant reducing agents (e.g. glutathione, ascorbic acid) to Pt(II), the active cytotoxic agent. While Pt(II) complexes are square planar, Pt(IV) complexes are octahedral, and therefore the axial ligands can be used to couple other chemical entities that ultimately dissociate when the platinum is reduced. In this project, a Gd(III) complex was coupled axially to a Pt(IV) prodrug. The agent was able to enter cells, where the Pt(IV) was reduced to Pt(II), releasing active cisplatin. Compared to the Gd(III)-Pt(II) agents discussed in chapter 2, the Gd(III)-Pt(IV) are much better therapeutics when they release cisplatin. Additionally, Gd(III) was observed to be well retained in cells, making this platform promising for intracellular contrast enhancement and imaging of therapy. Finally, there was is an additional axial ligand available that can be used to incorporate targeting groups,

fluorophores for multimodal imaging, or other therapeutics for combination therapy. These possibilities will be explored in future generations of Gd(III)-Pt(IV) agents.

Chapter 4 discusses the development of a Ca(II) sensing GBCA that increases its relaxivity through a q-modulation strategy in the presence of Ca(II). Several Ca(II) sensing GBCAs have been developed over the past two decades; however, the vast majority sense extracellular Ca(II) where concentrations are high. The goal of this project was to develop an agent that has high cellular uptake in order to image intracellular Ca(II) flux. Since Ca(II) is the primary transducer of electrical activity in neurons, the goal is to use this agent to image neuronal activity in the brain. A Ca(II) sensing agent with high cell uptake was developed by incorporating an analogue of the NIR fluorescent dye, IR-783. IR-783 targets organic anion transporter polypeptides (OATPs), resulting in active transport into cells. An IR-783 moiety was coupled to a Ca(II) sensing GBCA, and was found to enter cells in large amount. As an added benefit, IR-783 enables fluorescence imaging at NIR wavelengths for multimodal imaging and optical validation of the location of the probe. *In vivo* experiments using this agent are underway.

CHAPTER 2

Development of Gd(III)-Pt(II) Theranostic MR Contrast Agents

for Imaging Pt(II) Chemoresistance

2.1 Introduction

Since its initial FDA approval in 1978, cisplatin has proved to be an essential tool for the treatment of various types of solid tumors.[1-3] The success of cisplatin sparked widespread research into the development of other Pt(II), and more recently, Pt(IV) complexes that are efficacious chemotherapeutics.[4-7] Despite decades of research and clinical trials, there are only three Pt-based drugs approved by the FDA: cisplatin, carboplatin, and oxaliplatin.

Remarkably, these drugs are used in nearly 50% of all chemotherapy regimens.[8] Although they have widespread clinical use, Pt(II) chemotherapeutics are impeded by issues with off-target toxicity and chemoresistance.[9-13] Tumors can have both innate and acquired chemoresistance stemming from various mechanisms. These include decreased influx, increased efflux, increased sequestration in the cytoplasm by thiols, and increased DNA repair/resistance to damage. There is currently no effective method to predict tumor response to Pt(II) chemotherapy because the mechanisms of resistance and associated genes are not completely known or understood.[14-16] Once patients begin a Pt(II) regimen, they undergo weeks or months of treatment (two cycles, six to eight weeks *minimum* for cisplatin) before the tumor can be reevaluated for a clinical response, typically by measuring tumor size by MRI or CT.[17-21] If the tumor has not responded, the patient has been exposed to unnecessary toxicity and lost precious time. In order to improve efficacy and mitigate patient exposure to harmful side effects, new research tools are necessary to *predict* tumor response to Pt(II) chemotherapies.

Though multiple chemoresistance mechanisms are possible, and indeed a combination of mechanisms is typical, decreased accumulation of Pt(II) is one of the most consistently identified

causes of Pt(II) resistance.[22-24] This presents an ideal opportunity to use Gd(III)-Pt(II) theranostic MRI contrast agents (CAs) to image Pt(II) chemoresistance. Pt(II) moieties that have similar structures to chemotherapeutics, such as cisplatin or carboplatin, can be incorporated into Gd(III) CAs, allowing the agents to behave as Pt(II) drugs. This provides a powerful platform for determining if cancer cells of interest take up Pt(II) complexes. If a tumor is resistant to Pt(II) through a mechanism that results in decreased drug accumulation, the observed MR contrast enhancement due to the theranostic agent will be lower than in Pt(II) sensitive tumors that take the drugs up in higher amounts. In this way, the extent of MR contrast enhancement provides a direct and non-invasive readout of Pt(II) accumulation (Scheme 1). This, in turn, may provide a means of imaging Pt(II) chemoresistance.

There are few examples of Gd(III)-Pt(II/IV) agents in the literature, none of which have been used to image factors related to chemoresistance.[25-31] Here, we describe two Gd(III)-Pt(II) agents that were synthesized by coupling a Gd(III) MR CA to cisplatin and carboplatin-based complexes. These agents are designed to mimic the mechanism of action of Pt(II) drugs (i.e. bind to DNA). As a consequence, they provide *intracellular* contrast enhancement, whereas Gd(III) CAs are typically limited to the extracellular environment.[32, 33] This platform offers a straightforward way to non-invasively probe the amount of Gd(III) (and Pt(II) by proxy) in cancer cells. This method to image Pt(II) accumulation, a dominant factor of chemoresistance, is a crucial first step towards predicting response to therapy and monitoring for the onset of chemoresistance—a critical unmet need in medicine.
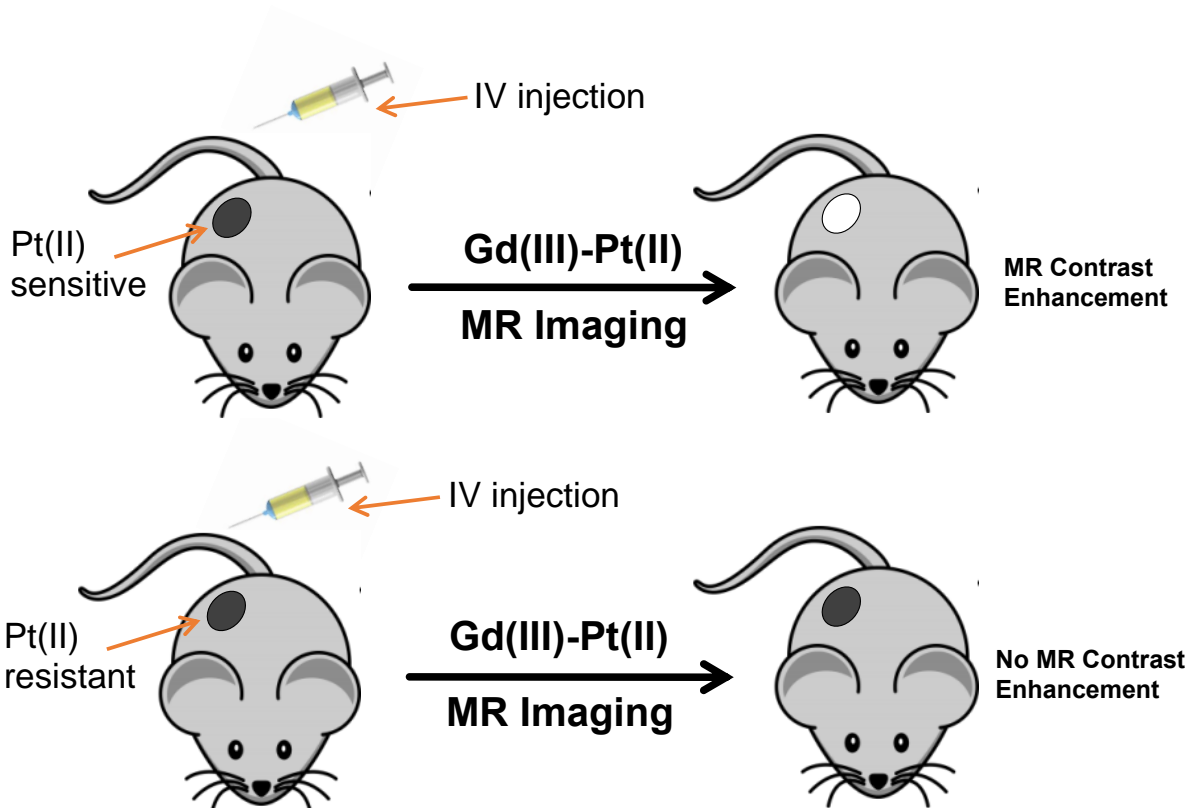
Scheme 2.1. Demonstration of how Gd(III)-Pt(II) agents may be used to image Pt(II) accumulation differences. Gd(III)-Pt(II) agents will accumulate in Pt(II) sensitive tumors, providing MR contrast enhancement. In Pt(II) resistant tumors, there is a decreased drug accumulation due to chemoresistance. Therefore, Gd(III)-Pt(II) agents will accumulate to a lesser extent, resulting in little to no MR contrast enhancement. This may provide a means of imaging Pt(II) chemoresistance.

2.2 Results and Discussion

Synthesis and purification of the agents. Two Gd(III)-Pt(II) agents, **GP1** and **GP2**, were synthesized through a copper-catalyzed click (CuAAC) reaction between Gd(III) complex **1** and Pt(II) complexes **2** and **3** (Figure 2.1.) Complexes **1**-**3** were synthesized using adapted literature protocols.[34, 35] **GP1** and **GP2** were synthesized from **1-3** in one step after finding adequate conditions for the CuAAC reaction. Both agents were purified by preparatory HPLC, characterized by HPLC-MS and HRMS (see appendix), and analyzed by ICP-MS to ensure the Gd:Pt ratio was near 1:1. The higher yield of **GP2** is attributed to the greater stability of the carboplatin moiety compared to cisplatin.

A)

1

GP1

GP2

B)

cisplatin

carboplatin

2

3
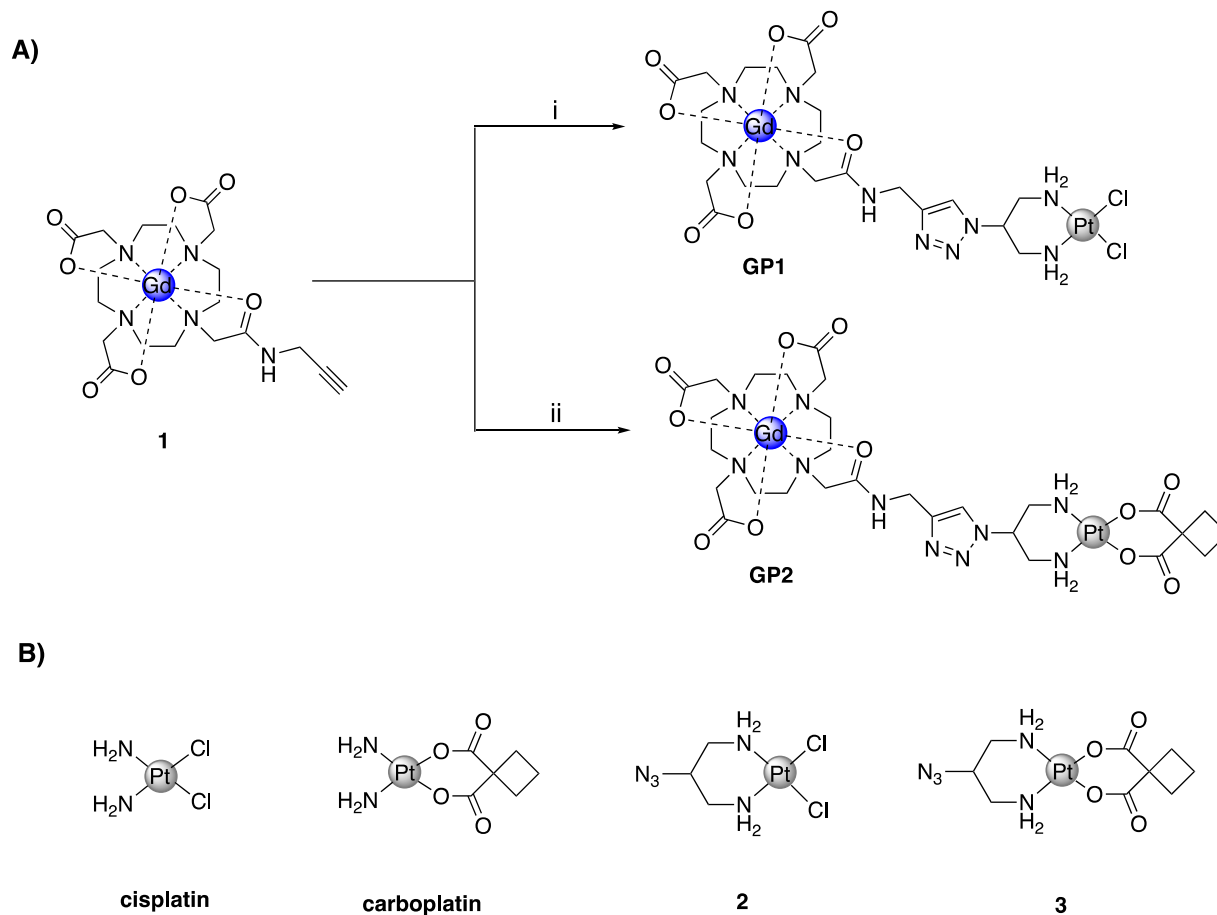
Figure 2.1. (A) Synthetic scheme of **GP1** and **GP2**: (i) **2** (1.1 equiv.), (+)-sodium L-ascorbate (0.5 equiv.), $CuSO_4(H_2O)_5$ (0.25 equiv.), DMF, RT, N_2, 32%; (ii) **3** (1.1 equiv.), (+)-sodium L-ascorbate (0.5 equiv.), $CuSO_4(H_2O)_5$ (0.25 equiv.), DMF, RT, N_2, 68%; (B) Structures of cisplatin, carboplatin, and the corresponding azide-appended complexes **2** and **3**.

Relaxivity measurements and DNA binding. The T_1 relaxivity (r_1) and T_2 relaxivity (r_2) of **GP1** and **GP2** at low (1.41 T) and high (7 T) field strength were measured in pH 7.40 tris buffer in the absence, and presence of calf thymus DNA (CT-DNA). These new agents were designed to behave like Pt(II) drugs, and as such, should have the ability to bind DNA, which can affect relaxivity.

The measured r_1 values are summarized in Table 2.1 (see appendix for r_2 values). At 1.41

T, **GP1** had an r_1 of 5.8 mM^{-1}s^{-1} in the absence and 13.3 mM^{-1}s^{-1} in the presence of CT-DNA, a

129% increase. At high field, the r_1 was 5.1 mM^{-1}s^{-1} without and 4.8 mM^{-1}s^{-1} with CT-DNA. The

large relaxivity increase at low field can be attributed to an increase in the rotational correlation

time (τ_R) upon binding to DNA. At high field, an increase in r_1 due to τ_R is not observed, as

expected.[36] Similar results were observed for **GP2**. At low field, **GP2** had an r_1 of 4.9 mM^{-1}s^{-1} in

the absence and 10.1 mM^{-1}s^{-1} in the presence of CT-DNA, a 106% increase. At high field, the r_1

was 5.0 mM^{-1}s^{-1} without and 5.4 mM^{-1}s^{-1} with CT-DNA.

These results demonstrate **GP1** and **GP2** behave as excellent MR CAs that can bind DNA.

In the absence of DNA, both agents have relaxivities well within the range for small molecule

Gd(III) complexes.[32, 33] In the presence of DNA, there is a significant boost in relaxivity at low

field attributed to a τ_R increase upon binding DNA. The absence of this relaxivity boost at high

field further supports the significant role τ_R plays in affecting the observed relaxation properties of

the agent. The significant contrast enhancement upon binding DNA at low field is useful because

it will likely enhance MR contrast intracellularly when compared to Pt(II) resistant cells, which

consistently exhibit lower numbers of Pt(II)-DNA adducts.[37]

Table 2.1. r_1 values of **GP1** and **GP2** at low (1.41 T) and high (7 T) field strength in pH 7.40 tris buffer at 37 °C

Agent:	Low Field (1.41 T)		High Field (7 T)	
	w/o CT-DNA	w/ CT-DNA	w/o CT-DNA	w/ CT-DNA
GP1	5.8	13.3	5.1	4.8
GP2	4.9	10.1	5.0	5.4

To further characterize the DNA binding, circular dichroism (CD) was used. CT-DNA was incubated with varying equivalents of **GP1**, **GP2,** cisplatin, or carboplatin to assess how each is shifted in the CD spectrum of CT-DNA. This provides a direct means of determining if the agents bind to DNA in the same way as their Pt(II) analogues. Previous research has shown Pt(II) drugs red-shift the CD spectrum of CT-DNA and cause an initial increase in ellipticity, with a subsequent decrease in ellipticity as the number of Pt(II)-DNA adducts increases (see ESI for CD spectra with cisplatin and carboplatin).[38, 39]

It is important to note that carboplatin is far less reactive than cisplatin, therefore it takes *significantly* more of the complex to produce the same number of Pt(II)-DNA adducts. Fig. 2 shows the CD spectra of CT-DNA incubated with varying equivalents of **GP1** (Figure 2.2A) and **GP2** (Figure 2.2B). Both agents shift the CD spectrum of CT-DNA in the same way as cisplatin and carboplatin, indicating they are binding to DNA in a similar manner. These data further suggest **GP1** and **GP2** can mimic the mechanism of action of Pt(II) drugs, which is essential if they are to be used to image Pt(II) resistance.
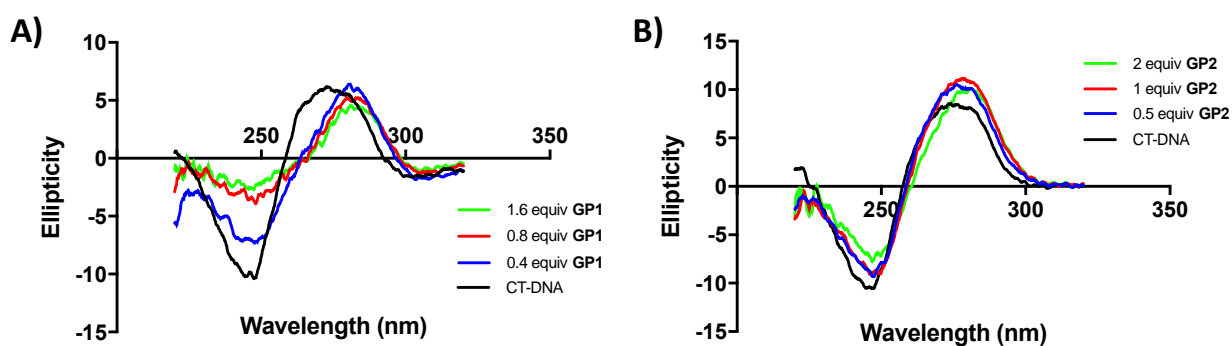
Fig. 2.2. CD spectra of 100 μM CT-DNA in pH 7.40 tris buffer incubated with varying equivalents of (A) **GP1** at 37 °C for 24 h and (B) **GP2** at 37 °C for 24 h. Both agents shifted the spectrum of CT-DNA in a similar manner as their Pt(II) analogues, cisplatin and carboplatin (see appendix).

Cytotoxicity of the agents. The cytotoxicity of **GP1** and **GP2** was measured in Pt(II) sensitive HeLa and A2780 cells, as well as cisplatin resistant 2780CP/Cl-16 cells (derivative of A2780). 2780CP/Cl-16 cells are not commercially available and were obtained from Professor Zahid Siddik at MD Anderson Cancer Center. These cells were developed by exposure to cisplatin and have been extensively characterized.[40] 2780CP/Cl-16 have a mutated *p53* tumor suppressor gene, increased glutathione concentrations, and decreased accumulation of cisplatin, all of which are mechanisms of resistance. This combination of chemoresistance mechanisms makes them a realistic model for Pt(II) resistance.

Table 2.2 summarizes the IC_{50} of cisplatin, carboplatin, **GP1**, and **GP2** in each of the cell lines (see ESI for IC_{50} curves). The IC_{50} measured for cisplatin and carboplatin were well within the range reported in the literature.[41, 42] Not surprisingly, each had a higher IC_{50} in 2780CP/Cl-16 cells, indicating Pt(II) resistance. Compared to their Pt(II) analogues, **GP1** and **GP2** consistently had higher IC_{50} values in all cell lines. This decrease in toxicity is expected because **GP1** and **GP2** contain a bulky Gd(III) complex, which likely decreases cell permeability, and therefore requires higher incubation concentrations to achieve the same levels of intracellular Pt(II). Most importantly, 2780CP/Cl-16 cells demonstrated resistance to both **GP1** and **GP2** compared to A2780 cells. This is essential in order to use these cell lines as a model to image Pt(II) resistance. Even though they are not as potent chemotherapeutics as cisplatin and carboplatin, these data support that **GP1** and **GP2** behave as Pt(II) drugs.

Table 2.2. IC_{50} concentrations of cisplatin, carboplatin, **GP1**, and **GP2** in various cell lines

Complex	IC_{50} (μM)		
	A2780	**2780CP/Cl-16**	**HeLa**
Cisplatin:	7.3	14.7	12.2
Carboplatin:	15.6	86.6	60.5
GP1:	117	498	222
GP2:	519	1774	1120

Accumulation of the agents in cells. To measure intracellular accumulation of **GP1** and **GP2**, concentration-dependent cell uptake experiments were performed in HeLa, A2780, and 2780CP/Cl-16 cells. Table 2.3 summarizes the cellular accumulation of Gd(III) in each of these cell lines when dosed at the respective IC_{50}. 2780CP/Cl-16 cells were dosed at the IC_{50} of A2780 cells in order to directly compare accumulation in the two cell lines.

Gd(III) uptake in all cell lines from both agents is higher than what is typically considered the detection limit for MR (high μM to low mM concentrations).[43, 44] This suggests that **GP1** and **GP2** penetrate cells in high enough amount to enhance intracellular MR contrast. Additionally, the Gd:Pt ratio in each case was close to 1.0. Our previous work with Gd(III)-Pt(IV) agents showed drastically different levels of cellular Gd/Pt accumulation because the Gd(III) and Pt(II/IV) complexes were designed to dissociate intracellularly.[28] Here, the Gd(III) and Pt(II) complexes remain coupled, and therefore it is expected the Gd:Pt ratio is much closer to 1, as is observed.

Table 2.3. Accumulation of **GP1** and **GP2** in A2780, 2780CP/Cl-16, and HeLa cells when incubated near the IC_{50}* for 24 h.

Complex:	A2780 Cells		2780CP/Cl-16 Cells		HeLa Cells	
	Gd (fmol/cell)	Gd:Pt Ratio	Gd (fmol/cell)	Gd:Pt Ratio	Gd (fmol/cell)	Gd:Pt Ratio
GP1	1.7 ± 0.2	1.11	1.1 ± 0.1	1.07	1.3 ± 0.3	1.09
GP2	1.7 ± 0.3	1.12	1.4 ± 0.1	1.10	2.1 ± 0.3	1.06

*2780CP/Cl-16 cells were dosed at the same concentrations as A2780 cells to allow for direct comparison.

Figure 2.3A shows that at each concentration there is a statistically significant (p<0.01) increase in accumulation of **GP1** in A2780 vs. 2780CP/Cl-16 cells. At a 125 μM incubation concentration, there was a 43% difference in Gd(III) accumulation. These data demonstrate that like cisplatin, **GP1** accumulates less in 2780CP/Cl-16 cells because they are Pt(II) resistant. This method provides a straightforward way of imaging a main cause of Pt(II) resistance by MRI, since the amount of CA present is directly proportional to the contrast enhancement.

Unlike **GP1**, there was no clear difference in accumulation of **GP2** in the two different cell lines (Figure 2.3B). At lower concentrations, the uptake of **GP2** in 2780CP/Cl-16 cells was actually higher than in A2780 cells. At 500 μM (~IC_{50} in A2780), the accumulation was higher in A2780 cells; however, the difference is not statistically significant. Clearly, the behavior of **GP2** varies from that of **GP1** and this difference is attributed to the Pt(II) moieties of the two agents. Carboplatin and cisplatin have significantly different properties (e.g. reactivity and hydrophobicity) that can affect how the agents behave. Additionally, 2780CP/Cl-16 cells were

made resistant through cisplatin exposure, not carboplatin. Though 2780CP/Cl-16 cells showed resistance to **GP2** in cytotoxicity assays, decreased accumulation is clearly not as much of a factor.

In addition to concentration-dependent uptake, time-dependent uptake experiments were performed in HeLa cells to assess how quickly the agents accumulate intracellularly (see appendix). These experiments showed that MR relevant amounts of agent accumulate in cells within the first 3 hours, with increased accumulation observed over longer amounts of time. Rapid accumulation is necessary for the agents to effectively enhance MR contrast of tumors *in vivo*.
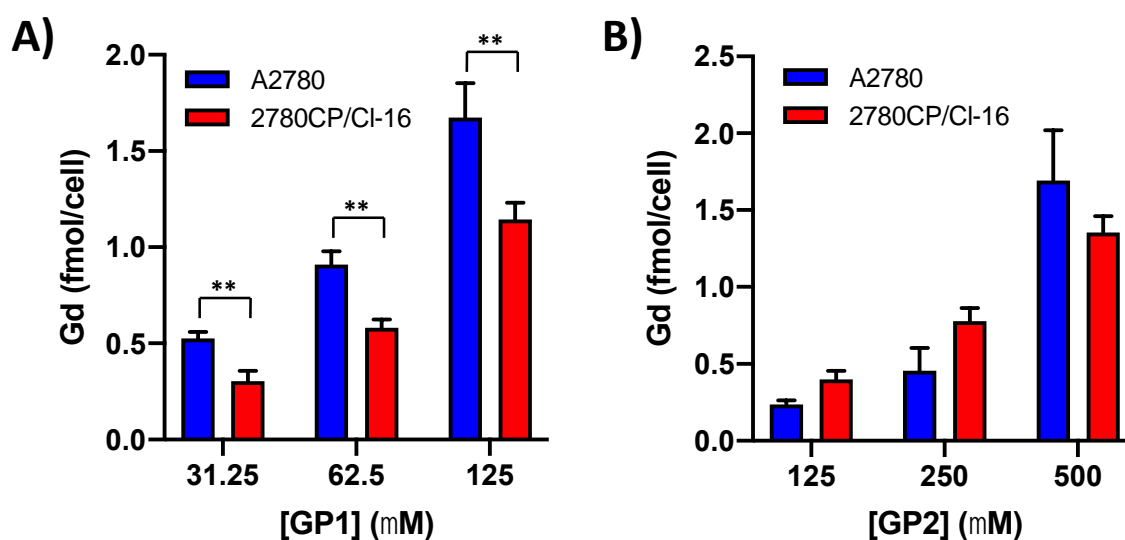
Figure 2.3. (A) Accumulation of **GP1** in A2780 and 2780CP/Cl-16 cells at varying concentrations up to the IC$_{50}$ of **GP1** in A2780 cells (~125 μM). At each concentration, there was a statistically significant ($p<0.01$) decrease in **GP1** accumulation in cisplatin resistant 2780CP/Cl-16 cells compared to the parent A2780 cells. (B) Accumulation of **GP2** in A2780 and 2780CP/Cl-16 cells at varying concentrations up to the IC$_{50}$ of **GP2** in A2780 cells (~500 μM). There is no clear trend in accumulation of **GP2** in the two cell lines.

MR Imaging of A2780 and 2780CP/Cl-16 cell pellets. MR imaging of A2780 and 2780CP/Cl-16 cell pellets treated with **GP1** and **GP2** was performed to assess if the agents can significantly enhance the intracellular contrast. Cells were incubated with **GP1** and **GP2** for 24 hours, washed, then pelleted and imaged in a 7 T MR scanner. The relaxation rate (R_1), which is defined as $1/T_1$ and is directly proportional to MR contrast, was determined and compared to untreated control cell pellets.

Figure 2.4 shows the results of the cell pellet MR imaging experiments. As expected from the cell uptake experiments, both **GP1** and **GP2** enhanced the intracellular MR contrast of both cell lines. In A2780 cells, **GP1** increased the R_1 by 54%, which was the largest contrast enhancement observed (Figure 2.4A). In 2780CP/Cl-16 cells, the same dose of **GP1** resulted in an R_1 increase of just 22%. This 32% difference in ΔR_1 demonstrates that the differences in accumulation of **GP1** in the Pt(II) sensitive A2780 and Pt(II) resistant 2780CP/Cl-16 cells results in significant differences in MR contrast. This supports the idea that Gd(III)-Pt(II) agents may be used to image Pt(II) chemoresistance.

Treatment with **GP2** resulted in nearly identical contrast enhancement in Pt(II) sensitive and resistant cell lines (Figure 2.4B). This was expected based on the cell uptake experiments, which showed a non-significant difference in accumulation at that dose (500 μM). Because of this, **GP2** was not included in further experimentation.
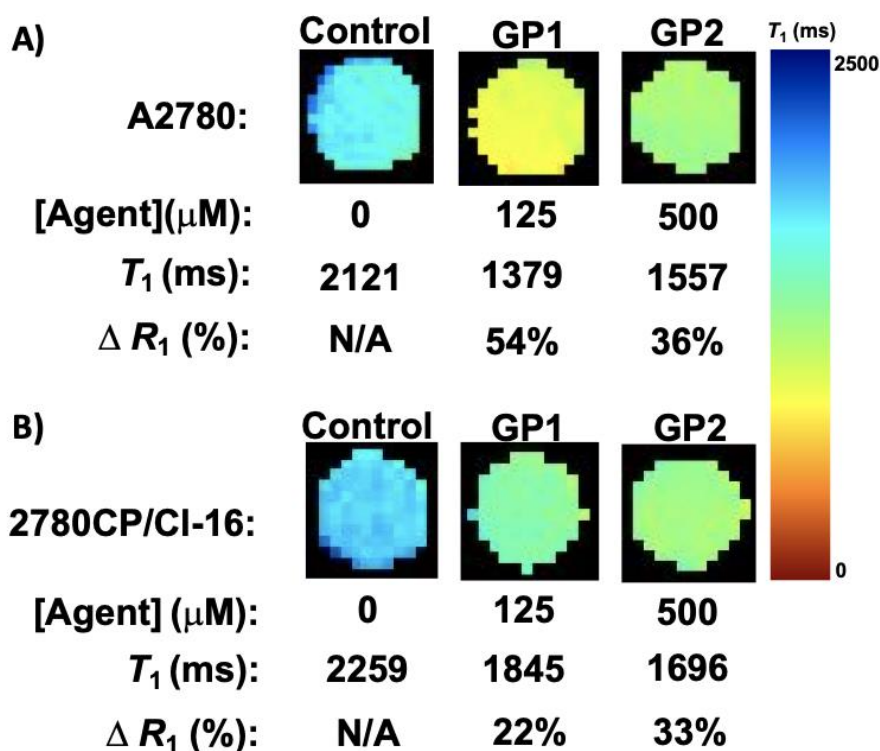
Figure 2.4. (A) MR images of A2780 cell pellets that were untreated (control), treated with 125 μM **GP1**, or 500 μM **GP2**. Both **GP1** and **GP2** significantly enhanced the intracellular contrast of A2780 cells. (B) MR images of 2780CP/Cl-16 cell pellets that were untreated (control), treated with 125 μM **GP1**, or 500 μM **GP2**. Both agents enhanced the MR contrast of 2780CP/Cl-16 cells. However, the contrast enhancement by **GP1** was significantly lower in 2780CP/Cl-16 cells compared to A2780 cells. The contrast enhancement by **GP2** was virtually the same in both cell lines. MR imaging was performed on a 7 T scanner and all cells treated with agent were dosed at IC$_{50}$ concentrations for 24 h prior to imaging.

***In vivo* MR imaging of GP1 in A2780 and 2780CP/Cl-16 flank tumors.** The promising *in vitro* results of **GP1** led to *in vivo* MR imaging experiments in murine models. Mice bearing either an A2780 or 2780CP/Cl-16 flank tumor received 0.15 mmol/kg of **GP1** through intravenous injection and were imaged 15 minutes and 3 hours post-injection. This dose was determined after considering typical clinical and preclinical doses of cisplatin and adjusting for the molar mass and

cytotoxicity of **GP1** compared to cisplatin.[45] The tumors were then harvested after the 3 hour time point and the accumulation of **GP1** was measured by ICP-MS of the whole tumor. Figure 2.5A shows representative images from the *in vivo* experiments. 15 minutes post-injection, **GP1** enhanced the contrast of both tumor types. Contrast enhancement was not uniform throughout the entire tumor, likely because the majority of agent was in the vasculature. After 3 hours, contrast enhancement remained in areas of the A2780 tumors; however, the 2780CP/Cl-16 tumors returned to baseline. ICP-MS analysis of the tumors at 3 hours post-injection (Figure 2.5B) confirmed that there was a statistically significant difference ($p < 0.05$) in accumulation of Gd(III) in the two tumor types. As expected, there was also a similar difference in accumulation of Pt(II) (see appendix).

These results demonstrate that the lower accumulation of **GP1** in 2780CP/Cl-16 due to Pt(II) resistance translates to *in vivo* models. Furthermore, the differences in agent accumulation can be qualitatively observed by MR imaging, providing a way of noninvasively imaging Pt(II) accumulation differences. This proof of concept is an important first step towards demonstrating the ability of Gd(III)-Pt(II) agents to image Pt(II) chemoresistance, and ultimately, predict the outcome of Pt(II) chemotherapy and monitor for the onset of chemoresistance.
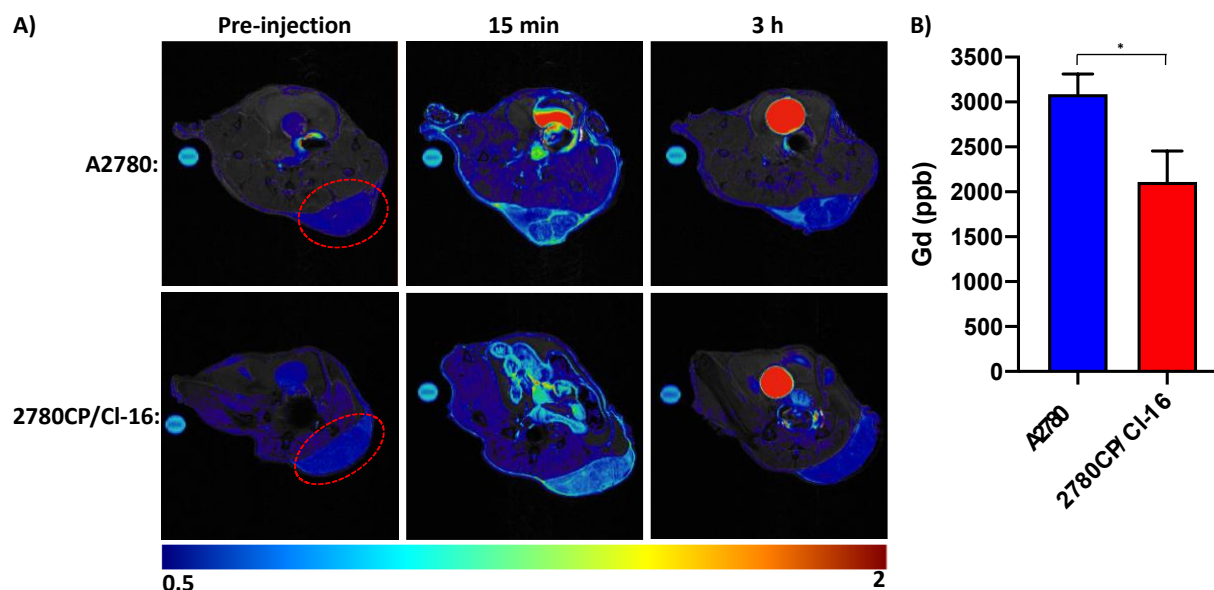
Figure 2.5. (A) MR images (9.4 T) of axial slices of mice bearing A2780 (top row) or 2780CP/Cl-16 (bottom row) flank tumors. Mice received 0.15 mmol/kg **GP1** intravenously and imaging was performed pre-injection and at 15 minutes and 3 hours post-injection. Tumor area is encircled in red and images are normalized to a reference standard of MultiHance (light blue circle left of mice). **GP1** enhanced contrast in both tumor types at 15 minutes post-injection. However, contrast enhancement persisted at 3 hours only in A2780 tumors. (B) Gd(III) content of each tumor type (n=3 for each) 3 hours post injection measured by ICP-MS. There was a statistically significant difference in accumulation ($p < 0.05$) of Gd(III) in the Pt(II) sensitive A2780 tumors compared to the Pt(II) resistant 2780CP/Cl-16 tumors.

2.3 Conclusions

We have developed a Gd(III)-Pt(II) theranostic agent (**GP1**) that behaves like cisplatin and provides T_1-weighted MR contrast enhancement. **GP1** accumulates to a lesser extent in cisplatin resistant 2780CP/Cl-16 cells compared to the parent cisplatin sensitive A2780 cells. This difference in accumulation results in differences in MR contrast enhancement both *in vitro* and *in vivo* and may provide a facile way of imaging Pt(II) resistance. This is a critical first step towards the goal of imaging Pt(II) resistance in order to predict the outcome of Pt(II) chemotherapy and

monitor for the onset of chemoresistance throughout therapy, a critical unmet need in medicine. Furthermore, this platform could potentially be applied to any chemotherapeutic where decreased drug accumulation is a dominant mechanism of chemoresistance. We are currently developing optimized Gd(III)-Pt(II) agents that have superior toxicity and cell uptake profiles. The goal is to test the optimized agents in more in-depth *in vivo* experiments that correlate quantitative MR imaging with cisplatin therapy outcomes to demonstrate the ability of Gd(III)-Pt(II) agents to image Pt(II) chemoresistance.

CHAPTER 3

Development of Gd(III)-Pt(IV) Theranostic Contrast Agents for

Tandem MR Imaging and Chemotherapy

3.1 Introduction

For decades, Pt(II) chemotherapeutics have been fundamental tools for the treatment of solid tumors.[1-3] Although there have been extensive efforts to develop new Pt-based chemotherapeutics, there are currently only three approved by the FDA: cisplatin, carboplatin, and oxaliplatin.[4-7] All FDA approved Pt chemotherapeutics are Pt(II) square planar complexes that cross-link DNA, ultimately leading to apoptosis in fast-dividing cells.[1, 8] This mechanism of action makes them highly effective at treating solid tumors. Even so, they have significant off-target toxicity that can result in a number of serious side effects including renal failure, hearing loss, and myelosuppression.[1-5] Pt(II) chemotherapeutics are also susceptible to chemoresistance. This stems from multiple mechanisms, including decreased drug accumulation, cytosolic sequestration, and resistance to DNA damage.[8-12] Despite issues with toxicity and chemoresistance, Pt(II) complexes are used in nearly 50% of all chemotherapy regimens, making them some of the most widely used cancer drugs available.[13]

A number of approaches have been attempted to mitigate off-target toxicity and chemoresistance of Pt drugs. This includes using tumor-targeting groups, nanoconstructs, and selective release mechanisms.[14-16] In recent years, Pt(IV) prodrugs have become a promising approach to alleviate off-target toxicity and reduce chemoresistance.[14-19] Pt(IV) complexes are octahedral and inert compared to their Pt(II) square planar analogues. In an oxidizing extracellular environment Pt(IV) complexes remain inert. They can be reduced intracellularly to Pt(II), that triggers the dissociation of a reactive Pt(II) drug from its axial ligands.[15-19] A variety of groups can be incorporated as axial ligands to allow for tumor targeting, combination therapy, bioimaging, and controlled reduction of the Pt(IV).[20-31] Sessler and coworkers were the first to demonstrate

how Gd(III) complexes can be used synergistically with Pt(IV) prodrugs. Their Gd(III)-texaphyrin complexes have been used to increase tumor localization and mediate the reduction of Pt(IV) to Pt(II).[30, 31] However, we believe there is a significant opportunity to investigate Gd(III)-Pt(IV) mixed metal complexes for applications as theranostic agents.

Several examples of theranostic Pt(IV) prodrug complexes for dual chemotherapy and fluorescence imaging have been reported.[24-27] Some of these probes can provide important information regarding drug delivery and subsequent reduction of the Pt(IV) complex *in vitro*. However, *in vivo* fluorescence imaging has limited clinical utility.[32, 33] The primary modality for imaging tumors is MRI, which allows for whole body, non-invasive imaging with excellent soft tissue contrast and spatial resolution.[32-36] While a few examples of Gd(III)-Pt(II) theranostics have appeared,[37-39] to our knowledge there are no reported examples of Pt(IV) prodrugs containing a Gd(III) complex for contrast-enhanced MR imaging either *in vitro* or *in vivo*.

Here, we describe two Gd(III)-Pt(IV) theranostic agents that were synthesized by coupling a Gd(III) MR contrast agent axially to cisplatin and carboplatin-based Pt(IV) complexes. These agents are water soluble, cell permeable, and oxidatively stable, but are reduced under biologically relevant intracellular conditions to release the toxic Pt(II) payload and the Gd(III) MR agent (Scheme 3.1.) These complexes are designed for *intracellular* contrast enhancement of cancer cells, whereas typical Gd(III) contrast agents are limited to the extracellular space surrounding tumors.[34, 40] This Gd(III)-Pt(IV) platform possesses a second axial site that can be used to couple targeting groups for tumor specificity, drugs to combat chemoresistance, or fluorophores for multimodal imaging and validation.
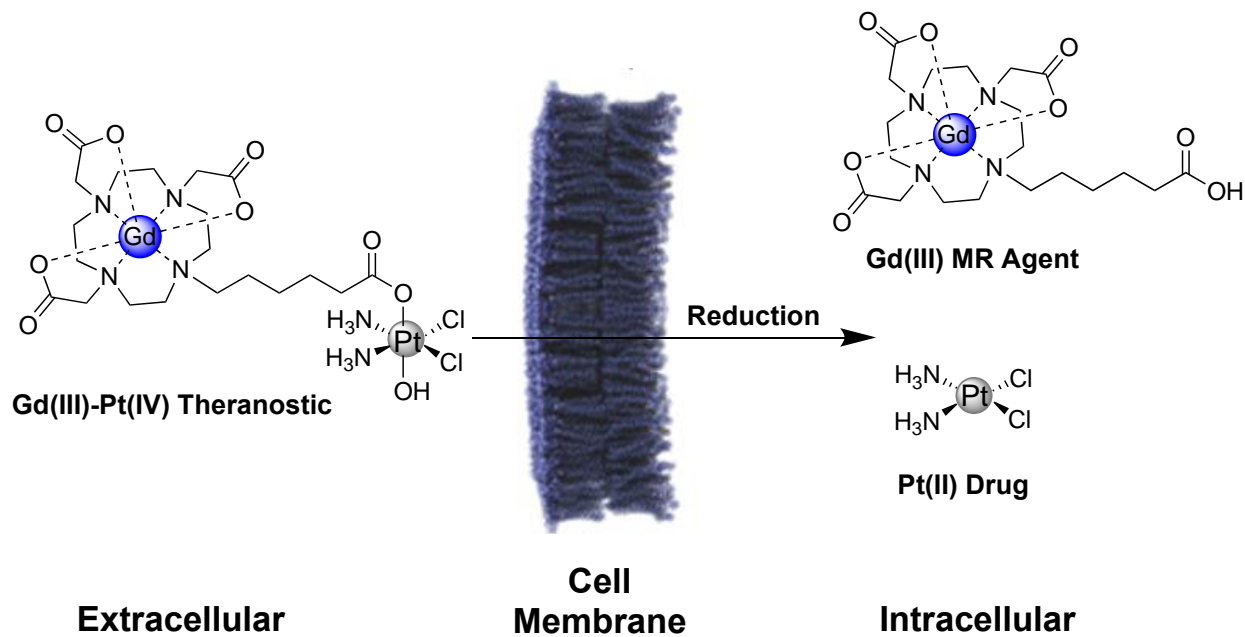
Scheme 3.1. Schematic of a Gd(III)-Pt(IV) theranostic agent. In the oxidizing extracellular environment, the agent remains in the Pt(IV) oxidation state.[15] Upon entering the cell, the agent is reduced to Pt(II), simultaneously releasing the therapeutic Pt(II) drug and a Gd(III) MR contrast agent.

3.2 Results and Discussion

Synthesis and purification of the agents. Two Gd(III)-Pt(IV) agents, **GP1** and **GP2** were synthesized by coupling a Gd(III) complex, **1**, with Pt(IV) complexes **2** and **3** respectively (Figure 3.1A.) Complexes **1**, **2**, and **3** were all synthesized following literature protocols.[41-43] The structures of **GP1** and **GP2** are found in Figure 1A. Both agents were purified by preparatory HPLC, characterized by HPLC-MS (see supplementary information) and analyzed by ICP-MS to ensure the Gd:Pt ratio was 1:1.
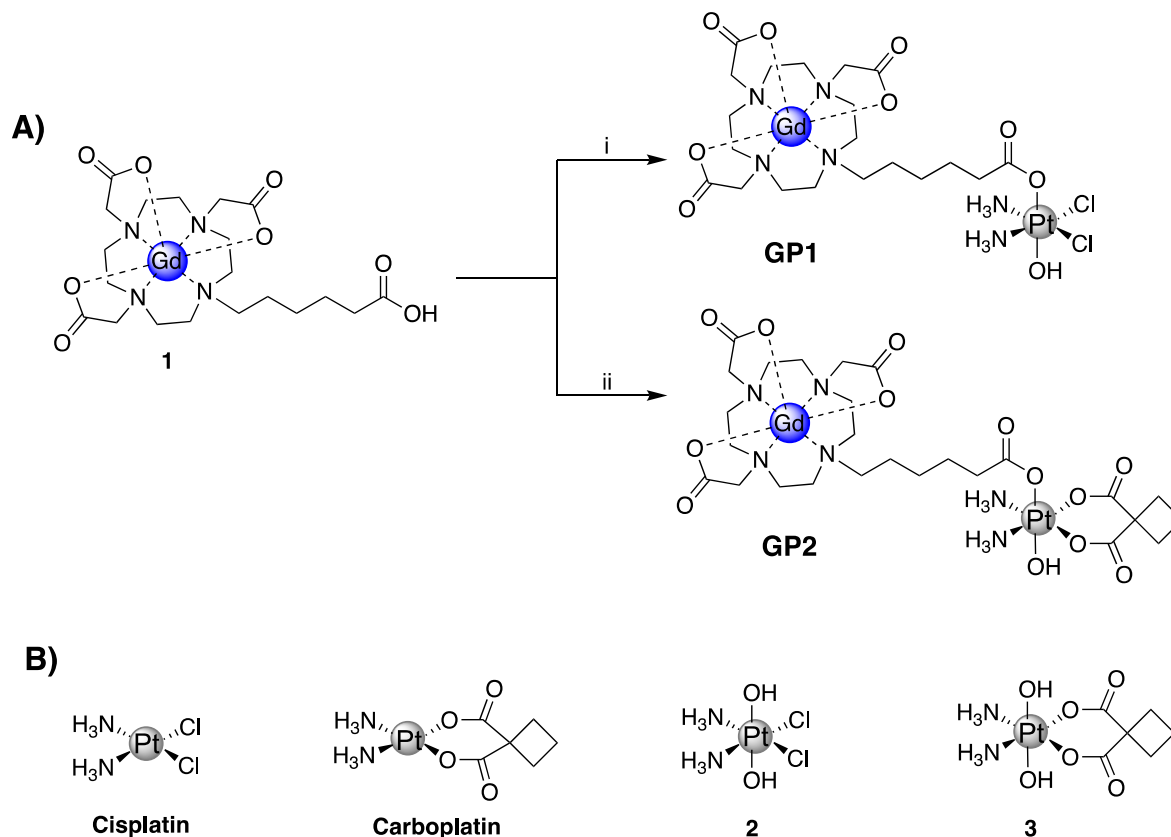
Figure 3.1. (A) Synthetic scheme of **GP1** and **GP2**: (i) TBTU (1 equiv.), triethylamine (1 equiv.), **2** (1.5 equiv.), DMSO, 45 °C, 12 h, 44%; (ii) TBTU (1 equiv.), triethylamine (1 equiv.), **3** (1.5 equiv), DMSO, 45 °C, 12 h, 56%. (B) Structures of cisplatin, carboplatin, and the corresponding Pt(IV) complexes **2** and **3**.

Relaxivity measurements. The T_1 relaxivity (r_1) and T_2 relaxivity (r_2) of **1**, **GP1**, and **GP2** were measured at both low (1.41 T) and high (7 T) magnetic field strength in phosphate-buffered saline (PBS) to quantify how well they behave as MR contrast agents. Relaxivity values are summarized in Table 3.1. At 1.41 T, **1** had an r_1 of 4.1 mM^{-1}s^{-1} and an r_2 of 4.6 mM^{-1}s^{-1}. At 7 T, the r_1 had a slight increase while the r_2 significantly increased, as expected at high field. The relaxivity values for **1** are well within the range of what is expected for a small molecule Gd(III) complex.[34] At 1.41 T, **GP1** and **GP2** had an r_1 of 7.0 and 8.8 mM^{-1}s^1 and r_2 of 7.5 and 10.7 mM^{-1}s^{-1} respectively. At 7 T, there was little change in r_1 for both agents, while both r_2 values increased, as expected. Compared to **1**, both **GP1** and **GP2** had significantly increased relaxivity (both r_1 and r_2). This is possibly due to an increase in the rotational correlation time (τ_R) or a change in the inner sphere hydration number (q) of Gd(III). The differences in relaxivity of **GP1** and **GP2** compared to **1** offers the possibility of monitoring reduction of the agents by MR at both high and low field strength. To test this, **GP1**, **GP2**, and **1** were incubated in 5 mM GSH in PBS and the relaxivity was measured (see appendix). The relaxivity of each converged to the same value (r_1 of 4.4, 4.5, and 4.6 mM^{-1}s^{-1} for **1**, **GP1**, and **GP2** respectively), indicating the same Gd(III) species was formed after reduction. The significant change in r_1 upon reduction of **GP1** and **GP2** theoretically could be used to monitor *intracellular* reduction by MR. However, further testing needs to be done to determine if these agents are suitable for this application.

Table 3.1. r_1 and r_2 of **1**, **GP1**, and **GP2** at low (1.41 T) and high (7 T) magnetic field strength in PBS

Agent:	r_1 (mM^{-1}s^{-1})		r_2 (mM^{-1}s^{-1})	
	1.41 T	7 T	1.41 T	7 T
1	4.1	4.7	4.6	6.9
GP1	7.0	7.1	7.5	10.7
GP2	8.8	8.5	9.2	12.4

Stability and reduction of the Gd(III)-Pt(IV) complexes. Though most Pt(IV) complexes (see **2** and **3** in Figure 3.1) are insoluble in most solvents, both **GP1** and **GP2** are readily soluble in aqueous solutions. To ensure both agents remain stable in aqueous media under various conditions, they were dissolved in PBS, two types of cell culture media (MEM and RPMI-1640), pH 5 H$_2$O, and porcine live esterase (PLE) in PBS and monitored over time by HPLC-MS.

Figure 3.2A-B shows that over 48 hours, **GP1** and **GP2** both remained completely stable in PBS and pH 5 H$_2$O. This suggests that both agents can remain intact even in the most acidic conditions in cells, such as in lysosomes (pH 4.5-5).[44] Both agents also remained highly stable in MEM ($\geq$92% intact) at 48 hours. **GP1** and **GP2** were mostly stable in the presence of PLE, and the slight decrease in stability that was observed (~10%) occurred on a much slower timescale than the reduction of both agents by GSH (Figure 3.2C-D). It is unlikely that esterase cleavage is a competing intracellular dissociation mechanism.

In RPMI-1640, 33% of **GP1** and 28% of **GP2** were reduced to Pt(II) within 48 hours. Unlike MEM, which contains no glutathione (GSH), RPMI-1640 has 0.003 mM GSH. Though

this is an extracellularly relevant concentration of GSH (0.002-0.02 mM),[45, 46] a minority of **GP1** and **GP2** are reduced over long periods of time. However, it is important to note that at 6 hours, both agents are ≥96% intact (i.e., they remain in the Pt(IV) oxidation state). *In vivo*, agent that does not get into cells within this time frame will likely be renally cleared before it is reduced. Therefore, within the time frame relevant for *in vivo* experiments, **GP1** and **GP2** stay intact and stable in extracellularly relevant conditions.

Under reducing conditions both agents rapidly converted to a monomeric Gd(III) complex and a Pt(II) drug. Each agent was incubated with 5 mM GSH and 5 mM ascorbate at 37 °C to mimic intracellular conditions. Figure 3.2C-D shows that both agents are rapidly reduced by GSH at these concentrations (≥94% reduction in less than an hour). As expected, **GP1** and **GP2** are also reduced by ascorbate, albeit it at a much slower rate. This is not surprising, as ascorbate is a weaker reducing agent. It is clear from these results that under conditions similar to those inside cells, both agents are reduced, releasing a Gd(III) contrast agent and Pt(II) chemotherapeutic.
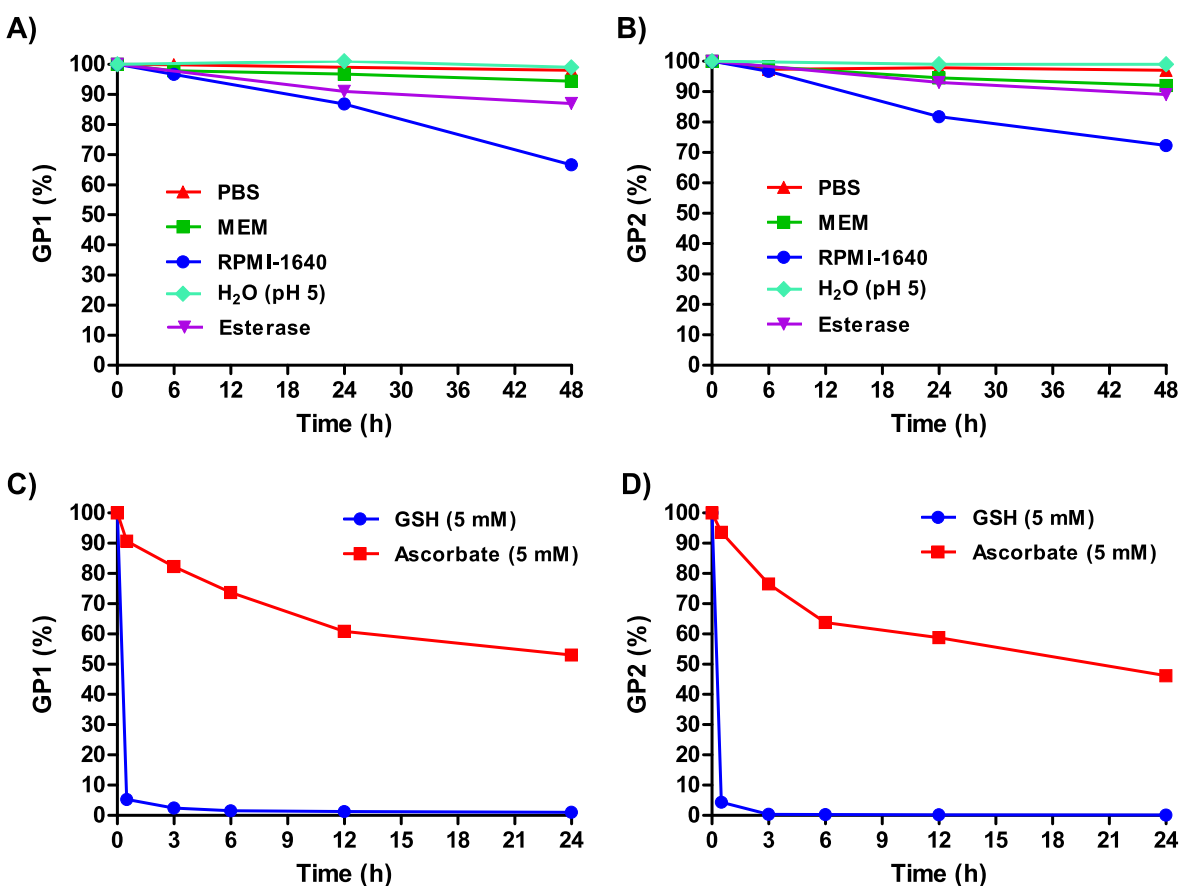
Figure 3.2. Stability of (A) **GP1** and (B) **GP2** in PBS, MEM, RPMI-1640, pH 5 H_2O, and porcine liver esterase (PLE) in PBS. The observed partial reduction over long periods of time in RPMI-1640 is likely a result of glutathione (GSH) in the media. Both agents are highly stable in PBS, MEM, and pH 5 H_2O over extended periods of time while PLE resulted in slight decrease in stability. Stability of (C) **GP1** and (D) **GP2** in 5 mM GSH and 5 mM ascorbate. **GP1** and **GP2** are both rapidly reduced by intracellular concentrations of GSH.

Cytotoxicity of the agents. To assess the cytotoxicity of **GP1** and **GP2** *in vitro*, cell viability assays were performed to determine the IC_{50} concentrations in three cancer cell lines (A2780, HeLa, and MCF-7). Table 3.2 summarizes the IC_{50} concentrations of both agents compared to those of cisplatin and carboplatin. Cells were incubated with cisplatin and **GP1** for 48 h and carboplatin and **GP2** for 72 h to compensate for the inherent decreased potency of carboplatin

compared to cisplatin. **GP1** had an IC_{50} of 29.8 μM in A2780 cells, 49.3 μM in HeLa cells, and 113 μM in MCF-7 cells. For all cell lines, **GP1** was less toxic than cisplatin but followed the same trend of highest toxicity in A2780 cells and least toxic in MCF-7 cells. **GP1** releases cisplatin intracellularly, therefore the apparent difference in toxicity of the two is likely due to decreased cell permeability of **GP1** caused by the Gd(III) complex. However, because **GP1** is inert in the extracellular matrix, higher doses can be safely administered to account for the decreased cell permeability.

 GP2 had an IC_{50} of 55.0 μM in A2780 cells, 258 μM in HeLa cells, and 382 μM in MCF-7 cells. The decreased toxicity is of **GP2** compared to **GP1** is expected because carboplatin is known to be significantly less reactive than cisplatin. **GP2** was similarly less toxic than carboplatin but followed the same trend of highest toxicity in A2780 cells and lowest toxicity in MCF-7 cells. The decreased toxicity compared to carboplatin is again attributed to decreased cell permeability due to the presence of the Gd(III) complex.

 These results demonstrate that **GP1** and **GP2** are cytotoxic in three different cancer cell lines. Both agents show similar trends in toxicity as their Pt(II) analogues, which suggests that upon entering the cells they are reduced and behave like typical Pt(II) chemotherapeutics.

Table 3.2. IC_{50} concentrations of cisplatin, carboplatin, **GP1**, and **GP2** in various cell lines.

Complex	IC_{50} (μM)		
	A2780	**HeLa**	**MCF-7**
Cisplatin:	7.6 ± 2.3	14.7 ± 1.2	22.4 ± 2.0
Carboplatin:	15.3 ± 5.8	71.2 ± 4.9	124 ± 4
GP1:	29.8 ± 2.5	49.3 ± 1.3	113 ± 4
GP2:	55.0 ± 2.9	258 ± 5.0	382 ± 6

Accumulation of the Gd(III)-Pt(IV) agents in cells. Accumulation of **GP1** and **GP2** in cells was measured by concentration-dependent uptake experiments in A2780 and HeLa cells. Individual concentration-dependent uptake graphs are found in the supplementary information. Table 3.3 compares the accumulation of Gd and Pt in A2780 and HeLa cells that were incubated with **GP1**, **GP2**, cisplatin, and carboplatin near their respective IC_{50} concentrations. For comparison, both cell lines were dosed with complex **1** at similar concentrations as **GP1** and **GP2**. The results of these uptake experiments demonstrate several important points. First, the accumulation of Gd in both cell lines for both agents is higher than what is typically considered the amount necessary for detection by MR (high μM concentrations).[32, 33] This suggests that **GP1** and **GP2** can significantly enhance intracellular MR contrast. Typical Gd(III) complexes alone are not cell permeable, therefore the Pt(IV) complexes are making it possible for **GP1** and **GP2** get into cells. This is evidenced by the significant increase in cellular uptake of **GP1** and **GP2** compared to complex **1** in both cell lines.

Second, intracellular Pt levels at the IC_{50} concentrations were similar between **GP1** and cisplatin and **GP2** and carboplatin. From a therapeutic standpoint, the agents behave like cisplatin and carboplatin once they enter cells and are reduced from Pt(IV) to Pt(II). These results support that the higher IC_{50} concentrations of **GP1** and **GP2** compared to cisplatin and carboplatin are caused by decreased cell-permeability, not a decrease in intracellular toxicity. It is clear that both **GP1** and **GP2** penetrate cells well enough to provide sufficient MR relevant Gd(III) concentrations for imaging *and* therapeutically relevant Pt concentrations in cells at low incubation concentrations.

Finally, there is a significant preferential accumulation of Gd(III) compared to Pt from both agents in both cell lines. The difference in accumulation of the two is because they dissociate from one another after the intracellular reduction of Pt(IV) to Pt(II). For **GP1**, a 13-fold higher accumulation of Gd(III) than Pt in A2780 cells and 34-fold higher Gd(III) accumulation in HeLa cells was observed. For **GP2**, Gd(III) accumulation was 3.7-fold higher in both A2780 and HeLa cells. These results suggest that the Gd(III) is effluxed to a lesser extent than Pt. When **GP1** and **GP2** are reduced intracellularly, the cell impermeable charged Gd(III) complex will be prevented from exiting the cells as readily as the cell permeable Pt(II) complexes. This is of particular consequence for the ability of **GP1** and **GP2** to act as MR contrast agents because higher cellular amounts of Gd(III) increase MR contrast.

Table 3.3. Accumulation of Gd and Pt in A2780 and HeLa cells when incubated with **GP1**, **GP2**, cisplatin, and carboplatin near their IC_{50} concentrations and **1** at 100 μM for 24 h.

Compound	Cell Accumulation (fmol/cell)			
	A2780 Cells		HeLa Cells	
	Gd	Pt	Gd	Pt
GP1	2.5 ± 0.3	0.20 ± 0.03	5.7 ± 1.9	0.17 ± 0.01
GP2	1.4 ± 0.2	0.38 ± 0.1	1.1 ± 0.2	0.30 ± 0.06
1	0.26 ± 0.02	N/A	0.21 ± 0.01	N/A
Cisplatin	N/A	0.21 ± 0.02	N/A	0.27 ± 0.02
Carboplatin	N/A	0.22 ± 0.02	N/A	0.60 ± 0.11

Cell uptake of **GP1** and **GP2** was additionally measured in a time-dependent manner in A2780 cells. Figure 3.3 demonstrates that the accumulation of both Gd(III) and Pt from both agents is directly proportional to time. In these experiments, higher accumulation of Gd(III) compared to Pt was observed at every timepoint. Initial uptake of **GP1** and **GP2** from 0-30 min was fast compared to uptake from 0.5-24 h. Fast uptake and intracellular reduction can explain why there was significantly more Gd(III) than Pt even at the 30 min timepoint. For both agents, the Gd:Pt ratio in cells continues to increase over time, which is consistent with a higher rate of efflux of Pt. These results also suggest MR-relevant amounts of Gd(III) from both agents accumulate in cells within a few hours. This is promising for the prospect of imaging within the time frame relevant for *in vivo* experiments.
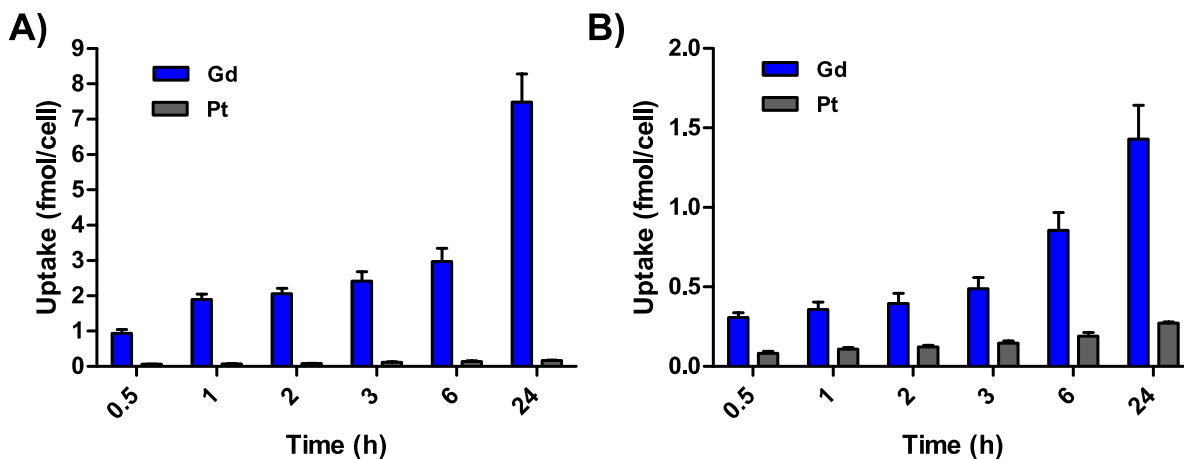
Figure 3.3. (A) Accumulation of Gd(III) and Pt in A2780 cells incubated with 65 μM **GP1** over time. (B) Accumulation of Gd(III) and Pt in A2780 cells incubated with 62.5 μM **GP2** over time. In both cases, accumulation of Gd(III) was significantly higher than Pt.

MR imaging of A2780 and HeLa cell pellets. To quantify the ability of **GP1** and **GP2** to enhance

MR contrast intracellularly, MR cell pellet imaging experiments were performed. A2780 and HeLa

cells were incubated with IC_{50} concentrations of **GP1** and **GP2** for 6 hours then imaged in a 7 T

MR scanner. The relaxation rate (R_1), which is defined as $1/T_1$ and is directly proportional to MR

contrast, of each cell pellet was determined and compared to control cells that were untreated,

incubated with 100 μM complex **1**, or incubated with IC_{50} concentrations of cisplatin.

Figure 3.4 demonstrates that **GP1** and **GP2** significantly enhance the intracellular MR

contrast of both A2780 and HeLa cells when dosed at concentrations near the IC_{50}. **GP1** increased

the R_1 by 36% in A2780 cells and 48% in HeLa cells compared to the untreated controls. **GP2**

increased the R_1 by 26% in A2780 cells 23% in HeLa cells. Treating cells with similar

concentrations of complex **1** and IC_{50} concentrations of cisplatin resulted in minimal increases in

R_1. This supports that the observed contrast enhancement by **GP1** and **GP2** is a result of the agents

effectively accumulating in cells, something **1** cannot do alone. Furthermore, any physiological

changes in the cells caused by the presence of a Pt(II) drug have little effect on the MR contrast. Therefore, the contrast enhancement is a result of intracellular Gd(III).

Notably, the cell pellet experiments were performed within a time frame relevant for *in vivo* MR imaging (6 hours). These results are very promising for the prospect of using Gd(III)-Pt(IV) theranostics like **GP1** and **GP2** for *in vivo* MR imaging.
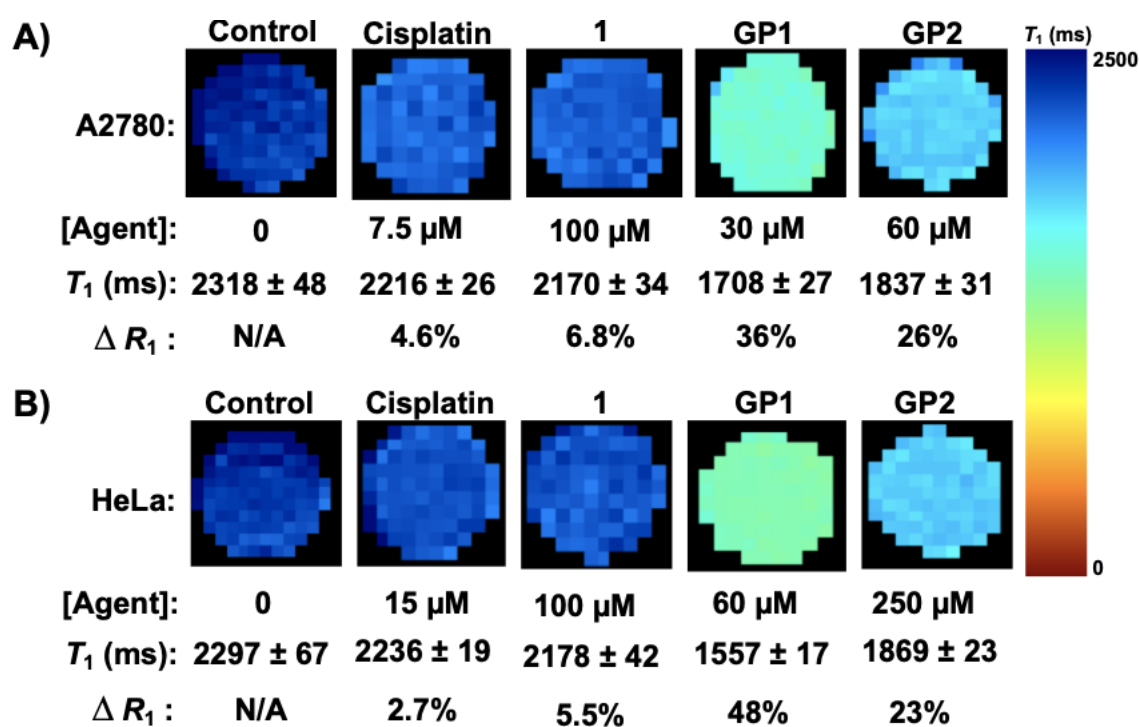
Figure 3.4. (A) MR imaging of A2780 cell pellets at 7 T. IC_{50} concentrations of **GP1** and **GP2** significantly enhanced the intracellular contrast of A2780 cells (increase in R_1) compared to the untreated control cells while **1** and cisplatin had a minimal effect. (B) MR imaging of HeLa cell pellets at 7 T. IC_{50} concentrations of **GP1** and **GP2** significantly enhanced the intracellular contrast of HeLa cells compared to the untreated control cells while **1** and cisplatin had a minimal effect.

3.3 Conclusions

We have described the synthesis, characterization and cellular uptake of two new Gd(III)-Pt(IV) agents. **GP1** and **GP2** represent the first examples of Gd(III)-Pt(IV) agents that are simultaneously MR contrast agents and are reduced to provide chemotherapy. Of the two agents, **GP1** is most promising as it exhibits greater cellular toxicity, higher intracellular accumulation of Gd(III) and better MR contrast enhancement *in vitro*. Future work will focus on demonstrating the *in vivo* efficacy of these agents for both imaging *and* treatment.

CHAPTER 4

DEVELOPMENT OF Ca^{2+} RESPONSIVE MR CONTRAST AGENTS WITH HIGH CELLULAR UPTAKE AND NIR FLUORESCENCE

4.1 Introduction

Ca(II) is involved in nearly all significant cellular events, including the maintenance of membrane potential, propagation of action potential, signal transduction, transcription, and apoptosis.[1-5] In the central nervous system (CNS), Ca(II) plays a crucial role in the proper function of neurons by contributing to synaptic signaling (the release of neurotransmitters), excitability, and the regulation of neuronal plasticity.[6,7] As a result of these essential functions, the dysregulation of Ca(II) is associated with various pathologic conditions, including seizures, ischemia, and hypoglycemia, all of which lead to neurodegeneration and neuronal cell death.[8-14] The impact of Ca(II) on neuronal function has led to the development of several techniques for detecting and imaging changes in Ca(II) concentrations (or Ca(II) flux), in vivo. Mammalian cells maintain a large gradient of unbound Ca(II), with extracellular concentrations of ~2 mM and intracellular concentrations of ~100 nM.[1-7] During an action potential, Ca(II) influx drastically increases the intracellular concentration, therefore imaging changes in Ca(II) can provide an ideal readout of neuronal activity.

Previous in vivo imaging of Ca(II) has commonly utilized Ca(II) sensitive fluorescent dyes or blood-oxygen-level-dependent (BOLD) contrast generated from functional magnetic resonance imaging (fMRI).[15-23] More recently, genetically encoded calcium indicators (GECIs) consisting of fluorescent fusion proteins have been de-veloped.[24-26] Though these techniques have provided important information about Ca(II) signaling, several inherent disadvantages hinder their ability to produce high resolution, real-time imaging of Ca(II) flux in vivo.

Optical techniques are limited by sample depth and opacity, making non-invasive in vivo imaging difficult.[27, 28] fMRI has excellent depth penetration, but changes in BOLD contrast are not

necessarily caused by Ca(II) and are indirect because they arise from changes in blood flow, volume, and oxygenation.[18,29] Additionally, the temporal resolution of BOLD imaging is restricted by the delay necessary to generate changes in circulation after neuronal firing. Though GECIs can be used to image subcellular structures and are compatible with long term in vivo imaging, they require introduction of an encoding gene through transgenesis or viral constructs.

The limitations of these techniques for imaging neuronal activity in deep brain regions in vivo may be over-come through the use of contrast-enhanced magnetic resonance imaging.[30] In order to image Ca(II) flux using contrast-enhanced MR imaging, our lab and others have developed bioresponsive agents that generate in-creased MR contrast through interaction with Ca(II) ions.[31-39] The majority of these agents image changes in the extracellular Ca(II) pool. However, the decrease in extracellular Ca(II) caused by neuronal signaling is minimal because of the high extracellular concentration whereas the increase in intracellular Ca(II) is significant.

There are two examples of MR agents designed to im-age changes in intracellular Ca(II).[33,37] Our lab developed the first Ca(II) bioresponsive MR contrast agents that are activated by intracellular concentrations from 1-10 µm.[31-33] The agents consist of two paramagnetic Gd(III) complexes (1,4,7,10-tetraazacycloddodecane-1,4,7-triacetic acid, Gd(III)-DO3A) conjugated to the well-established Ca(II) binding domain 1,2,bis(O-aminophenoxy) ethane-N,N,N',N'-tetraacetic acid (BAPTA). Regiospecific back-binding to Gd(III) from carboxylate groups of BAPTA coordinatively saturates Gd(III) and blocks water coordination (q) at Ca(II) con-centrations below 1 µM, resulting in a lower relaxivity "off" state. At Ca(II) concentrations greater than 1 µM, the carboxylates of BAPTA preferentially bind Ca(II), which increases q and therefore the T_1 relaxivity (r_1) of each Gd(III) complex. This platform allows for the detection of intracellular

Ca(II) flux at low concentrations (1-10 µM). However, the ability of our previously developed agents to effectively detect intracellular Ca(II) in vivo has been limited by cellular uptake of previous agents.[33]

To address this limitation, we have designed and synthesized a series of new agents that are conjugated to a near infrared (NIR) fluorescent dye, IR-783 (Figure 4.1.) IR-783 has been shown to significantly increase the up-take of many small molecules (including Gd(III) complexes) via organic anion transporter polypeptides (OATPs).[40] In addition to increasing cellular uptake, IR-783 enables NIR fluorescence imaging for optical co-registration of uptake and location of the agent both in vitro and in vivo.[41, 42]

Therefore, by incorporation of IR-783 to our Ca(II) responsive platform, we have developed a series of multimodal MR and NIR fluorescence agents capable of detecting intracellular Ca(II) changes that exhibits very high cellular uptake. This advance is a crucial step towards the goal of successfully imaging intracellular Ca(II) flux in vivo, which could have a significant impact on the ability to study brain function and pathologic states stemming from Ca(II) dysregulation.
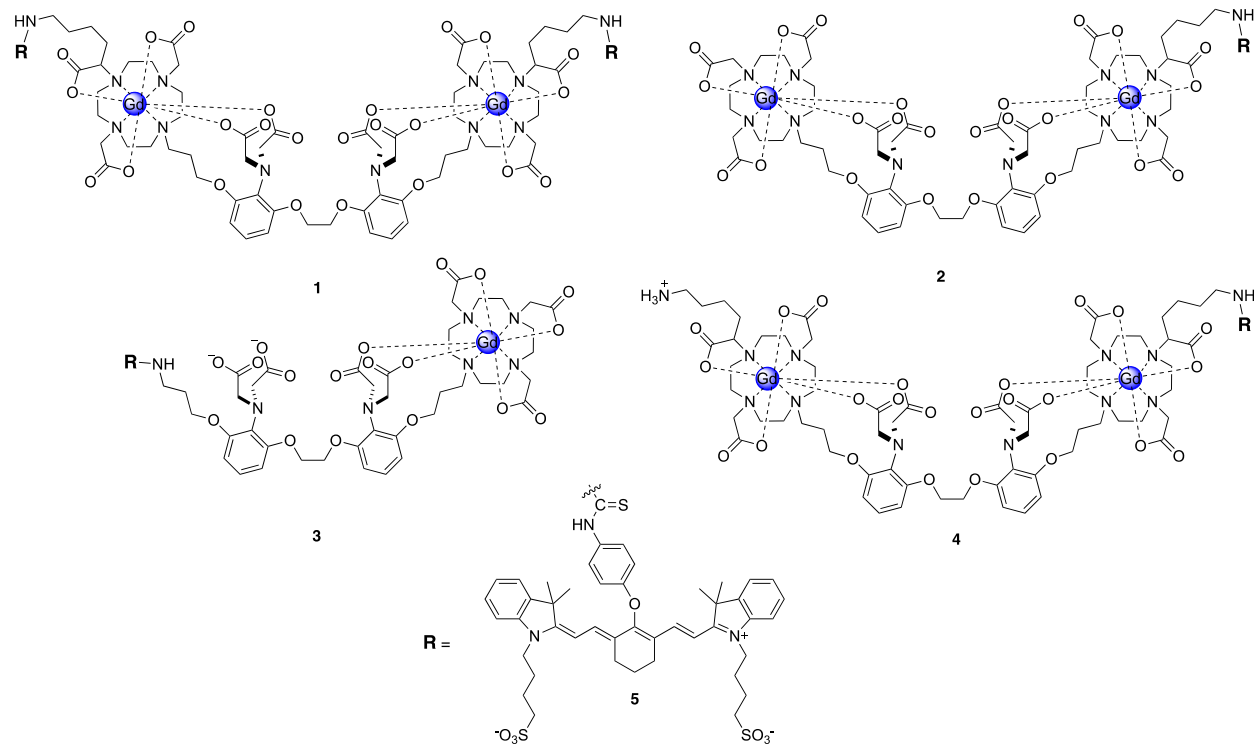
Figure 4.1. Structures of the Ca(II) bioresponsive multimodal MR contrast agents, **1-4**. Incorporation of a NIR dye (IR-783) dramatically increases cellular uptake and allows for simultaneous detection by NIR fluorescence imaging. **1-4** were synthesized by varying the number of Gd(III) and IR-783 moieties to determine the architecture that exhibits the greatest cellular uptake and most favorable MR/optical imaging properties.

4.2 Results and Discussion
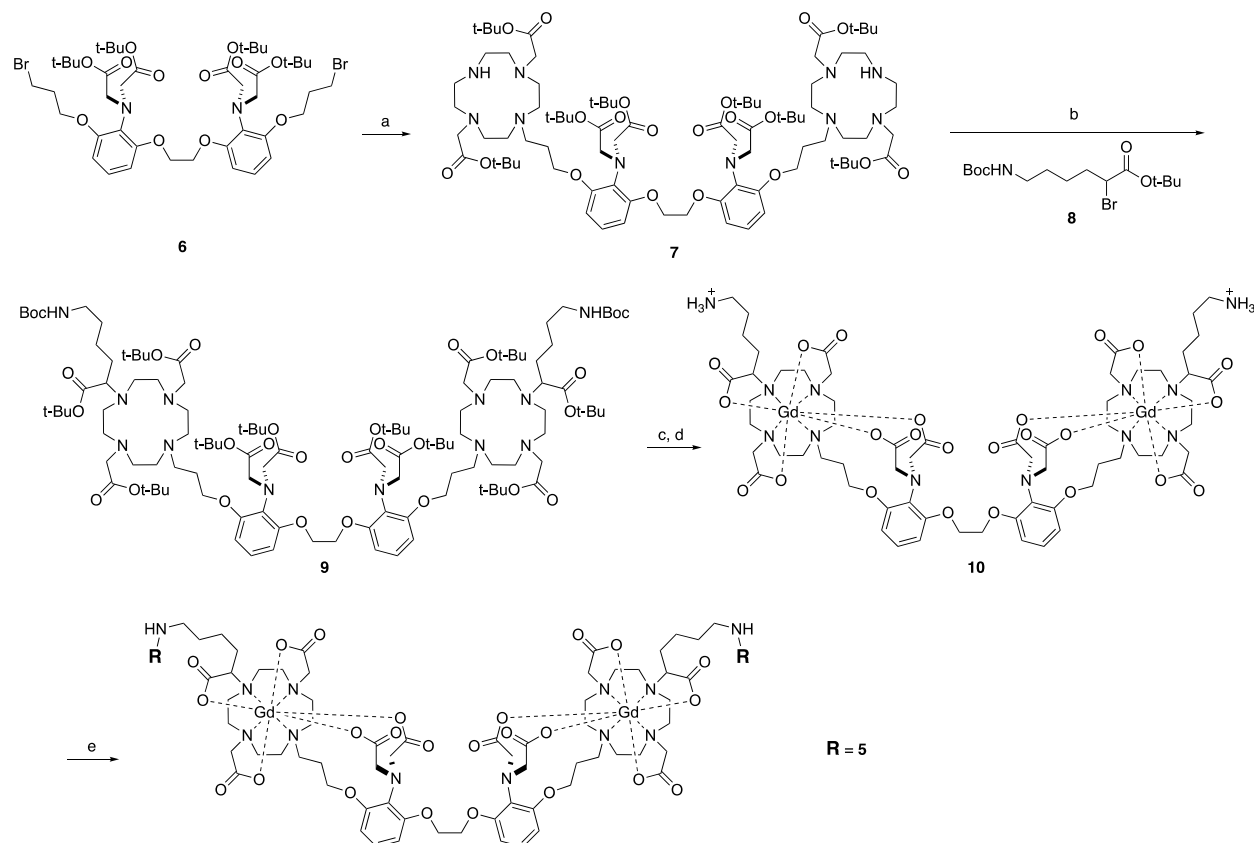
Scheme 4.1. Synthetic scheme of IR-783 conjugated complex **1**. (a) Bis-t-butyl DO2A, K$_2$CO$_3$, MeCN, 60 °C, 30%. (b) **8**, K$_2$CO$_3$, MeCN, 50 °C. (c) Formic acid, 40 °C, 75% (over 2 steps). (d) GdCl$_3$, NaOH, pH 5-6.5, 40 °C. (e) **5**, DMSO/MeCN/100 mM Na$_2$CO$_3$, 14% (over 2 steps). Compounds **5** and **8** were synthesized following adapted literature protocols.

Synthesis and Characterization. Four multimodal contrast agents (**1-4**) were synthesized and characterized (Scheme 4.1.) **1-4** each consist of three moieties: BAPTA, one or more Gd(III) chelates, and optical dye, IR-783. BAPTA was chosen as a Ca(II) binding domain because it exhibits a 10^5-fold selectivity for Ca(II) over other cations such as Mg(II) and protons.[31, 32, 43] Protected cyclen-based macrocycles for coordination to Gd(III) were attached through reaction

with the brominated BAPTA binding domain, **6**. Subsequent deprotection and metalation resulted in Gd(III) intermediate complexes (**10**, **S5**, **S7**), which were then conjugated to IR-783-NCS, **5**, through NCS coupling reactions to afford agents **1-4**. The complexes were purified by semi-preparative reverse-phase HPLC in basic conditions and were characterized via analytical HPLC-MS.

Effect of Ca(II) Binding on Relaxivity. Relaxivities (r_1) of **1-4** were measured at pH 7.40 in 0.1 M HEPES buffer with 0.1 M KCl in the absence and presence of Ca(II) (0-100 μM). Upon addition of CaCl$_2$, all agents precipitated out of solution, likely because binding Ca(II) neutralizes two negative charges on the molecules, promoting aggregation of the IR-783 moieties, which are prone to self-aggregation.[42, 44] To overcome the aggregation of the complexes, 1% DMSO and 5% Tween 80 were added to the solutions. In the absence of Ca(II), the ionic r_1 (r_1 per Gd(III) ion) of **1** at 1.41 T was found to be 26.4 mM^{-1} s^{-1} (Table 4.1.) In the presence of 100 μM Ca(II), **3** instantly precipitated, **2** displayed a decrease in r_1 due to the formation of insoluble aggregates, and **4** displayed an initial increase in r_1, but precipitated out of solution after 24 h. However, **1** remained soluble in the presence of Ca(II). T_1 and T_2 measurements of solutions of **1** in the presence of 100 μM Ca(II) were repeated after 24, 48, and 72 h. At these time points, no changes in T_1 or T_2 were observed indicating **1** remains soluble over time. Any changes in solubility or aggregation would likely have changed the observed T_1 or T_2 at 1.41 T.

In the presence of 100 μM Ca(II), the r_1 of **1** was found to be 36.3 mM^{-1} s^{-1} at 1.41 T. This represents a 38% increase in response to the presence of Ca(II). At 7 T, **1** had an r_1 of 2.2 mM^{-1} s^{-1} without Ca(II) and 4.7 mM^{-1} s^{-1} in the presence of 100 μM Ca(II), representing a 114% increase.

The increase in r_1 in response to Ca(II) at 7 T was markedly higher than the increase at 1.41 T, therefore all *in vitro* MR imaging was performed at 7 T.

The r_1 of **1** (0-0.8 mM) was then measured at varying concentrations of Ca(II) (see appendix). Importantly, the data show the dynamic range of response to Ca(II) for **1** is between 1 and 10 μM with an EC50 of 3.6 μM (i.e., the intracellular concentration of *in vivo* Ca(II)). This dynamic range is consistent with previous BAPTA-based Ca(II) responsive agents investigated in our lab.[31-33]

Table 4.1. Relaxivity (r_1) of complex **1** at low (1.41 T) and high (7 T) magnetic field strength with and without Ca(II).

Complex	r_1 (1.41 T)		r_1 (1.41 T, 100 μM Ca(II))		r_1 (7 T)		r_1 (7 T, 100 μM Ca(II))	
	ionic (mM^{-1} s^{-1})	Molecular (mM^{-1} s^{-1})	ionic (mM^{-1} s^{-1})	Molecular (mM^{-1} s^{-1})	ionic (mM^{-1} s^{-1})	Molecular (mM^{-1} s^{-1})	ionic (mM^{-1} s^{-1})	Molecular (mM^{-1} s^{-1})
1	26.4 ± 1.0	52.8 ± 2.0	36.3 ± 0.6	72.6 ± 1.2	2.2 ± 0.2	4.4 ± 0.4	4.7 ± 0.8	9.6 ± 1.6

All values reported were measured in pH 7.40 0.1 M HEPES buffer with 0.1 M KCl, 1% DMSO and 5% Tween 80 at 37 °C.

***In Vitro* Toxicity, Uptake and Retention.** Although cytotoxic amounts of Tween 80 were used to measure r_1 in solution, this does not impact *in vitro* experiments because **1** is *readily* soluble in cell media (DMEM or MEM + 10% FBS). Cell media is not an attractive choice for measuring r_1 because of the inherently high concentrations of Ca^{2+} and Zn^{2+}, making it difficult to measure the r_1 of the "off" state of the agent.

In vitro experiments were performed using HT-22 hippocampal neuronal cells and U-87 MG glioblastoma cells. HT-22 cells were chosen because they are commonly used to study neuronal function while U-87 MG cells were chosen as a second brain cell line to validate the toxicity and uptake of **1**.[45, 46] Toxicity of **1** was assessed by incubating cells with concentrations ranging from 0-100 μM for 24 h (see appendix). In both HT-22 and U-87 MG cells, **1** was well tolerated at concentrations up to 20 μM ($\geq$ 88% cell viability). For this reason, all further *in vitro* experiments were performed using $\leq$ 20 μM **1**.

Concentration-dependent uptake was determined by incubating cells with 0-20 μM **1** for 24 h. Figure 4.2 shows that at low incubation concentrations ranging from 5-20 μM, both HT-22 and U-87 MG cells displayed high uptake of Gd(III) (>2-16 femtomoles per cell). These values all correspond to cellular concentrations in the millimolar range (assuming a cell volume of ~2 picoliters) which is well above the amount necessary for detection by MR.[27, 28, 47] The uptake of **1** is greatly improved compared to previous Ca(II) responsive contrast agents even when dosed at much lower concentrations.[33] In order to characterize the subcellular localization of the agent, cell fractionation experiments were performed in HT-22 cells incubated with 10 μM **1** (see appendix). These experiments demonstrate the *nearly all* of the agent (95%) is located in the cytosol. These results demonstrate the ability of the agent to access intracellular Ca(II) upon an influx.
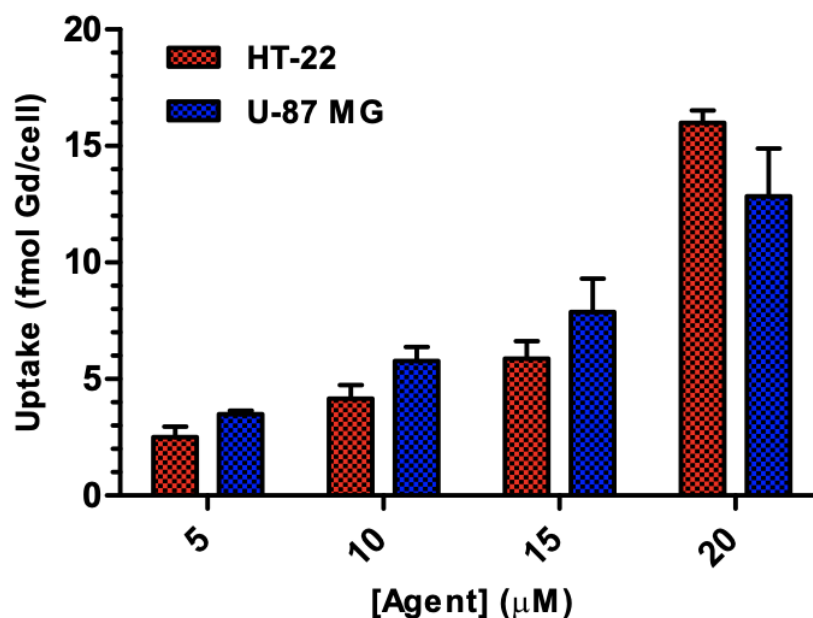
Figure 4.2. Concentration-dependent uptake of **1** in HT-22 and U-87 MG cells after 24 h. Data are the mean ± one standard deviation of three runs. **1** exhibits drastically higher cellular uptake compared to previous BAPTA based agents.

Time-dependent uptake in HT-22 cells was performed to determine how quickly MR-relevant concentrations of Gd(III) accumulate intracellularly. Cells were incubated with 10 μM **1** for times ranging from 0.5-24 h and uptake of Gd(III) was determined at each timepoint. Figure 4.3 demonstrates that uptake of **1** increases over time. More importantly, in just 30 min, uptake of >2 fmol/cell was observed, indicating MR-relevant concentrations of **1** rapidly accumulate intracellularly.

To determine if **1** remains internalized in cells, a leaching experiment was performed. HT-22 cells were incubated with 10 μM **1** for 24 h, after which the media was removed, the cells were
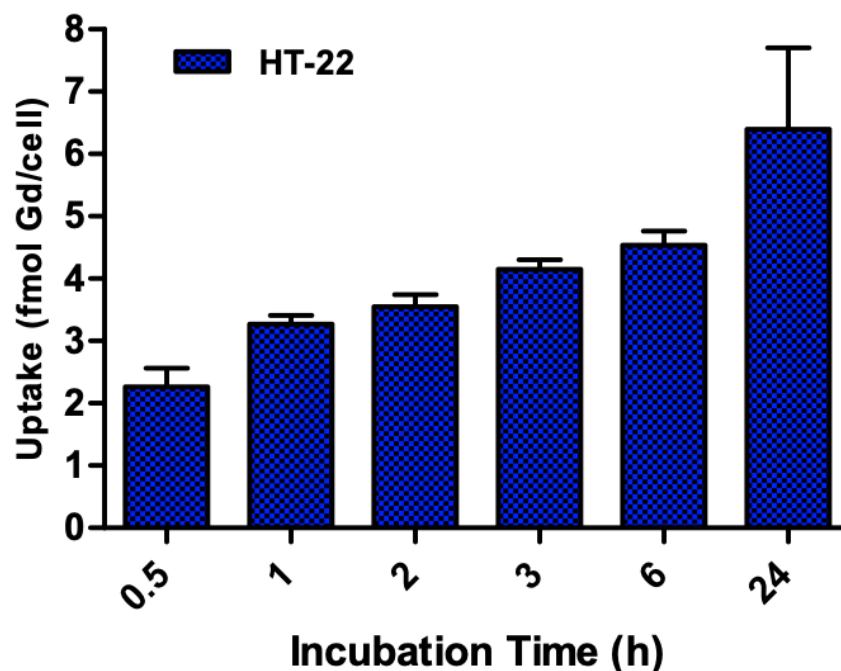
Figure 4.3. Time-dependent uptake of Gd(III) in HT-22 cells treated with 10 μM **1**. Data are the mean ± one standard deviation of three runs. MR-relevant concentrations of Gd(III) rapidly accumulate in HT-22 cells (>2 fmol/cell in 30 min) followed by increased uptake over time.

washed with DPBS 3x and fresh media was added. The cells were incubated in the fresh media for varying amounts of time (0, 3, 6, 12, and 24 h), and at each time point the media was collected and analyzed by ICP-MS to determine the amount of Gd(III) that leached. From 0-3 h, 25% of Gd(III) was lost to leaching; However, from 3-24 h a non-significant amount of Gd(III) leached. The initial loss of Gd(III) is likely due to non-specifically bound agent on the cell surface, as the cells could not be centrifuged because they were adhered to the plate. Nevertheless, these data demonstrate that the majority of **1** is retained over 24 h, which is a suitable timeframe for *in vivo* imaging.

***In Vitro* MR Imaging.** To quantify the increase in MR image contrast induced by the accumulation of **1**, HT-22 cells were incubated with 10 μM **1** for 30 min or 24 h, centrifuged into capillaries, and imaged using a 7 T MR spectrometer. The control cell pellet (no agent) had a T_1 of 2051 ± 15 ms while the cells incubated with **1** for 30 min and 24 h had a T_1 of 1610 ± 14 ms and 987 ± 12 ms (Figure 4.4). These values correspond to an increase in R_1 ($1/T_1$, proportional to the signal) of 27% and 107% compared to the control (Figure 4.5.) These data indicate **1** can quickly accumulate in cells and significantly increase MR contrast in as little as 30 min, with even more profound increases in contrast at longer incubation times.
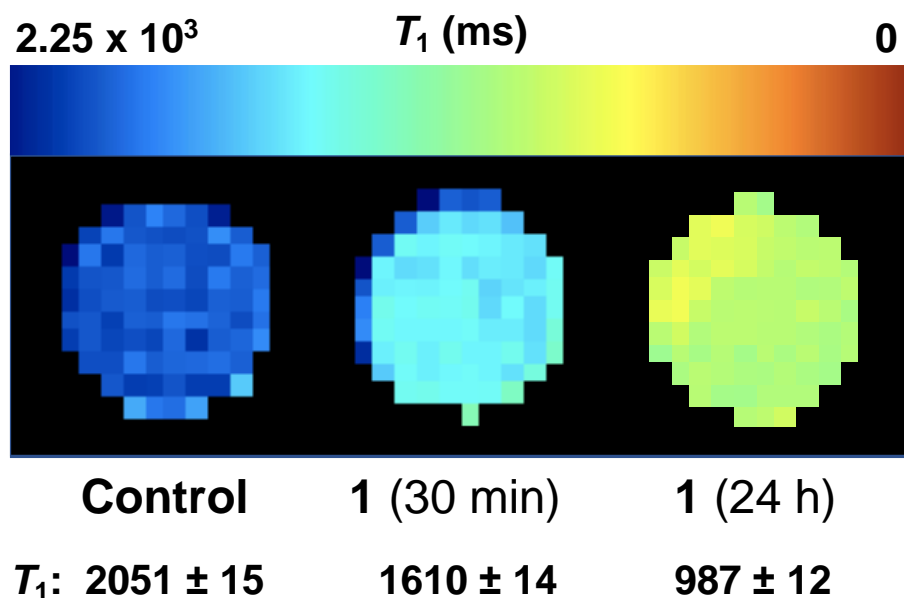
Figure 4.4. T_1 map of MR images of HT-22 cell pellets. Cells were untreated (control) or incubated with 10 μM **1** for 30 min or 24 h. **1** significantly lowered the T_1 of HT-22 cells at both incubation times, indicating rapid, high cellular uptake.

To test if **1** can respond to intracellular Ca(II) changes *in vitro*, a Ca(II) ionophore, calcimycin, was used in the same HT-22 cell pellet MR experiments. Control cells (no agent) and cells incubated with 10 μM **1** for 24 h were treated with 10 μM calcimycin (in pH 7.40 0.1 M HEPES buffer with 0.1 M KCl and 2 mM $CaCl_2$), pelleted, and imaged at 7 T (see appendix). Cells treated with calcimycin alone had a T_1 of 2066 ± 17 ms, a non-significant change from the control cells without calcimycin. However, cells incubated with **1** for 24 h that were then treated with calcimycin had a T_1 of 925 ± 13 ms, which represents a 121% increase in R_1 compared to the control (Figure 4.5.) This increase in R_1 is 14% higher than the increase observed for cells incubated with **1** for 24 h that were not treated with calcimycin. Thus, increasing the intracellular Ca(II) concentration resulted in a significant increase in MR contrast ($p < 0.01$) in cells labeled with **1**. This demonstrates that **1** can indeed detect changes in intracellular Ca(II), even at relatively low concentrations.

To further support that the observed changes in MR signal are due to **1** binding Ca(II), HT-22 cells were incubated with a Ca(II)-insensitive analogue (**S1**) and imaged at 7 T (see appendix). Half of these labeled cells were treated with 10 μM calcimycin while the rest were untreated. Treatment with calcimycin did not shorten the observed T_1. Therefore, the observed decrease in T_1 by **1** is due Ca(II) binding and not calcimycin.
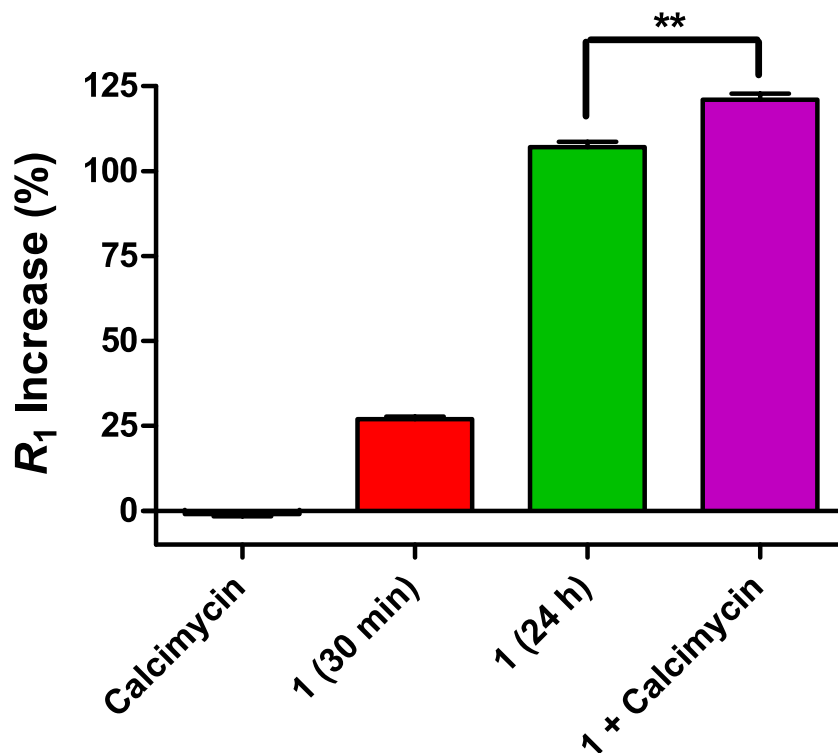
Figure 4.5. Percent increase of R_1 of HT-22 cell pellets imaged at 7 T compared to untreated (control) cells. Cells were treated with 10 μM calcimycin alone, 10 μM **1** for 30 min, 10 μM **1** for 24 h, or 10 μM **1** for 24 h followed by 10 μM calcimycin. Cells treated with calcimycin alone showed no significant change in R_1, but all cells incubated with **1** had significant increases. Cells incubated with **1** and treated with calcimycin (purple) showed a significant increase (p < 0.01) in R_1 compared to the same cells that were not treated with calcimycin (green), indicating **1** responds to intracellular Ca(II) changes.

***In Vitro* Fluorescence Imaging.** In addition to significantly improving cellular uptake, incorporation of IR-783 allows for detection by fluorescence imaging at NIR wavelengths. To assess the ability of **1** to be detected by fluorescence imaging, HT-22 cells were imaged using a two-photon confocal microscope and an IVIS Spectrum.

Plated cells and cell pellets used for MR imaging were additionally imaged using an IVIS Spectrum and compared to HT-22 cells without agent (see appendix). These images demonstrate

that **1** can be detected by NIR fluorescence imaging *in vitro* even at higher concentrations than are required by MR imaging.

For confocal microscopy, cells were plated on a FluoroDish and incubated with 10 μM of **1** for 24 h, after which the cells were washed (3x) with DPBS and fresh media was added. The confocal micrographs in Figure 4.6 demonstrate that **1** accumulates intracellularly in HT-22 cells and can be detected by NIR fluorescence imaging at the same concentrations compatible with MR imaging.

The results of these *in vitro* experiments support our hypothesis that incorporation of IR-783 onto BAPTA-based Ca(II) responsive contrast agents significantly increases cellular uptake while enabling detection by NIR fluorescence imaging.
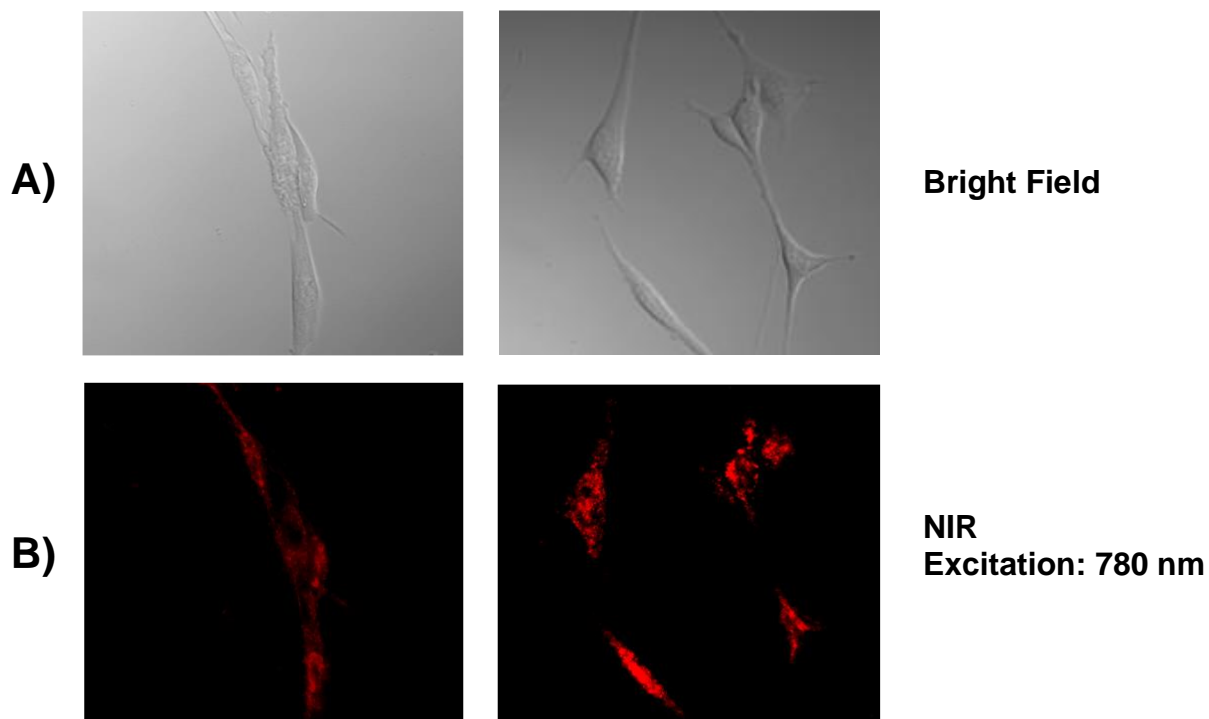
Figure 4.6. Confocal micrographs of HT-22 cells incubated with 10 μM **1** for 24 h. A) Bright field images of the HT-22 cells treated with **1**. B) Fluorescence images of the same HT-22 cells treated with **1** using an excitation wavelength of 780 nm. The overlap of the bright field and fluorescence images indicates **1** has the ability to accumulate intracellularly and is easily detected by fluorescence imaging at NIR wavelengths.

4.3 Conclusions

We have synthesized a series of Ca(II) responsive MR imaging contrast agents that incorporate a NIR dye (IR-783) that substantially increases the cellular uptake of the Ca(II)-responsive MR agents while simultaneously providing a fluorescence signal. Complex **1** demonstrated the most promising results and exhibited a very large increase in r_1 (114%) in solution when activated in the presence of Ca(II) at 7 T. At concentrations between 0-20 µM, **1** was well tolerated by HT-22 and U-87 MG cells (≥88% viability) and showed rapid, drastically increased cellular uptake compared to previous Ca(II) responsive MR contrast agents. At concentrations ≤ 10 µM, **1** was detectable *in vitro* by both MR and NIR fluorescence imaging and showed significantly increased MR contrast in response to intracellular Ca(II) changes. This new series of multimodal and bioresponsive MR probes is currently being evaluated *in vivo* using stereotaxic microinjection techniques to measure Ca(II) flux in whole animals.

REFERENCES

Chapter 1 References

1. James, M. L.; Gambhir, S. S., A molecular imaging primer: modalities, imaging agents, and applications. *Physiol Rev* **2012,** *92* (2), 897-965.

2. Massoud, T. F.; Gambhir, S. S., Molecular imaging in living subjects: seeing fundamental biological processes in a new light. *Genes Dev* **2003,** *17* (5), 545-80.

3. Pysz, M. A.; Gambhir, S. S.; Willmann, J. K., Molecular imaging: current status and emerging strategies. *Clin Radiol* **2010,** *65* (7), 500-516.

4. Weissleder, R., Molecular imaging in cancer. *Science* **2006,** *312* (5777), 1168-71.

5. Alexander, V. M.; Choyke, P. L.; Kobayashi, H., Fluorescent molecular imaging: technical progress and current preclinical and clinical applications in urogynecologic diseases. *Curr Mol Med* **2013,** *13* (10), 1568-1578.

6. Peterson, J. D., Paradigms in Fluorescence Molecular Imaging: Maximizing Measurement of Biological Changes in Disease, Therapeutic Efficacy, and Toxicology/Safety. *Molecular Imaging and Biology* **2019,** *21* (4), 599-611.

7. Fouquet, C.; Gilles, J.-F.; Heck, N.; Dos Santos, M.; Schwartzmann, R.; Cannaya, V.; Morel, M.-P.; Davidson, R. S.; Trembleau, A.; Bolte, S., Improving axial resolution in confocal microscopy with new high refractive index mounting media. *PLoS One* **2015,** *10* (3), e0121096-e0121096.

8. Marshall, M. V.; Rasmussen, J. C.; Tan, I. C.; Aldrich, M. B.; Adams, K. E.; Wang, X.; Fife, C. E.; Maus, E. A.; Smith, L. A.; Sevick-Muraca, E. M., Near-Infrared Fluorescence

Imaging in Humans with Indocyanine Green: A Review and Update. *Open Surg Oncol J* **2010,** *2* (2), 12-25.

9.   Guo, Z.; Park, S.; Yoon, J.; Shin, I., Recent progress in the development of near-infrared fluorescent probes for bioimaging applications. *Chemical Society Reviews* **2014,** *43* (1), 16-29.

10.   Vahrmeijer, A. L.; Hutteman, M.; van der Vorst, J. R.; van de Velde, C. J. H.; Frangioni, J. V., Image-guided cancer surgery using near-infrared fluorescence. *Nature Reviews Clinical Oncology* **2013,** *10* (9), 507-518.

11.   Pimlott, S. L.; Sutherland, A., Molecular tracers for the PET and SPECT imaging of disease. *Chem Soc Rev* **2011,** *40* (1), 149-62.

12.   Ametamey, S. M.; Honer, M.; Schubiger, P. A., Molecular imaging with PET. *Chem Rev* **2008,** *108* (5), 1501-16.

13.   Wei, W.; Rosenkrans, Z. T.; Liu, J.; Huang, G.; Luo, Q.-Y.; Cai, W., ImmunoPET: Concept, Design, and Applications. *Chemical Reviews* **2020,** *120* (8), 3787-3851.

14.   Ehman, E. C.; Johnson, G. B.; Villanueva-Meyer, J. E.; Cha, S.; Leynes, A. P.; Larson, P. E. Z.; Hope, T. A., PET/MRI: Where might it replace PET/CT? *J Magn Reson Imaging* **2017,** *46* (5), 1247-1262.

15.   Lusic, H.; Grinstaff, M. W., X-ray-computed tomography contrast agents. *Chemical reviews* **2013,** *113* (3), 1641-1666.

16.   Li, H.; Meade, T. J., Molecular Magnetic Resonance Imaging with Gd(III)-Based Contrast Agents: Challenges and Key Advances. *Journal of the American Chemical Society* **2019,** *141* (43), 17025-17041.

17. Wahsner, J.; Gale, E. M.; Rodríguez-Rodríguez, A.; Caravan, P., Chemistry of MRI Contrast Agents: Current Challenges and New Frontiers. *Chem Rev* **2019,** *119* (2), 957-1057.

18. Grobner, T., Gadolinium--a specific trigger for the development of nephrogenic fibrosing dermopathy and nephrogenic systemic fibrosis? *Nephrol Dial Transplant* **2006,** *21* (4), 1104-8.

19. Marckmann, P.; Skov, L.; Rossen, K.; Dupont, A.; Damholt, M. B.; Heaf, J. G.; Thomsen, H. S., Nephrogenic systemic fibrosis: suspected causative role of gadodiamide used for contrast-enhanced magnetic resonance imaging. *J Am Soc Nephrol* **2006,** *17* (9), 2359-62.

20. Kanda, T.; Fukusato, T.; Matsuda, M.; Toyoda, K.; Oba, H.; Kotoku, J.; Haruyama, T.; Kitajima, K.; Furui, S., Gadolinium-based Contrast Agent Accumulates in the Brain Even in Subjects without Severe Renal Dysfunction: Evaluation of Autopsy Brain Specimens with Inductively Coupled Plasma Mass Spectroscopy. *Radiology* **2015,** *276* (1), 228-32.

21. Kanda, T.; Ishii, K.; Kawaguchi, H.; Kitajima, K.; Takenaka, D., High signal intensity in the dentate nucleus and globus pallidus on unenhanced T1-weighted MR images: relationship with increasing cumulative dose of a gadolinium-based contrast material. *Radiology* **2014,** *270* (3), 834-41.

22. Prince, M. R.; Zhang, H.; Zou, Z.; Staron, R. B.; Brill, P. W., Incidence of immediate gadolinium contrast media reactions. *AJR Am J Roentgenol* **2011,** *196* (2), W138-43.

23. Loving, G. S.; Mukherjee, S.; Caravan, P., Redox-activated manganese-based MR contrast agent. *J Am Chem Soc* **2013,** *135* (12), 4620-3.

24.   Gale, E. M.; Atanasova, I. P.; Blasi, F.; Ay, I.; Caravan, P., A Manganese Alternative to Gadolinium for MRI Contrast. *Journal of the American Chemical Society* **2015,** *137* (49), 15548-15557.

25.   Wang, J.; Wang, H.; Ramsay, I. A.; Erstad, D. J.; Fuchs, B. C.; Tanabe, K. K.; Caravan, P.; Gale, E. M., Manganese-Based Contrast Agents for Magnetic Resonance Imaging of Liver Tumors: Structure–Activity Relationships and Lead Candidate Evaluation. *Journal of Medicinal Chemistry* **2018,** *61* (19), 8811-8824.

26.   Kálmán, F. K.; Nagy, V.; Váradi, B.; Garda, Z.; Molnár, E.; Trencsényi, G.; Kiss, J.; Même, S.; Même, W.; Tóth, É.; Tircsó, G., Mn(II)-Based MRI Contrast Agent Candidate for Vascular Imaging. *J Med Chem* **2020,** *63* (11), 6057-6065.

27.   Wang, H.; Jordan, V. C.; Ramsay, I. A.; Sojoodi, M.; Fuchs, B. C.; Tanabe, K. K.; Caravan, P.; Gale, E. M., Molecular Magnetic Resonance Imaging Using a Redox-Active Iron Complex. *Journal of the American Chemical Society* **2019,** *141* (14), 5916-5925.

28.   Snyder, E. M.; Asik, D.; Abozeid, S. M.; Burgio, A.; Bateman, G.; Turowski, S. G.; Spernyak, J. A.; Morrow, J. R., A Class of FeIII Macrocyclic Complexes with Alcohol Donor Groups as Effective T1 MRI Contrast Agents. *Angewandte Chemie International Edition* **2020,** *59* (6), 2414-2419.

29.   Asik, D.; Smolinski, R.; Abozeid, S. M.; Mitchell, T. B.; Turowski, S. G.; Spernyak, J. A.; Morrow, J. R., Modulating the Properties of Fe(III) Macrocyclic MRI Contrast Agents by Appending Sulfonate or Hydroxyl Groups. *Molecules* **2020,** *25* (10).

30.   Tu, C.; Nagao, R.; Louie, A. Y., Multimodal magnetic-resonance/optical-imaging contrast agent sensitive to NADH. *Angew Chem Int Ed Engl* **2009,** *48* (35), 6547-6551.

31. Li, W.-h.; Fraser, S. E.; Meade, T. J., A Calcium-Sensitive Magnetic Resonance Imaging Contrast Agent. *Journal of the American Chemical Society* **1999,** *121* (6), 1413-1414.

32. Yoo, B.; Pagel, M. D., An overview of responsive MRI contrast agents for molecular imaging. *Front Biosci* **2008,** *13*, 1733-52.

33. Louie, A. Y.; Hüber, M. M.; Ahrens, E. T.; Rothbächer, U.; Moats, R.; Jacobs, R. E.; Fraser, S. E.; Meade, T. J., In vivo visualization of gene expression using magnetic resonance imaging. *Nature Biotechnology* **2000,** *18* (3), 321-325.

34. Lilley, L. M.; Kamper, S.; Caldwell, M.; Chia, Z. K.; Ballweg, D.; Vistain, L.; Krimmel, J.; Mills, T. A.; MacRenaris, K.; Lee, P.; Waters, E. A.; Meade, T. J., Self-Immolative Activation of β-Galactosidase-Responsive Probes for In Vivo MR Imaging in Mouse Models. *Angewandte Chemie International Edition* **2020,** *59* (1), 388-394.

35. Laurent, S.; Botteman, F.; Vander Elst, L.; Muller, R. N., Optimising the design of paramagnetic MRI contrast agents: influence of backbone substitution on the water exchange rate of Gd-DTPA derivatives. *Magma* **2004,** *16* (5), 235-45.

36. *Metal Ions in Bio-Imaging Techniques*. De Gruyter: 2021.

37. Vistain, L. F.; Rotz, M. W.; Rathore, R.; Preslar, A. T.; Meade, T. J., Targeted delivery of gold nanoparticle contrast agents for reporting gene detection by magnetic resonance imaging. *Chemical Communications* **2016,** *52* (1), 160-163.

38. Nicholls, F. J.; Rotz, M. W.; Ghuman, H.; MacRenaris, K. W.; Meade, T. J.; Modo, M., DNA-gadolinium-gold nanoparticles for in vivo T1 MR imaging of transplanted human neural stem cells. *Biomaterials* **2016,** *77*, 291-306.

39.   Holbrook, R. J.; Rammohan, N.; Rotz, M. W.; MacRenaris, K. W.; Preslar, A. T.; Meade, T. J., Gd(III)-Dithiolane Gold Nanoparticles for T1-Weighted Magnetic Resonance Imaging of the Pancreas. *Nano Lett* **2016,** *16* (5), 3202-3209.

40.   Rotz, M. W.; Culver, K. S.; Parigi, G.; MacRenaris, K. W.; Luchinat, C.; Odom, T. W.; Meade, T. J., High relaxivity Gd(III)-DNA gold nanostars: investigation of shape effects on proton relaxation. *ACS Nano* **2015,** *9* (3), 3385-96.

41.   Hung, A. H.; Holbrook, R. J.; Rotz, M. W.; Glasscock, C. J.; Mansukhani, N. D.; MacRenaris, K. W.; Manus, L. M.; Duch, M. C.; Dam, K. T.; Hersam, M. C.; Meade, T. J., Graphene oxide enhances cellular delivery of hydrophilic small molecules by co-incubation. *ACS nano* **2014,** *8* (10), 10168-10177.

42.   Manus, L. M.; Mastarone, D. J.; Waters, E. A.; Zhang, X.-Q.; Schultz-Sikma, E. A.; Macrenaris, K. W.;   Ho, D.; Meade, T. J., Gd(III)-nanodiamond conjugates for MRI contrast enhancement. *Nano Lett* **2010,** *10* (2), 484-489.

43.   Chen, D.; Dougherty, C. A.; Zhu, K.; Hong, H., Theranostic applications of carbon nanomaterials in cancer: Focus on imaging and cargo delivery. *J Control Release* **2015,** *210*, 230-45.

44.   Carniato, F.;   Tei, L.; Botta, M., Gd-Based Mesoporous Silica Nanoparticles as MRI Probes. *European Journal of Inorganic Chemistry* **2018,** *2018* (46), 4936-4954.

45.   Ye, F.; Jeong, E.-K.; Jia, Z.; Yang, T.; Parker, D.; Lu, Z.-R., A Peptide Targeted Contrast Agent Specific to Fibrin-Fibronectin Complexes for Cancer Molecular Imaging with MRI. *Bioconjugate Chemistry* **2008,** *19* (12), 2300-2303.

46.   Davies, G.-L.; Kramberger, I.; Davis, J. J., Environmentally responsive MRI contrast agents. *Chemical Communications* **2013,** *49* (84), 9704-9721.

47.   Breckwoldt, M. O.; Chen, J. W.; Stangenberg, L.; Aikawa, E.; Rodriguez, E.; Qiu, S.; Moskowitz, M. A.; Weissleder, R., Tracking the inflammatory response in stroke in vivo by sensing the enzyme myeloperoxidase. *Proc Natl Acad Sci U S A* **2008,** *105* (47), 18584-9.

48.   Nejadnik, H.; Ye, D.; Lenkov, O. D.; Donig, J. S.; Martin, J. E.; Castillo, R.; Derugin, N.; Sennino, B.; Rao, J.; Daldrup-Link, H., Magnetic resonance imaging of stem cell apoptosis in arthritic joints with a caspase activatable contrast agent. *ACS Nano* **2015,** *9* (2), 1150-60.

49.   Li, H.; Parigi, G.; Luchinat, C.; Meade, T. J., Bimodal Fluorescence-Magnetic Resonance Contrast Agent for Apoptosis Imaging. *Journal of the American Chemical Society* **2019,** *141* (15), 6224-6233.

50.   Adams, C. J.; Meade, T. J., Gd(iii)–Pt(iv) theranostic contrast agents for tandem MR imaging and chemotherapy. *Chemical Science* **2020,** *11* (9), 2524-2530.

51.   Lilley, L. M.; Du, K.; Krzyaniak, M. D.; Parigi, G.; Luchinat, C.; Harris, T. D.; Meade, T. J., Effect of Magnetic Coupling on Water Proton Relaxivity in a Series of Transition Metal GdIII Complexes. *Inorganic Chemistry* **2018,** *57* (10), 5810-5819.

52.   Robertson, A. G.; Rendina, L. M., Gadolinium theranostics for the diagnosis and treatment of cancer. *Chemical Society Reviews* **2021,** *50* (7), 4231-4244.

53. Yan, C.; Shi, L.; Guo, Z.; Zhu, W., Molecularly near-infrared fluorescent theranostics for in vivo tracking tumor-specific chemotherapy. *Chinese Chemical Letters* **2019,** *30* (10), 1849-1855.

54. Pruis, I. J.; van Dongen, G. A. M. S.; Veldhuijzen van Zanten, S. E. M., The Added Value of Diagnostic and Theranostic PET Imaging for the Treatment of CNS Tumors. *Int J Mol Sci* **2020,** *21* (3), 1029.

55. Chen, H.; Zhang, W.; Zhu, G.; Xie, J.; Chen, X., Rethinking cancer nanotheranostics. *Nature Reviews Materials* **2017,** *2* (7), 17024.

56. Chen, H.; Jia, H.; Tham, H. P.; Qu, Q.; Xing, P.; Zhao, J.; Phua, S. Z. F.; Chen, G.; Zhao, Y., Theranostic Prodrug Vesicles for Imaging Guided Codelivery of Camptothecin and siRNA in Synergetic Cancer Therapy. *ACS Applied Materials & Interfaces* **2017,** *9* (28), 23536-23543.

Chapter 2 References

1.   Dasari, S.; Bernard Tchounwou, P., Cisplatin in cancer therapy: Molecular mechanisms of action. *European Journal of Pharmacology* **2014,** *740*, 364-378.

2.   Desoize, B.; Madoulet, C., Particular aspects of platinum compounds used at present in cancer treatment. *Critical Reviews in Oncology/Hematology* **2002,** *42* (3), 317-325.

3.   Goodsell, D. S., The Molecular Perspective: Cisplatin. *STEM CELLS* **2006,** *24* (3), 514-515.

4.   Wheate, N. J.; Walker, S.; Craig, G. E.; Oun, R., The status of platinum anticancer drugs in the clinic and in clinical trials. *Dalton Transactions* **2010,** *39* (35), 8113-8127.

5.   Wilson, J. J.; Lippard, S. J., Synthetic Methods for the Preparation of Platinum Anticancer Complexes. *Chemical Reviews* **2014,** *114* (8), 4470-4495.

6.   Farrell, N. P., Multi-platinum anti-cancer agents. Substitution-inert compounds for tumor selectivity and new targets. *Chemical Society Reviews* **2015,** *44* (24), 8773-8785.

7.   Kelland, L., The resurgence of platinum-based cancer chemotherapy. *Nature Reviews Cancer* **2007,** *7*, 573.

8.   Johnstone, T. C.; Park, G. Y.; Lippard, S. J., Understanding and improving platinum anticancer drugs--phenanthriplatin. *Anticancer Res* **2014,** *34* (1), 471-6.

9.   Siddik, Z. H., Cisplatin: mode of cytotoxic action and molecular basis of resistance. *Oncogene* **2003,** *22* (47), 7265-7279.

10.   Galluzzi, L.; Vitale, I.; Michels, J.; Brenner, C.; Szabadkai, G.; Harel-Bellan, A.; Castedo, M.; Kroemer, G., Systems biology of cisplatin resistance: past, present and future. *Cell death & disease* **2014,** *5* (5), e1257-e1257.

11.   Giaccone, G., Clinical Perspectives on Platinum Resistance. *Drugs* **2000,** *59* (4), 9-17.

12.   Köberle, B.; Tomicic, M. T.; Usanova, S.; Kaina, B., Cisplatin resistance: Preclinical findings and clinical implications. *Biochimica et Biophysica Acta (BBA) - Reviews on Cancer* **2010,** *1806* (2), 172-182.

13.   Shen, D.-W.; Pouliot, L. M.; Hall, M. D.; Gottesman, M. M., Cisplatin resistance: a cellular self-defense mechanism resulting from multiple epigenetic and genetic changes. *Pharmacological reviews* **2012,** *64* (3), 706-721.

14.   Kim, J. H.; Lee, K.-W.; Kim, Y. H.; Lee, K. H.; Oh, D. Y.; Kim, J.; Yang, S. H.; Im, S.-A.; Choi, S. H.; Bang, Y.-J., Individualized tumor response testing for prediction of response to Paclitaxel and Cisplatin chemotherapy in patients with advanced gastric cancer. *Journal of Korean medical science* **2010,** *25* (5), 684-690.

15.   Chen, S. H.; Chang, J. Y., New Insights into Mechanisms of Cisplatin Resistance: From Tumor Cell to Microenvironment. *Int J Mol Sci* **2019,** *20* (17).

16.   Zhou, J.; Kang, Y.; Chen, L.; Wang, H.; Liu, J.; Zeng, S.; Yu, L., The Drug-Resistance Mechanisms of Five Platinum-Based Antitumor Agents. *Frontiers in Pharmacology* **2020,** *11* (343).

17.   Gu, Y.-L.; Pan, S.-M.; Ren, J.; Yang, Z.-X.; Jiang, G.-Q., Role of Magnetic Resonance Imaging in Detection of Pathologic Complete Remission in Breast Cancer Patients Treated With Neoadjuvant Chemotherapy: A Meta-analysis. *Clinical Breast Cancer* **2017,** *17* (4), 245-255.

18.   Aboagye, E. O.; Bhujwalla, Z. M.; Shungu, D. C.; Glickson, J. D., Detection of Tumor Response to Chemotherapy by 1H Nuclear Magnetic Resonance Spectroscopy: Effect of

5-Fluorouracil on Lactate Levels in Radiation-induced Fibrosarcoma 1 Tumors. *Cancer Research* **1998,** *58*, 1063-1067.

19.   Zinreich, S. J., Imaging in laryngeal cancer: computed tomography, magnetic resonance imaging, positron emission tomography. *Otolaryngologic Clinics of North America* **2002,** *35* (5), 971-991.

20.   Nguyen-Thu, H.; Hanaoka, H.; Nakajima, T.; Yamaguchi, A.; Nguyen-Cong, T.; Kartamihardja, A. A. P.; Tsushima, Y., Early prediction of triple negative breast cancer response to cisplatin treatment using diffusion-weighted MRI and (18)F-FDG-PET. *Breast Cancer* **2018,** *25* (3), 334-342.

21.   Chang, Y. C.; Yu, C. J.; Chen, C. M.; Hu, F. C.; Hsu, H. H.; Tseng, W. Y.; Ting-Fang Shih, T.; Yang, P. C.; Chih-Hsin Yang, J., Dynamic contrast-enhanced MRI in advanced nonsmall-cell lung cancer patients treated with first-line bevacizumab, gemcitabine, and cisplatin. *J Magn Reson Imaging* **2012,** *36* (2), 387-96.

22.   Kilari, D.; Guancial, E.; Kim, E. S., Role of copper transporters in platinum resistance. *World J Clin Oncol* **2016,** *7* (1), 106-113.

23.   Kelland, L. R., New platinum antitumor complexes. *Crit Rev Oncol Hematol* **1993,** *15* (3), 191-219.

24.   Andrews, P. A.; Howell, S. B., Cellular pharmacology of cisplatin: perspectives on mechanisms of acquired resistance. *Cancer Cells* **1990,** *2* (2), 35-43.

25.   Zhu, Z.; Wang, X.; Li, T.; Aime, S.; Sadler, P. J.; Guo, Z., Platinum(II)–Gadolinium(III) Complexes as Potential Single-Molecular Theranostic Agents for Cancer Treatment. *Angewandte Chemie International Edition* **2014,** *53* (48), 13225-13228.

26. Wu, B.; Li, X.-Q.; Huang, T.; Lu, S.-T.; Wan, B.; Liao, R.-F.; Li, Y.-S.; Baidya, A.; Long, Q.-Y.; Xu, H.-B., MRI-guided tumor chemo-photodynamic therapy with Gd/Pt bifunctionalized porphyrin. *Biomaterials Science* **2017,** *5* (9), 1746-1750.

27. Stacey, O. J.; Amoroso, A. J.; Platts, J. A.; Horton, P. N.; Coles, S. J.; Lloyd, D.; Williams, C. F.; Hayes, A. J.; Dunsford, J. J.; Pope, S. J. A., Water soluble, cyclometalated Pt(ii)–Ln(iii) conjugates towards novel bimodal imaging agents. *Chemical Communications* **2015,** *51* (61), 12305-12308.

28. Adams, C. J.; Meade, T. J., Gd(iii)–Pt(iv) theranostic contrast agents for tandem MR imaging and chemotherapy. *Chemical Science* **2020,** *11* (9), 2524-2530.

29. Thiabaud, G.; Arambula, J. F.; Siddik, Z. H.; Sessler, J. L., Photoinduced Reduction of PtIV within an Anti-Proliferative PtIV–Texaphyrin Conjugate. *Chemistry – A European Journal* **2014,** *20* (29), 8942-8947.

30. Thiabaud, G.; McCall, R.; He, G.; Arambula, J. F.; Siddik, Z. H.; Sessler, J. L., Activation of Platinum(IV) Prodrugs By Motexafin Gadolinium as a Redox Mediator. *Angew Chem Int Ed Engl* **2016,** *55* (41), 12626-12631.

31. Thiabaud, G.; He, G.; Sen, S.; Shelton, K. A.; Baze, W. B.; Segura, L.; Alaniz, J.; Munoz Macias, R.; Lyness, G.; Watts, A. B.; Kim, H. M.; Lee, H.; Cho, M. Y.; Hong, K. S.; Finch, R.; Siddik, Z. H.; Arambula, J. F.; Sessler, J. L., Oxaliplatin Pt(IV) prodrugs conjugated to gadolinium-texaphyrin as potential antitumor agents. *Proc Natl Acad Sci U S A* **2020,** *117* (13), 7021-7029.

32.   Li, H.; Meade, T. J., Molecular Magnetic Resonance Imaging with Gd(III)-Based Contrast Agents: Challenges and Key Advances. *Journal of the American Chemical Society* **2019,** *141* (43), 17025-17041.

33.   Wahsner, J.; Gale, E. M.; Rodríguez-Rodríguez, A.; Caravan, P., Chemistry of MRI Contrast Agents: Current Challenges and New Frontiers. *Chemical Reviews* **2019,** *119* (2), 957-1057.

34.   Song, Y.; Kohlmeir, E. K.; Meade, T. J., Synthesis of Multimeric MR Contrast Agents for Cellular Imaging. *Journal of the American Chemical Society* **2008,** *130* (21), 6662-6663.

35.   Urankar, D.; Košmrlj, J., Preparation of diazenecarboxamide–carboplatin conjugates by click chemistry. *Inorganica Chimica Acta* **2010,** *363* (14), 3817-3822.

36.   Caravan, P.; Farrar, C. T.; Frullano, L.; Uppal, R., Influence of molecular parameters and increasing magnetic field strength on relaxivity of gadolinium- and manganese-based T1 contrast agents. *Contrast Media & Molecular Imaging* **2009,** *4* (2), 89-100.

37.   Hu, J.; Lieb, J. D.; Sancar, A.; Adar, S., Cisplatin DNA damage and repair maps of the human genome at single-nucleotide resolution. *Proceedings of the National Academy of Sciences* **2016,** *113* (41), 11507.

38.   Macquet, J.-P.; Butour, J.-L., Circular Dichroism Study of DNA Platinum Complexes. *European Journal of Biochemistry* **1978,** *83*, 375-387.

39.   Uemura, M.; Yoshikawa, Y.; Chikuma, M.; Komeda, S., A circular dichroism study uncovers a two-step interaction of antitumor azolato-bridged dinuclear platinum(ii) complexes with calf thymus DNA. *Metallomics* **2012,** *4* (7), 641-644.

40. Siddik, Z. H.; Mims, B.; Lozano, G.; Thai, G., Independent pathways of p53 induction by cisplatin and X-rays in a cisplatin-resistant ovarian tumor cell line. *Cancer Res* **1998,** *58* (4), 698-703.

41. Kamalipooya, S.; Abdolmaleki, P.; Salemi, Z.; Javani Jouni, F.; Zafari, J.; Soleimani, H., Simultaneous application of cisplatin and static magnetic field enhances oxidative stress in HeLa cell line. *In Vitro Cellular & Developmental Biology - Animal* **2017,** *53* (9), 783-790.

42. He, Y.; Zhu, Q.; Chen, M.; Huang, Q.; Wang, W.; Li, Q.; Huang, Y.; Di, W., The changing 50% inhibitory concentration (IC50) of cisplatin: a pilot study on the artifacts of the MTT assay and the precise measurement of density-dependent chemoresistance in ovarian cancer. *Oncotarget* **2016,** *7* (43), 70803-70821.

43. James, M. L.; Gambhir, S. S., A Molecular Imaging Primer: Modalities, Imaging Agents, and Applications. *Physiological Reviews* **2012,** *92* (2), 897-965.

44. Pysz, M. A.; Gambhir, S. S.; Willmann, J. K., Molecular imaging: current status and emerging strategies. *Clinical Radiology* **2010,** *65* (7), 500-516.

45. Aston, W. J.; Hope, D. E.; Nowak, A. K.; Robinson, B. W.; Lake, R. A.; Lesterhuis, W. J., A systematic investigation of the maximum tolerated dose of cytotoxic chemotherapy with and without supportive care in mice. *BMC Cancer* **2017,** *17* (1), 684.

Chapter 3 References

1.   Dasari, S.; Bernard Tchounwou, P., Cisplatin in cancer therapy: Molecular mechanisms of action. *European Journal of Pharmacology* **2014,** *740*, 364-378.

2.   Desoize, B.; Madoulet, C., Particular aspects of platinum compounds used at present in cancer treatment. *Critical Reviews in Oncology/Hematology* **2002,** *42* (3), 317-325.

3.   Goodsell, D. S., The Molecular Perspective: Cisplatin. *STEM CELLS* **2006,** *24* (3), 514-515.

4.   Kelland, L., The resurgence of platinum-based cancer chemotherapy. *Nature Reviews Cancer* **2007,** *7*, 573.

5.   Wheate, N. J.; Walker, S.; Craig, G. E.; Oun, R., The status of platinum anticancer drugs in the clinic and in clinical trials. *Dalton Transactions* **2010,** *39* (35), 8113-8127.

6.   Wilson, J. J.; Lippard, S. J., Synthetic Methods for the Preparation of Platinum Anticancer Complexes. *Chemical Reviews* **2014,** *114* (8), 4470-4495.

7.   Farrell, N. P., Multi-platinum anti-cancer agents. Substitution-inert compounds for tumor selectivity and new targets. *Chemical Society Reviews* **2015,** *44* (24), 8773-8785.

8.   Siddik, Z. H., Cisplatin: mode of cytotoxic action and molecular basis of resistance. *Oncogene* **2003,** *22* (47), 7265-7279.

9.   Galluzzi, L.; Vitale, I.; Michels, J.; Brenner, C.; Szabadkai, G.; Harel-Bellan, A.; Castedo, M.; Kroemer, G., Systems biology of cisplatin resistance: past, present and future. *Cell death & disease* **2014,** *5* (5), e1257-e1257.

10.   Giaccone, G., Clinical Perspectives on Platinum Resistance. *Drugs* **2000,** *59* (4), 9-17.

11.   Köberle, B.; Tomicic, M. T.; Usanova, S.; Kaina, B., Cisplatin resistance: Preclinical findings and clinical implications. *Biochimica et Biophysica Acta (BBA) - Reviews on Cancer* **2010,** *1806* (2), 172-182.

12.   Shen, D.-W.; Pouliot, L. M.; Hall, M. D.; Gottesman, M. M., Cisplatin resistance: a cellular self-defense mechanism resulting from multiple epigenetic and genetic changes. *Pharmacological reviews* **2012,** *64* (3), 706-721.

13.   Johnstone, T. C.; Park, G. Y.; Lippard, S. J., Understanding and improving platinum anticancer drugs--phenanthriplatin. *Anticancer Res* **2014,** *34* (1), 471-476.

14.   Browning, R. J.; Reardon, P. J. T.; Parhizkar, M.; Pedley, R. B.; Edirisinghe, M.; Knowles, J. C.; Stride, E., Drug Delivery Strategies for Platinum-Based Chemotherapy. *ACS Nano* **2017,** *11* (9), 8560-8578.

15.   Johnstone, T. C.; Suntharalingam, K.; Lippard, S. J., The Next Generation of Platinum Drugs: Targeted Pt(II) Agents, Nanoparticle Delivery, and Pt(IV) Prodrugs. *Chemical Reviews* **2016,** *116* (5), 3436-3486.

16.   Wang, X.; Guo, Z., Targeting and delivery of platinum-based anticancer drugs. *Chemical Society Reviews* **2013,** *42* (1), 202-224.

17.   Li, X.; Liu, Y.; Tian, H., Current Developments in Pt(IV) Prodrugs Conjugated with Bioactive Ligands. *Bioinorg Chem Appl* **2018,** *2018*, 8276139-8276139.

18.   Kenny, R. G.; Chuah, S. W.; Crawford, A.; Marmion, C. J., Platinum(IV) Prodrugs – A Step Closer to Ehrlich's Vision? *European Journal of Inorganic Chemistry* **2017,** *2017* (12), 1596-1612.

19.   Wang, Z.;   Deng, Z.; Zhu, G., Emerging platinum(iv) prodrugs to combat cisplatin resistance: from isolated cancer cells to tumor microenvironment. *Dalton Transactions* **2019,** *48* (8), 2536-2544.

20.   Montagner, D.;   Tolan, D.;   Andriollo, E.;   Gandin, V.; Marzano, C., A Pt(IV) Prodrug Combining Chlorambucil and Cisplatin: a Dual-Acting Weapon for Targeting DNA in Cancer Cells. *Int J Mol Sci* **2018,** *19* (12), 3775.

21.   Chen, H.;   Wang, X.; Gou, S., A cisplatin-based platinum(IV) prodrug containing a glutathione s-transferase inhibitor to reverse cisplatin resistance in non-small cell lung cancer. *Journal of Inorganic Biochemistry* **2019,** *193*, 133-142.

22.   Hui Huang, Y. D., Yanhua Zhang, Dan Ru, Zhihua Wu, Jiali Zhang, Ming SHen, Yourong DUan, Ying Sun, GSH-sensitive Pt(IV) prodrug-loaded phase-transitional nanoparticles with a hybrid lipid-polymer shell for precise theranostics against ovarian cancer. *Theranostics* **2019,** *9* (4), 1047-1065.

23.   Qin, X.;   Fang, L.;   Zhao, J.; Gou, S., Theranostic Pt(IV) Conjugate with Target Selectivity for Androgen Receptor. *Inorganic Chemistry* **2018,** *57* (9), 5019-5029.

24.   Ong, J. X.;   Lim, C. S. Q.;   Le, H. V.; Ang, W. H., A Ratiometric Fluorescent Probe for Cisplatin: Investigating the Intracellular Reduction of Platinum(IV) Prodrug Complexes. *Angewandte Chemie International Edition* **2019,** *58* (1), 164-167.

25.   Song, Y.;   Suntharalingam, K.;   Yeung, J. S.;   Royzen, M.; Lippard, S. J., Synthesis and characterization of Pt(IV) fluorescein conjugates to investigate Pt(IV) intracellular transformations. *Bioconjug Chem* **2013,** *24* (10), 1733-1740.

26.   Wilson, J. J.; Lippard, S. J., Modulation of Ligand Fluorescence by the Pt(II)/Pt(IV) Redox Couple. *Inorganica Chim Acta* **2012,** *389*, 77-84.

27.   Yuan, Y.; Chen, Y.; Tang, B. Z.; Liu, B., A targeted theranostic platinum(iv) prodrug containing a luminogen with aggregation-induced emission (AIE) characteristics for in situ monitoring of drug activation. *Chemical Communications* **2014,** *50* (29), 3868-3870.

28.   Zhao, Y.; Woods, J. A.; Farrer, N. J.; Robinson, K. S.; Pracharova, J.; Kasparkova, J.; Novakova, O.; Li, H.; Salassa, L.; Pizarro, A. M.; Clarkson, G. J.; Song, L.; Brabec, V.; Sadler, P. J., Diazido Mixed-Amine Platinum(IV) Anticancer Complexes Activatable by Visible-Light Form Novel DNA Adducts. *Chemistry – A European Journal* **2013,** *19* (29), 9578-9591.

29.   Kasparkova, J.; Kostrhunova, H.; Novakova, O.; Křikavová, R.; Vančo, J.; Trávníček, Z.; Brabec, V., A Photoactivatable Platinum(IV) Complex Targeting Genomic DNA and Histone Deacetylases. *Angewandte Chemie International Edition* **2015,** *54* (48), 14478-14482.

30.   Thiabaud, G.; Arambula, J. F.; Siddik, Z. H.; Sessler, J. L., Photoinduced Reduction of PtIV within an Anti-Proliferative PtIV–Texaphyrin Conjugate. *Chemistry – A European Journal* **2014,** *20* (29), 8942-8947.

31.   Thiabaud, G.; McCall, R.; He, G.; Arambula, J. F.; Siddik, Z. H.; Sessler, J. L., Activation of Platinum(IV) Prodrugs By Motexafin Gadolinium as a Redox Mediator. *Angew Chem Int Ed Engl* **2016,** *55* (41), 12626-12631.

32.   James, M. L.; Gambhir, S. S., A Molecular Imaging Primer: Modalities, Imaging Agents, and Applications. *Physiological Reviews* **2012,** *92* (2), 897-965.

33. Pysz, M. A.; Gambhir, S. S.; Willmann, J. K., Molecular imaging: current status and emerging strategies. *Clinical Radiology* **2010,** *65* (7), 500-516.

34. Wahsner, J.; Gale, E. M.; Rodríguez-Rodríguez, A.; Caravan, P., Chemistry of MRI Contrast Agents: Current Challenges and New Frontiers. *Chemical Reviews* **2019,** *119* (2), 957-1057.

35. Rammohan, N.; MacRenaris, K. W.; Moore, L. K.; Parigi, G.; Mastarone, D. J.; Manus, L. M.; Lilley, L. M.; Preslar, A. T.; Waters, E. A.; Filicko, A.; Luchinat, C.; Ho, D.; Meade, T. J., Nanodiamond-Gadolinium(III) Aggregates for Tracking Cancer Growth In Vivo at High Field. *Nano Lett* **2016,** *16* (12), 7551-7564.

36. Holbrook, R. J.; Rammohan, N.; Rotz, M. W.; MacRenaris, K. W.; Preslar, A. T.; Meade, T. J., Gd(III)-Dithiolane Gold Nanoparticles for T1-Weighted Magnetic Resonance Imaging of the Pancreas. *Nano Lett* **2016,** *16* (5), 3202-9.

37. Zhu, Z.; Wang, X.; Li, T.; Aime, S.; Sadler, P. J.; Guo, Z., Platinum(II)–Gadolinium(III) Complexes as Potential Single-Molecular Theranostic Agents for Cancer Treatment. *Angewandte Chemie International Edition* **2014,** *53* (48), 13225-13228.

38. Wu, B.; Li, X.-Q.; Huang, T.; Lu, S.-T.; Wan, B.; Liao, R.-F.; Li, Y.-S.; Baidya, A.; Long, Q.-Y.; Xu, H.-B., MRI-guided tumor chemo-photodynamic therapy with Gd/Pt bifunctionalized porphyrin. *Biomaterials Science* **2017,** *5* (9), 1746-1750.

39. Stacey, O. J.; Amoroso, A. J.; Platts, J. A.; Horton, P. N.; Coles, S. J.; Lloyd, D.; Williams, C. F.; Hayes, A. J.; Dunsford, J. J.; Pope, S. J. A., Water soluble, cyclometalated Pt(ii)–Ln(iii) conjugates towards novel bimodal imaging agents. *Chemical Communications* **2015,** *51* (61), 12305-12308.

40.   Li, H.; Meade, T. J., Molecular Magnetic Resonance Imaging with Gd(III)-Based Contrast Agents: Challenges and Key Advances. *Journal of the American Chemical Society* **2019,** *141* (43), 17025-17041.

41.   Rammohan, N.; MacRenaris, K. W.; Moore, L. K.; Parigi, G.; Mastarone, D. J.; Manus, L. M.; Lilley, L. M.; Preslar, A. T.; Waters, E. A.; Filicko, A.; Luchinat, C.; Ho, D.; Meade, T. J., Nanodiamond–Gadolinium(III) Aggregates for Tracking Cancer Growth In Vivo at High Field. *Nano Letters* **2016,** *16* (12), 7551-7564.

42.   Varbanov, H. P.; Valiahdi, S. M.; Kowol, C. R.; Jakupec, M. A.; Galanski, M.; Keppler, B. K., Novel tetracarboxylatoplatinum(iv) complexes as carboplatin prodrugs. *Dalton Transactions* **2012,** *41* (47), 14404-14415.

43.   Hall, M. D.; Dillon, C. T.; Zhang, M.; Beale, P.; Cai, Z.; Lai, B.; Stampfl, A. P. J.; Hambley, T. W., The cellular distribution and oxidation state of platinum(II) and platinum(IV) antitumour complexes in cancer cells. *JBIC Journal of Biological Inorganic Chemistry* **2003,** *8* (7), 726-732.

44.   Coen, K.; Flannagan, R. S.; Baron, S.; Carraro-Lacroix, L. R.; Wang, D.; Vermeire, W.; Michiels, C.; Munck, S.; Baert, V.; Sugita, S.; Wuytack, F.; Hiesinger, P. R.; Grinstein, S.; Annaert, W., Lysosomal calcium homeostasis defects, not proton pump defects, cause endo-lysosomal dysfunction in PSEN-deficient cells. *The Journal of Cell Biology* **2012,** *198* (1), 23-35.

45.   Forman, H. J.; Zhang, H.; Rinna, A., Glutathione: overview of its protective roles, measurement, and biosynthesis. *Mol Aspects Med* **2009,** *30* (1-2), 1-12.

46. Tolan, D.; Gandin, V.; Morrison, L.; El-Nahas, A.; Marzano, C.; Montagner, D.; Erxleben, A., Oxidative Stress Induced by Pt(IV) Pro-drugs Based on the Cisplatin Scaffold and Indole Carboxylic Acids in Axial Position. *Scientific Reports* **2016,** *6*, 29367.

Chapter 4 References

1. Bading, H. (2013) Nuclear calcium signalling in the regulation of brain function, *Nat. Rev. Neurosci. 14*, 593.

2. Bean, B. P. (2007) The action potential in mammalian central neurons, *Nat. Rev. Neurosci. 8*, 451.

3. Berridge, M. J. (1998) Neuronal Calcium Signaling, *Neuron 21*, 13-26.

4. Clapham, D. E. (2007) Calcium Signaling, *Cell 131*, 1047-1058.

5. Hagenston, A. M., and Bading, H. Calcium signaling in synapse-to-nucleus communication, *Cold Spring Harbor Perspect. Biol. 3*, a004564-a004564.

6. Mauceri, D., Hagenston, A. M., Schramm, K., Weiss, U., and Bading, H. (2015) Nuclear Calcium Buffering Capacity Shapes Neuronal Architecture, *J. Biol. Chem. 290*, 23039-23049.

7. Nanou, E., and Catterall, W. A. (2018) Calcium Channels, Synaptic Plasticity, and Neuropsychiatric Disease, *Neuron 98*, 466-481.

8. Kovac, S., Dinkova Kostova, A. T., Herrmann, A. M., Melzer, N., Meuth, S. G., and Gorji, A. (2017) Metabolic and Homeostatic Changes in Seizures and Acquired Epilepsy-Mitochondria, Calcium Dynamics and Reactive Oxygen Species, *Int. J. Mol. Sci. 18*, 1935.

9. Kumar, A., Bodhinathan, K., and Foster, T. C. (2009) Susceptibility to Calcium Dysregulation during Brain Aging, *Front. Aging. Neurosci. 1*, 2-2.

10. Massimini, M., and Amzica, F. (2001) Extracellular Calcium Fluctuations and Intracellular Potentials in the Cortex During the Slow Sleep Oscillation, *J. Neurophysiol. 85*, 1346-1350.

11. Nessa, A., Rahman, S. A., and Hussain, K. (2016) Hyperinsulinemic Hypoglycemia - The Molecular Mechanisms, *Front. Endocrinol. 7*, 29-29.

12. Silver, I. A., and Erecińska, M. (1990) Intracellular and extracellular changes of [Ca2+] in hypoxia and ischemia in rat brain in vivo, *J. Gen. Physiol. 95*, 837.

13. Waters, J., Larkum, M., Sakmann, B., and Helmchen, F. (2003) Supralinear Ca2+ Influx into Dendritic Tufts of Layer 2/3 Neocortical Pyramidal Neurons In Vitro and In Vivo, *J. Neurosci 23*, 8558.

14. Zündorf, G., and Reiser, G. (2011) Calcium dysregulation and homeostasis of neural calcium in the molecular mechanisms of neurodegenerative diseases provide multiple targets for neuroprotection, *Antioxid. Redox Signaling 14*, 1275-1288.

15. Bartelle, B. B., Barandov, A., and Jasanoff, A. (2016) Molecular fMRI, *J. Neurosci. 36*, 4139.

16. Egawa, T., Hanaoka, K., Koide, Y., Ujita, S., Takahashi, N., Ikegaya, Y., Matsuki, N., Terai, T., Ueno, T., Komatsu, T., and Nagano, T. (2011) Development of a Far-Red to Near-Infrared Fluorescence Probe for Calcium Ion and its Application to Multicolor Neuronal Imaging, *J. Am. Chem. Soc. 133*, 14157-14159.

17. Grienberger, C., and Konnerth, A. (2012) Imaging Calcium in Neurons, *Neuron 73*, 862-885.

18. Heeger, D. J., and Ress, D. (2002) What does fMRI tell us about neuronal activity?, *Nat. Rev. Neurosci. 3*, 142-151.

19. Logothetis, N. K. (2008) What we can do and what we cannot do with fMRI, *Nature 453*, 869.

20.   Logothetis, N. K., Pauls, J., Augath, M., Trinath, T., and Oeltermann, A. (2001) Neurophysiological investigation of the basis of the fMRI signal, *Nature 412*, 150-157.

21.   Okada, S., Bartelle, B. B., Li, N., Breton-Provencher, V., Lee, J. J., Rodriguez, E., Melican, J., Sur, M., and Jasanoff, A. (2018) Calcium-dependent molecular fMRI using a magnetic nanosensor, *Nat. Nanotechnol. 13*, 473-477.

22.   Ouzounov, D. G., Wang, T., Wang, M., Feng, D. D., Horton, N. G., Cruz-Hernández, J. C., Cheng, Y.-T., Reimer, J., Tolias, A. S., Nishimura, N., and Xu, C. (2017) In vivo three-photon imaging of activity of GCaMP6-labeled neurons deep in intact mouse brain, *Nat. Methods 14*, 388.

23.   Thestrup, T., Litzlbauer, J., Bartholomäus, I., Mues, M., Russo, L., Dana, H., Kovalchuk, Y., Liang, Y., Kalamakis, G., Laukat, Y., Becker, S., Witte, G., Geiger, A., Allen, T., Rome, L. C., Chen, T.-W., Kim, D. S., Garaschuk, O., Griesinger, C., and Griesbeck, O. (2014) Optimized ratiometric calcium sensors for functional in vivo imaging of neurons and T lymphocytes, *Nat. Methods 11*, 175.

24.   Pérez Koldenkova, V., and Nagai, T. (2013) Genetically encoded Ca2+ indicators: Properties and evaluation, *Biochimica et Biophysica Acta 1833*, 1787-1797.

25.   Lin, M. Z., and Schnitzer, M. J. (2016) Genetically encoded indicators of neuronal activity, *Nat. Neurosci 19*, 1142-1153.

26.   Lin Tian, S. A. H., Loren L. Looger. (2012) Imaging Neuronal Activity with Genetically Encoded Calcium Indicators, *Cold Spring Harb. Protocols*, 647-656.

27.   James, M. L., and Gambhir, S. S. (2012) A Molecular Imaging Primer: Modalities, Imaging Agents, and Applications, *Physiol. Rev. 92*, 897-965.

28. Pysz, M. A., Gambhir, S. S., and Willmann, J. K. (2010) Molecular imaging: current status and emerging strategies, *Clin. Radiol. 65*, 500-516.

29. Logothetis, N. K., and Wandell, B. A. (2004) Interpreting the BOLD Signal, *Annu. Rev. Physiol. 66*, 735-769.

30. Heffern, M. C., Matosziuk, L. M., and Meade, T. J. (2014) Lanthanide Probes for Bioresponsive Imaging, *Chem. Rev. 114*, 4496-4539.

31. Li, W.-h., Fraser, S. E., and Meade, T. J. (1999) A Calcium-Sensitive Magnetic Resonance Imaging Contrast Agent, *J. Am. Chem. Soc. 121*, 1413-1414.

32. Li, W.-h., Parigi, G., Fragai, M., Luchinat, C., and Meade, T. J. (2002) Mechanistic Studies of a Calcium-Dependent MRI Contrast Agent, *Inorg. Chem. 41*, 4018-4024.

33. MacRenaris, K. W., Ma, Z., Krueger, R. L., Carney, C. E., and Meade, T. J. (2016) Cell-Permeable Esterase-Activated Ca(II)-Sensitive MRI Contrast Agent, *Bioconjugate Chem. 27*, 465-473.

34. Angelovski, G., Fouskova, P., Mamedov, I., Canals, S., Toth, E., and Logothetis, N. K. (2008) Smart Magnetic Resonance Imaging Agents that Sense Extracellular Calcium Fluctuations, *ChemBioChem 9*, 1729-1734.

35. Angelovski, G., Gottschalk, S., Milošević, M., Engelmann, J., Hagberg, G. E., Kadjane, P., Andjus, P., and Logothetis, N. K. (2014) Investigation of a Calcium-Responsive Contrast Agent in Cellular Model Systems: Feasibility for Use as a Smart Molecular Probe in Functional MRI, *ACS Chem. Neurosci. 5*, 360-369.

36. Atanasijevic, T., Shusteff, M., Fam, P., and Jasanoff, A. (2006) Calcium-sensitive MRI contrast agents based on superparamagnetic iron oxide nanoparticles and calmodulin, *Proc. Natl. Acad. Sci. 103*, 14707.

37. Barandov, A., Bartelle, B. B., Williamson, C. G., Loucks, E. S., Lippard, S. J., and Jasanoff, A. (2019) Sensing intracellular calcium ions using a manganese-based MRI contrast agent, *Nat. Commun. 10*, 897.

38. Hagberg, G. E., Mamedov, I., Power, A., Beyerlein, M., Merkle, H., Kiselev, V. G., Dhingra, K., Kubìček, V., Angelovski, G., and Logothetis, N. K. (2014) Diffusion properties of conventional and calcium-sensitive MRI contrast agents in the rat cerebral cortex, *Contrast Media Mol. Imaging 9*, 71-82.

39. Savic, T., Gambino, G., Bokharaie, V., Noori, H., Logothetis, N., and Angelovski, G. (2019) Early detection and monitoring of cerbral ischemia using calcium-responsive MRI probes, *Proc. Natl. Acad. Sci. 116*, 20666-20671.

40. Harrison, V. S. R., Carney, C. E., MacRenaris, K. W., Waters, E. A., and Meade, T. J. (2015) Multimeric Near IR–MR Contrast Agent for Multimodal In Vivo Imaging, *J. Am. Chem. Soc. 137*, 9108-9116.

41. Wu, J. B., Shi, C., Chu, G. C.-Y., Xu, Q., Zhang, Y., Li, Q., Yu, J. S., Zhau, H. E., and Chung, L. W. K. (2015) Near-infrared fluorescence heptamethine carbocyanine dyes mediate imaging and targeted drug delivery for human brain tumor, *Biomaterials 67*, 1-10.

42. Yi, X., Wang, F., Qin, W., Yang, X., and Yuan, J. (2014) Near-infrared fluorescent probes in cancer imaging and therapy: an emerging field, *Int. J. Nanomed. 9*, 1347-1365.

43. Grynkiewicz, G., Poenie, M., and Tsien, R. Y. (1985) A New Generation of Ca2+ Indicators with Greatly Improved Fluorescence Properties, *J. Biol. Chem. 260*, 3440-3450.

44. Shi, C., Wu, J. B., and Pan, D. (2016) Review on near-infrared heptamethine cyanine dyes as theranostic agents for tumor imaging, targeting, and photodynamic therapy, *J. Biomed. Opt. 21*, 1-11, 11.

45. Brimson, J. M., and Tencomnao, T. (2011) Rhinacanthus nasutus Protects Cultured Neuronal Cells against Hypoxia Induced Cell Death, *Molecules 16*.

46. Calabrese, E. J. (2008) Pharmacological Enhancement of Neuronal Survival, *Crit. Rev. Toxicol. 38*, 349-389.

47. Wahsner, J., Gale, E. M., Rodríguez-Rodríguez, A., and Caravan, P. (2019) Chemistry of MRI Contrast Agents: Current Challenges and New Frontiers, *Chem. Rev. 119*, 957-1057.

APPENDIX 1

SUPPORTING INFORMATION FOR CHAPTER 2

General Methods. Unless otherwise indicated, all reactions were performed under a nitrogen atmosphere using oven-dried glassware. Anhydrous solvents were used in all reactions and obtained from a J.C. Meyer solvent system (Laguna Beach, CA). Thin-layer chromatography (TLC) was performed on EMD 60 F254 silica gel plates. Standard grade 60 Å 230–400 mesh silica gel was used for normal-phase column chromatography. Unless otherwise stated, all silica gel columns were flashed with air. ^{1}H and ^{13}C NMR spectra were obtained on a Bruker 500 MHz Avance III NMR spectrometer. ESI-MS was performed on a Bruker AmaZon-SL spectrometer.

Cyclen was obtained from Strem Chemical, while all other reagents were purchased from Sigma Aldrich, Fisher Scientific, or TCI and used without purification. Analytical HPLC-MS was performed on an Agilent 1260 Infinity II HPLC system with an in-line Agilent 6120 Quad mass spectrometer. Semi-preparative HPLC was performed on an Agilent PrepStar 218 equipped with an Agilent 1260 Infinity diode array detector. HPLC purifications utilized deionized water (18.2 MΩ·cm) obtained from a Millipore Q-Guard System and HPLC grade MeCN, formic acid, and ammonium hydroxide (all obtained from Fisher Scientific).

Analytical HPLC-MS used a Phenomenex Synergi C18 column (4.6 × 150 mm, 4 μm). Semipreparative HPLC used a Phenomenex Synergi C18 column (21.2 x 150 mm, 4 μm). **GP1** and **GP2** were purified using the following method: MeCN held at 0% for 5 min followed by a 15 min ramp to 25% followed by a 5 min ramp to 100%.

Synthesis of GP1. 82 mg **1** (0.14 mmol) and 59 mg **2** (0.16 mmol) were added to a 25 mL round bottom flask and dissolved in 10 mL of dry DMF. 11 mg CuSO$_4$(H$_2$O)$_5$ (0.045 mmol) and 18 mg

(+)-sodium L-ascorbate (0.09 mmol) were added to 200 μL 0.9% NaCl solution and mixed thoroughly. The mixture was added to the round bottom flask containing **1** and **2**, and the solution was stirred under nitrogen in the dark for 48 h. The DMF was evaporated and the crude product was dissolved in 15 mL of 0.9% NaCl solution to ensure the chloride ligands were not lost. The crude was purified by HPLC (retention time: 13.4 min) in 32% yield. An analytical HPLC-MS trace of the purified product is found in Figure S1A. HRMS m/z observed: 999.1005 $[M+Na]^+$ (Figure S1B).

Synthesis of GP2. 50 mg **1** (0.08 mmol) and 40 mg **3** (0.09 mmol) were added to a 25 mL round bottom flask and dissolved in 10 mL of dry DMF. 6 mg $CuSO_4(H_2O)_5$ (0.025 mmol) and 10 mg (+)-sodium L-ascorbate (0.05 mmol) were added to 200 μL H_2O and mixed thoroughly. The mixture was added to the round bottom flask containing **1** and **3**, and the solution was stirred under nitrogen in the dark for 48 h. The DMF was evaporated, the crude product was dissolved in 15 mL of H_2O, and the crude was purified by HPLC (retention time: 14.5 min) in 68% yield. An analytical HPLC-MS trace of the purified product is found in Figure S1C. HRMS m/z observed: 1049.2075 $[M+H]^+$ (Figure S1D).

Relaxivity Measurements at 1.41 T. **GP1** and **GP2** were dissolved in 1 mL of 5 mM pH 7.40 Tris HCl buffer (with or without 500 μM CT-DNA). Each solution was serially diluted to make solutions of varying concentration. Solutions containing CT-DNA were incubated for 24 h at 37 °C to allow adequate time for the agents to bind DNA. Relaxation times were measured on a Bruker

mq60 NMR analyzer equipped with Minispec v 2.51 Rev.00/NT software (Bruker Biospin, Billerica, MA, USA) operating at 1.41 T (60MHz) and 37 °C. Measurements were made using an inversion recovery pulse sequence (T_1_ir_mb) using the following parameters: 4 scans per point, 10 data points, monoexponential curve fitting, phase cycling, 10 ms first pulse separation, and a recycle delay and final pulse separation ≥ 5 T_1. 10 µL aliquots of each solution were taken for ICP-MS analysis to determine the concentration of Gd(III). Measurements were repeated every day for a week to ensure no changes in relaxivity were observed.

Relaxivity Measurements at 7 T. GP1 and **GP2** were dissolved in 200 µL 5 mM pH 7.40 Tris HCl buffer (with or without 500 µM CT-DNA) and each solution was serially diluted to make solutions of varying concentration. 25 µL of each solution were pipetted into flame sealed Pasteur pipettes. The pipette tips containing solution were scored, separated, and sealed with parafilm to make small capillaries containing solution. These capillaries were imaged using a Bruker PharmaScan 7 T MR imaging spectrometer (Bruker BioSpin, Billerica, MA, USA). T_1 relaxation times were measured using a rapid-acquisition rapid-echo (RARE-VTR) T_1-map pulse sequence with static T_E (10 ms) and variable T_R (100, 200, 400, 500, 750, 1000, 2500, 7500, and 1000 ms) values. Imaging parameters were as follows: field of view (FOV) = 25 x 25 mm^2, matrix size (MTX) = 256 x 256, number of axial slices = 5, slice thickness (SI) = 1.0 mm, and averages (NEX) = 4. T_1 analysis was carried out using the image sequence analysis tool in Paravision 6.0 pl2 software (Bruker, Billerica, MA, USA) with monoexponential curve-fitting of image intensities of selected regions of interest (ROIs) for each axial slice.

Circular Dichroism with CT-DNA. A stock solution of 100 μM CT-DNA in 5 mM pH 7.40 Tris HCl buffer was prepared. CT-DNA solutions with varying equivalents of **GP1**, **GP2**, cisplatin or carboplatin were prepared and incubated at 37 °C in the dark for 24 h. CD spectra of each solution were acquired using the following parameters: 220-320 nm, 1 nm bandwidth, 0.1 nm step resolution, 10 nm/min scan speed, 1 s response time.

Cell Lines and Culture. 2780CP/Cl-16 cells were obtained from Professor Zahid Siddik at MD Anderson Cancer Center. A2780 and 2780CP/Cl-16 cells were cultured using RPMI-1640 supplemented with 10% FBS and L-glutamine. HeLa cells were cultured using phenol red free DMEM supplemented with 10% FBS. All three cell lines were grown in a humidified incubator at 37 °C and 5% CO_2 and were harvested using 0.25% TrypLE. Cells were grown for 24 hours after plating before each experiment. All solutions were filtered through 0.2 μL sterile filters before use.

Viability Assays. A2780, 2780CP/Cl-16, and HeLa cells were plated at a density of 3,000 cells per well (100 μL) in opaque white 96-well plates. Cells were dosed with 100 μL of solutions of **GP1**, **GP2**, cisplatin, or carboplatin in media and incubated for 48 hours (**GP1** or cisplatin) or 72 hours (**GP2** or carboplatin). After incubation, 50 μL CellTiter-Glo 2.0 (Promega, Madison, WI) was added to each well and the assay was carried out following the manufacturer's protocol. Luminescence of the wells was measured using a Synergy H1 microplate reader (BioTek,

Winooski, VT). Viability was determined by comparing luminescence readings of the cells treated with agent to untreated control cells. Values are reported as the average ± the standard deviation of three independent experiments.

Concentration-dependent Cell Uptake. A2780, 2780CP/Cl-16, and HeLa cells were plated at a density of 40,000 cells per well (500 μL) in a 24-well plate. Cells were incubated with **GP1**, **GP2**, cisplatin or carboplatin at varying concentrations in media (300 μL) for 24 hours. After 24 hours, the media were aspirated and the cells were washed twice with 500 μL of PBS, harvested, and centrifuged at 500 rpm for 5 minutes at 4° C. The media were aspirated, and the cells were resuspended in 200 μL of media. A 50 μL aliquot was taken for cell counting using a Guava PCA system using the Guava Viacount protocol provided by the manufacturer. An additional 100 μL aliquot was used for ICP-MS analysis of Gd and Pt in the cells. Values are reported as the average ± the standard deviation of three independent experiments.

Time-dependent Cellular Uptake. HeLa cells were plated at a density of 40,000 cells per well (500 μL) in a 24-well plate. Cells were incubated with 300 μL of 250 μM **GP1** or 1000 μM **GP2** in media for variable amounts of time (3, 6, 9, 24 h). At each timepoint, the media were aspirated, and the cells were washed twice with 500 μL of PBS, harvested, and centrifuged at 500 rpm for 5 minutes at 4° C. The media were aspirated, and the cells were resuspended in 200 μL of media. A 50 μL aliquot was taken for cell counting using a Guava PCA system using the Guava Viacount

protocol provided by the manufacturer. An additional 100 μL aliquot was used for ICP-MS analysis of Gd and Pt in the cells. Values are reported as the average ± the standard deviation of three independent experiments.

MR Imaging of Cell Pellets at 7 T. A2780 and 2780CP/Cl-16 cells were grown to ~60% confluency in T-75 flasks. A2780 and 2780CP/Cl-16 cells were both dosed with 5 mL of 125 μM **GP1**, 500 μM **GP2**, or vehicle (media). Cells were incubated for 24 hours. After incubation, the media were aspirated and the cells were washed twice with 5 mL PBS, harvested, and centrifuged at 500 rpm for 5 min at 4 °C. The cells were resuspended in 1 mL of media and 950 μL of the suspension was added to flame-sealed Pasteur pipettes while the rest was used for cell counting and ICP-MS. The pipettes were centrifuged at 200 rpm for 5 minutes and were separated to form small capillaries containing the cell pellets. The capillaries were sealed with parafilm and imaged using a Bruker PharmaScan 7 T MR imaging spectrometer following the same imaging protocol previously described.

In vivo **MR imaging of tumor-bearing mice at 9.4 T.** All animal experiments were reviewed and approved by the Institutional Animal Care and Use Committee (IACUC) at Northwestern University (protocol # IS00000691). Athymic nude mice (Jackson Laboratory) were inoculated on the left flank through subcutaneous injection of A2780 cells (3 million/mouse) or 2780CP/Cl-16 cells (8 millions/mouse) in 1:1 PBS/Matrigel. The tumors were measured twice weekly until they were of adequate size for imaging, around 2 weeks for A2780 and 4 weeks for 2780CP/Cl-16 cells.

Three A2780 and three 2780CP/Cl-16 mice were imaged pre-injection and 15 minutes and 3 hours after IV injection of 0.15 mmol/kg **GP1**. After the 3-hour time point, mice the mice were euthanized, and the tumors were collected for ICP-MS analysis of Gd(III) and Pt(II) content.

MR imaging was performed on a 9.4T Bruker Biospec MRI system with a 30 cm bore and a 12 cm gradient insert (Bruker Biospin Inc, Billerica, MA). Respiratory signals and temperature were monitored using an MR-compatible physiologic monitoring system (SA Instruments, Stonybrook, NY); a warm water circulating system was used to maintain body temperature. The mouse's abdomen was centered in a 40 mm quadrature volume coil (Bruker Biospin, Inc, Billerica, MA) operating in transmit/receive mode. A reference standard containing a diluted commercially available Gd contrast agent (Multihance) was placed alongside the mouse. T_1 weighted images were acquired using an accelerated spin echo sequence (T_1 Rapid Acquisition with Relaxation Enhancement, T1-RARE) oriented axially. The following parameters were used: TR/TE = 750 ms / 5.62 ms, RARE factor 4, MTX = 256 x 256, FOV 3.5 x 3.5 cm, 7 slices, 1 mm slice thickness and 4 signal averages. Acquisition time was approximately 4 minutes. *In vivo* MRI data were analyzed using Amira version 2020.1 (Thermo Fisher Scientific, Waltham, MA, USA). T_1 weighted images were normalized to the reference standard, a color map was applied, and then the T_1 weighted image was overlaid on the corresponding T_2 weighted anatomical reference image.

Cell Counting with a Guava EasyCyte Mini Personal Cell Analyzer (PCA) System. Aliquots of cell suspensions were mixed with the Guava ViaCount Reagent and allowed to stain for 5 minutes. The samples were vortexed for 20 seconds and cell count was determined via manual

analysis using a Guava EasyCyte Mini PCA and ViaCount software. 1000 events were acquired for each sample and dilutions were performed to assure the cell count was in the optimal range for instrument performance (10-100 cells/µL). Performance of the instrument was assessed daily using Guava-Check Beads and the manufacturer's protocol and Daily Check software.

Quantification of Gadolinium and Platinum with Inductively Coupled Plasma Mass Spectrometry. Quantification of Gd and Pt was accomplished using ICP-MS of acid digested samples. Specifically, samples were digested in concentrated trace nitric acid (> 69%, Thermo Fisher Scientific, Waltham, MA, USA) and trace hydrochloric acid (> 34%, Thermo Fisher Scientific, Waltham, MA, USA) and placed at 65 °C for at least 4 hours to allow for complete sample digestion. Ultra-pure H_2O (18.2 MΩ·cm) was then added to produce a final solution of 2.0% nitric acid and 2.0% hydrochloric acid (v/v) in a total sample volume of 10 mL. Quantitative standards were made using a 10,000 µg/mL Gd elemental standard and a 1,000 ug/mL Pt elemental standard (Inorganic Ventures, Christiansburg, VA, USA) which were used to create a 200 ng/g mixed element standard and a 2 ng/g mixed element standard in 2.0% nitric acid and 2.0% hydrochloric acid (v/v) in a total sample volume of 50 mL. A solution of 2.0% nitric acid and 2.0% hydrochloric acid (v/v) was used as the calibration blank.

ICP-MS was performed on a computer-controlled (QTEGRA software) Thermo iCapQ ICP-MS (Thermo Fisher Scientific, Waltham, MA, USA) operating in STD mode and equipped with a ESI SC-2DX PrepFAST autosampler (Omaha, NE, USA). Internal standard was added inline using the prepFAST system and consisted of 1 ng/mL of a mixed element solution containing Bi, In, ^{6}Li,

Sc, Tb, Y (IV-ICPMS-71D from Inorganic Ventures). Online dilution was also carried out by the prepFAST system and used to generate a calibration curve consisting of 200, 100, 50, 20, 10, 2 ppb Gd and Pt and a calibration curve consisting of 2000, 1000, 500, 200, 100, and 20 ppt Gd and Pt. Each sample was acquired using 1 survey run (10 sweeps) and 3 main (peak jumping) runs (40 sweeps). The isotopes selected for analysis were ^{194,195}Pt, ^{56,57}Gd, and ^{115}In, ^{159}Tb, ^{209}Bi (chosen as internal standards for data interpolation and machine stability). Instrument performance is optimized daily through autotuning followed by verification via a performance report (passing manufacturer specifications).

HPLC-MS and HRMS:
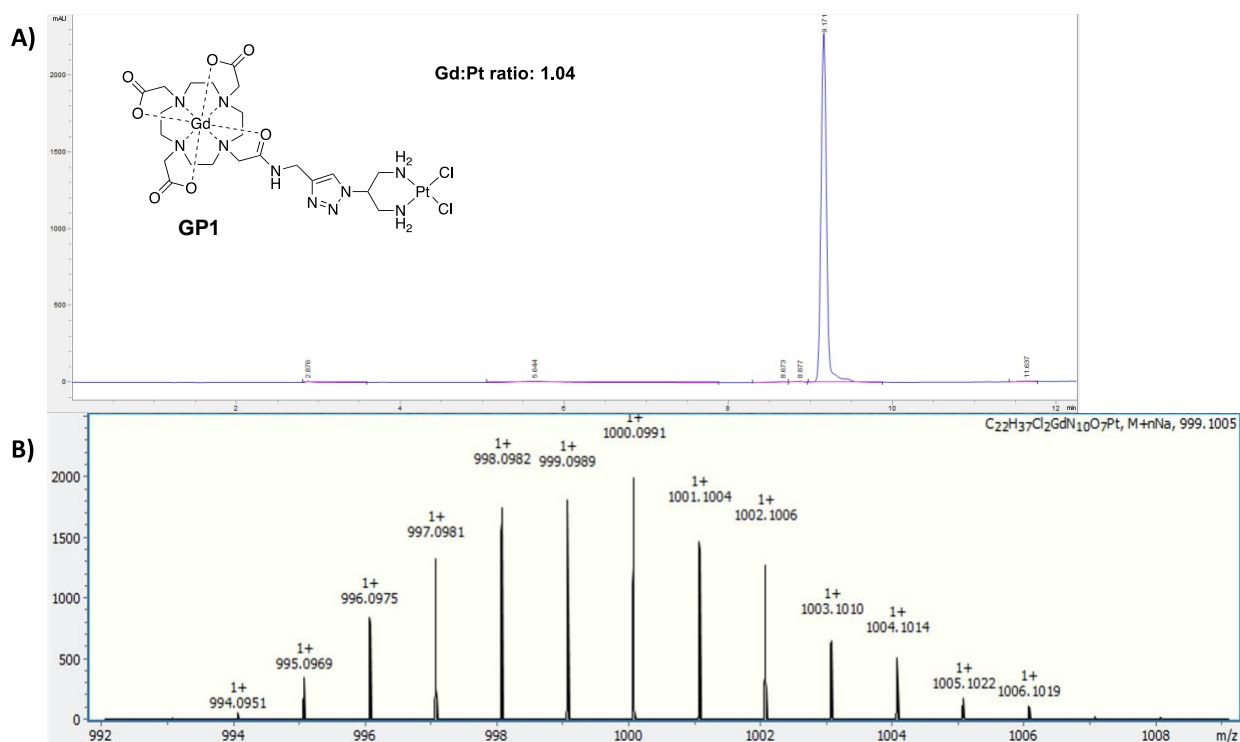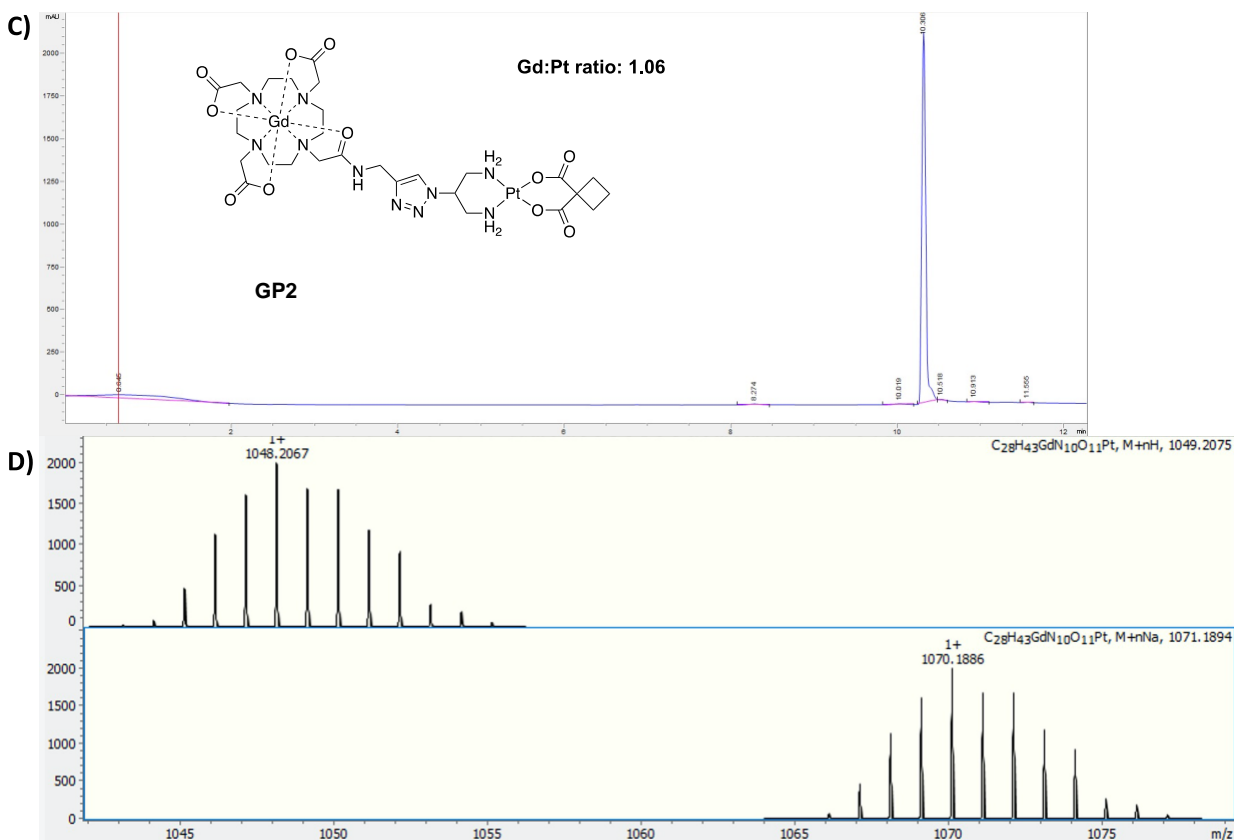
Figure A.1.1. (A) HPLC chromatogram of **GP1** (retention time=9.17 min) with Gd:Pt ratio determined by ICP-MS. (B) HRMS spectrum of purified **GP1**. (C) HPLC chromatogram of **GP2** (retention time=10.31 min) with Gd:Pt ratio. (D) HRMS spectrum of purified **GP2**.

Relaxivity Measurements:

Table A.1.1. r_2 values of **GP1** and **GP2** at low (1.41 T) and high (7 T) field strength in tris buffer at 37 °C

Agent:	Low Field (1.41 T)		High Field (7 T)	
	w/o CT-DNA	w/ CT-DNA	w/o CT-DNA	w/ CT-DNA
GP1	7.8	20.2	9.5	23.7
GP2	13.6	28.4	14.6	31.2
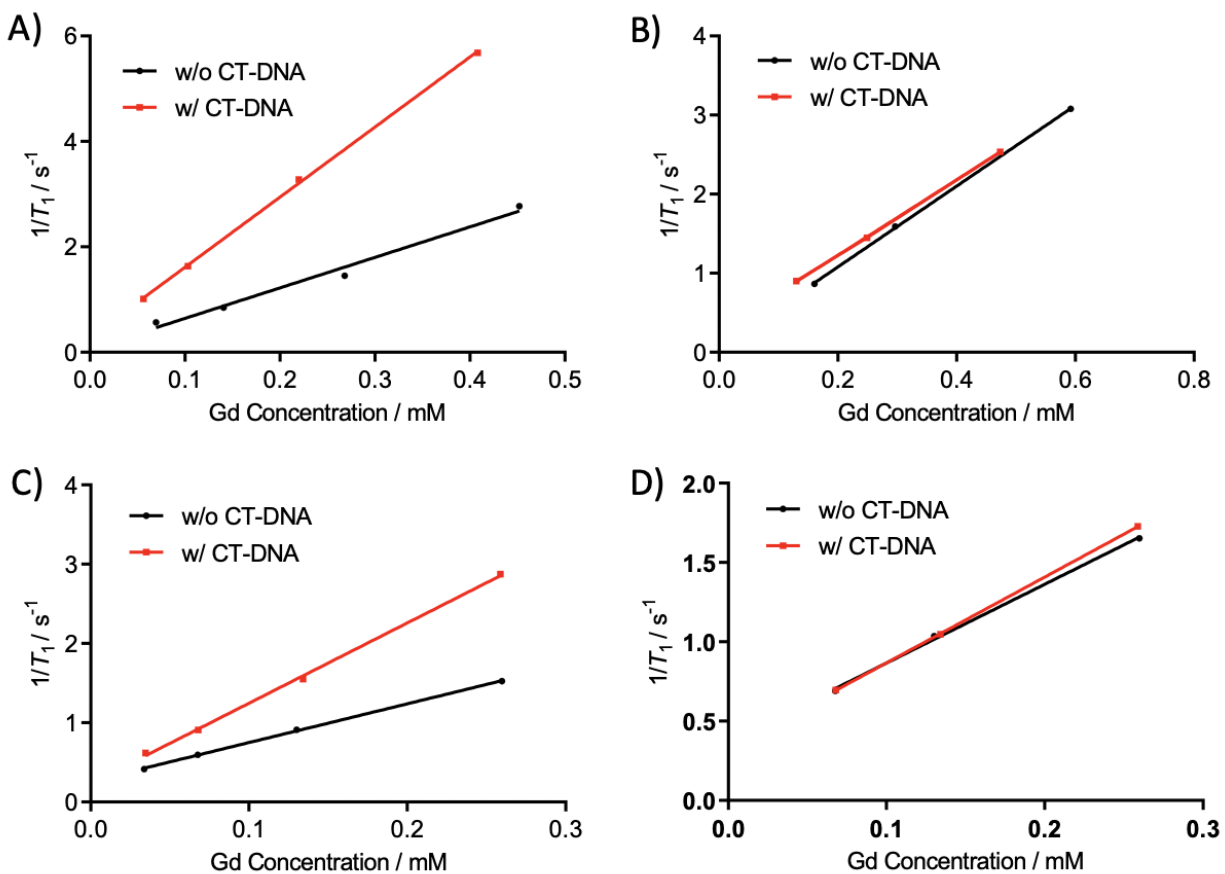
Figure A.1.2. T_1 relaxivity (r_1) plots of (A) **GP1** with and without CT-DNA in tris buffer at 1.41 T and 37 °C. (B) **GP1** with and without CT-DNA in tris buffer at 7 T and 37 °C. (C) **GP2** with and without CT-DNA in tris buffer at 1.41 T and 37 °C. (D) **GP2** with and without CT-DNA in tris buffer at 7 T and 37 °C.

CD-Spectra:
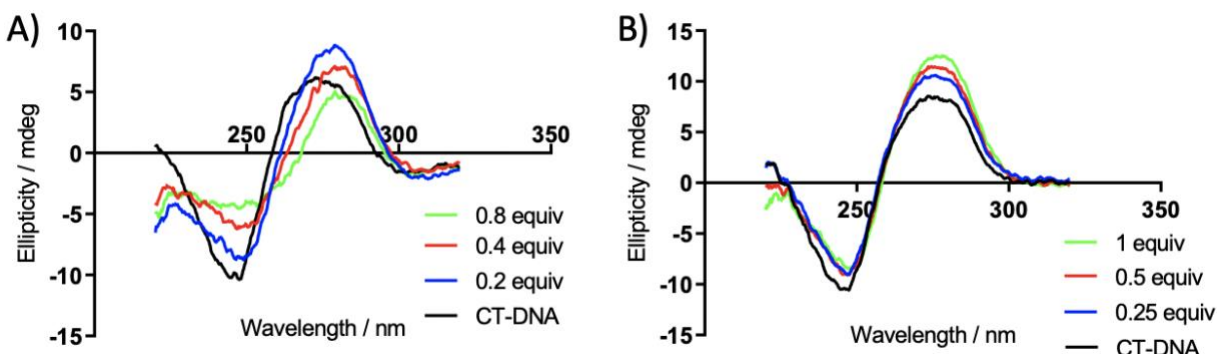
Figure A.1.3. CD spectra of 100 µM CT-DNA in tris buffer incubated with varying equivalents of (A) cisplatin for 24 h at 37 °C and (B) carboplatin for 24 h at 37 °C.

IC50 Curves:
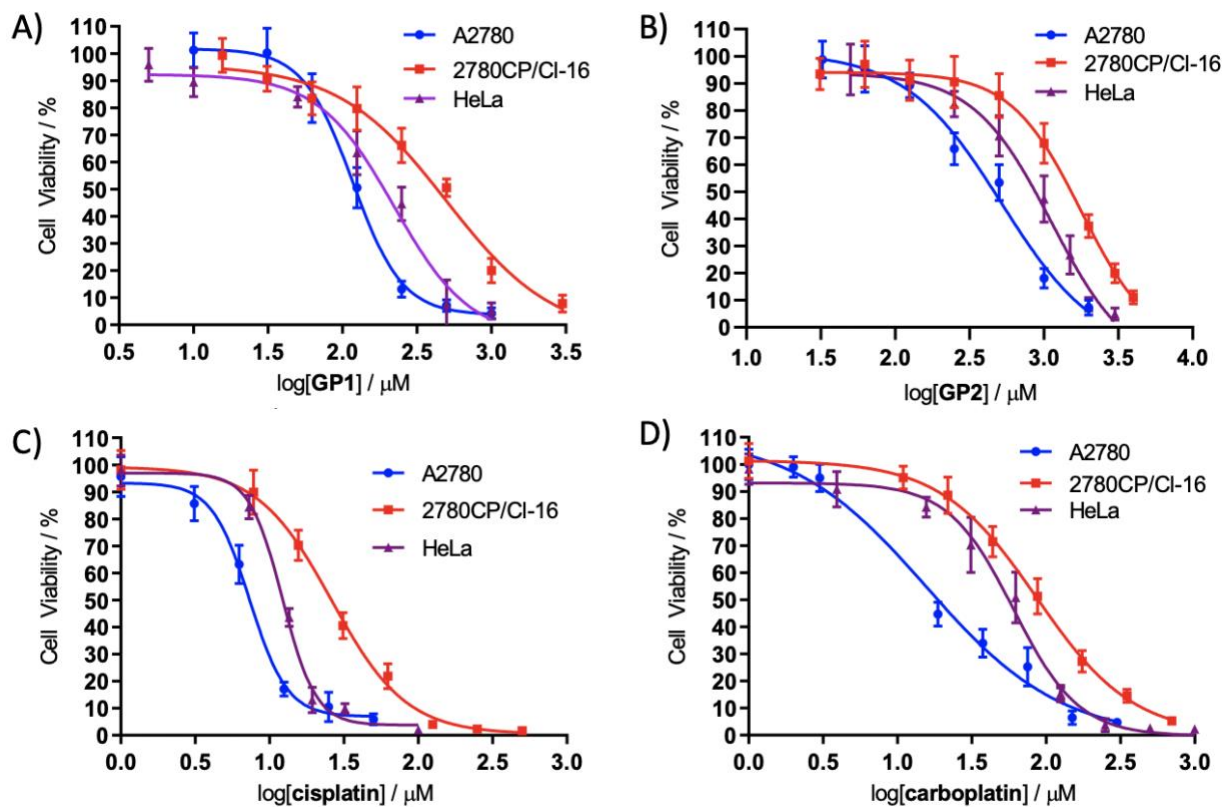
Figure A.1.4. IC$_{50}$ curves of (A) **GP1** (B) **GP2** (C) cisplatin and (D) carboplatin in A2780, 2780CP/Cl-16, and HeLa cells. Cells were incubated with **GP1** and cisplatin for 48 h and **GP2** and carboplatin for 72 h. Cell viability was measured with CellTiter-Glo 2.0.

Time-Dependent Uptake:
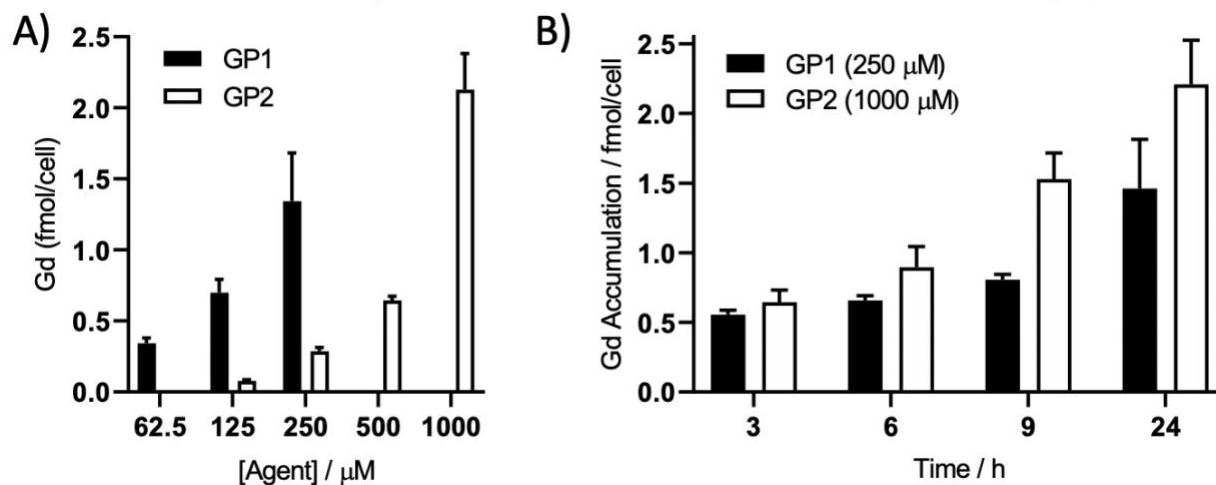
Figure A.1.5. (A) Concentration-dependent uptake of **GP1** and **GP2** in HeLa cells over 24 h. MR relevant concentrations of both agents accumulate in HeLa cells. (B) Time-dependent uptake of 250 μM **GP1** and 1000 μM **GP2** (~IC$_{50}$ values) in HeLa cells. MR relevant amounts of both agents accumulate in as little as 3 hours when dosed at the IC$_{50}$.

In Vivo MR Imaging:
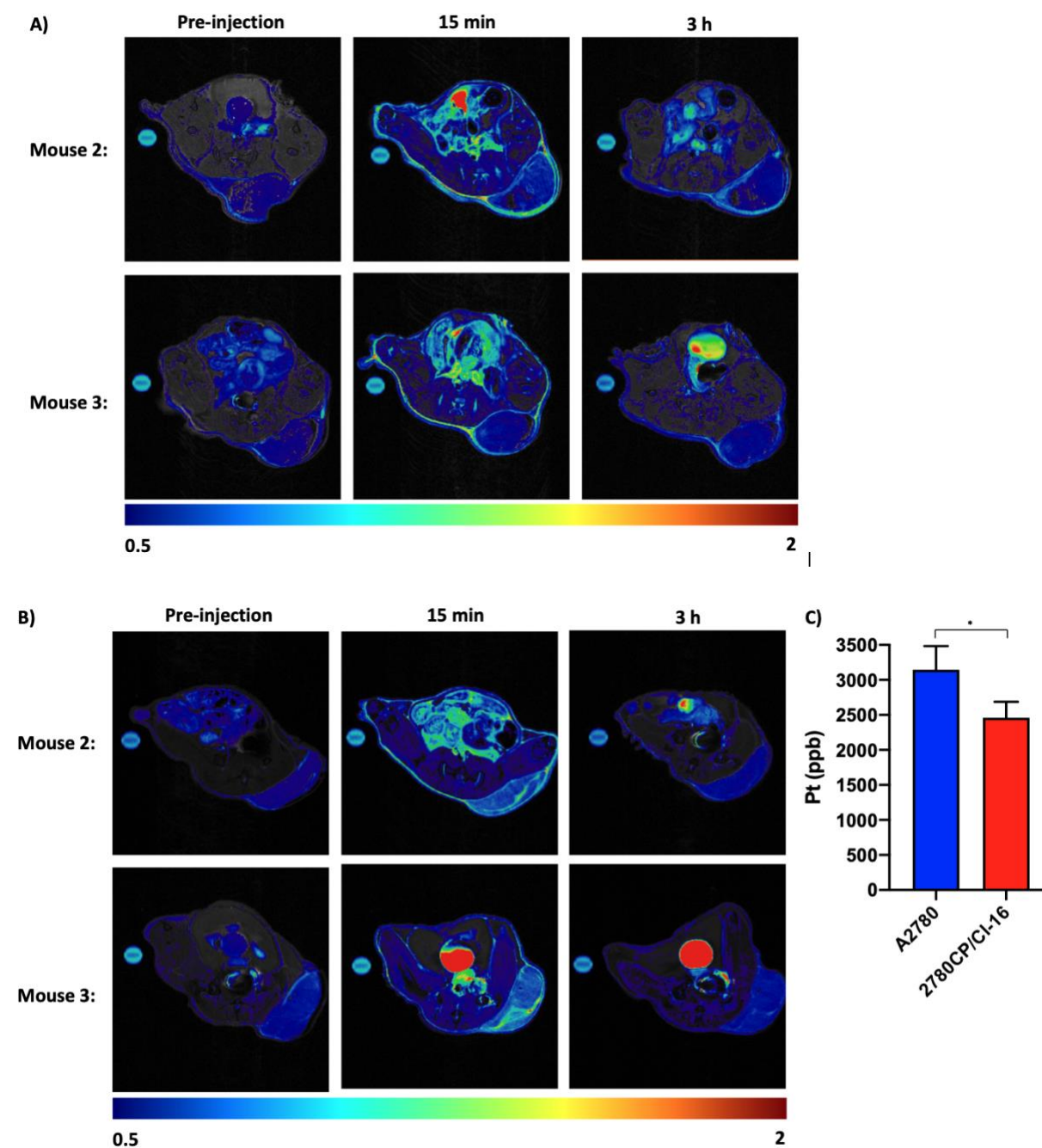
Figure A.1.6. MR imaging at 9.4 T of additional (A) A2780 tumor-bearing mice and (B) 2780CP/Cl-16 tumor-bearing mice given 0.15 mmol/kg **GP1** through IV injection. (C) Pt(II) accumulation in A2780 and 2780CP/Cl-16 tumors measured by ICP-MS (n=3 for each tumor type). There was a statistically significant difference (p<0.05) in accumulation of Pt(II) in the two tumor types, similar to Gd(III).
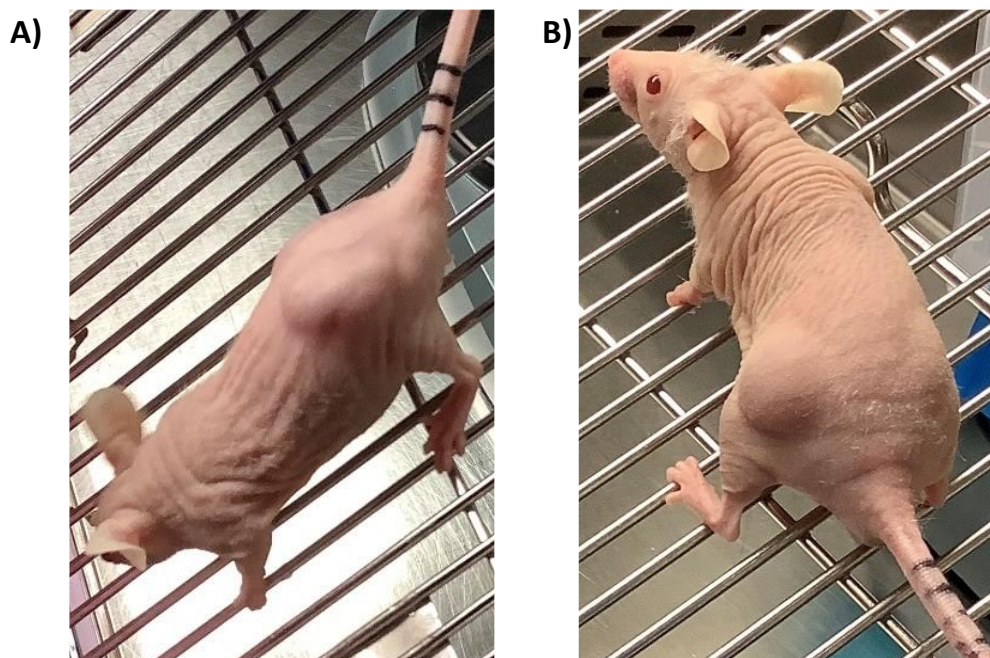
Figure A.1.7. Representative pictures of athymic nude mice bearing an (A) A2780 flank tumor and (B) 2780CP/Cl-16 flank tumor.

APPENDIX 2

SUPPORTING INFORMATION FOR CHAPTER 3

General Methods. Unless otherwise indicated, all reactions were performed under a nitrogen atmosphere using oven-dried glassware. Anhydrous solvents were used in all reactions and obtained from a J.C. Meyer solvent system (Laguna Beach, CA). Thin-layer chromatography (TLC) was performed on EMD 60 F254 silica gel plates. Standard grade 60 Å 230–400 mesh silica gel was used for normal-phase column chromatography. Unless otherwise stated, all silica gel columns were flashed with air. 1H and 13C NMR spectra were obtained on a Bruker 500 MHz Avance III NMR spectrometer. ESI-MS was performed on a Bruker AmaZon-SL spectrometer.

Cyclen was obtained from Strem Chemical, while all other reagents were purchased from Sigma Aldrich, Fisher Scientific, or TCI and used without purification. Analytical HPLC-MS was performed on an Agilent 1260 Infinity II HPLC system with an in-line Agilent 6120 Quad mass spectrometer. Semi-preparative HPLC was performed on an Agilent PrepStar 218 equipped with an Agilent 1260 Infinity diode array detector. HPLC purifications utilized deionized water (18.2 MΩ·cm) obtained from a Millipore Q-Guard System and HPLC grade MeCN, formic acid, and ammonium hydroxide (all obtained from Fisher Scientific).

Analytical HPLC-MS used an Atlantis C18 column (4.6 × 250 mm, 5 μm). Semipreparative HPLC used an Atlantis T3 C18 column (19 x 250 mm, 10 μm). **GP1** and **GP2** were purified using the following method: MeCN held at 0% for 5 min followed by a 25 min ramp to 75% followed by a 5 min ramp to 100%.

Synthesis of GP1. 9.0 mg **1** (0.015 mmol) were added to a 10 mL round bottom flask and dissolved in 3 mL of dry DMSO. 4.7 mg TBTU (0.015 mmol) and 2 μL triethylamine (0.015 mmol) were added and the solution was heated to 45 °C and stirred for 10 min. 7.3 mg **2** (0.023 mmol) were

added and the reaction was stirred at 45 °C under nitrogen over night. The reaction mixture was lyophilized to dryness, dissolved in H_2O, and purified by semipreparative HPLC (retention time: 13.8 min) in 44% yield. Analytical HPLC-MS trace of the purified product is found in Fig. S1A. ESI-MS m/z observed: 931.7, calculated: 931.1 $[M+H]^+$.

Synthesis of GP2. 5.5 mg **1** (0.009 mmol) were added to a 10 mL round bottom flask and dissolved in 2 mL of dry DMSO. 2.9 mg TBTU (0.009 mmol) and 1.2 μL triethylamine (0.009 mmol) were added and the solution was heated to 45 °C and stirred for 10 min. 5.5 mg **3** (0.014 mmol) were added and the reaction was stirred at 45 °C under nitrogen over night. The reaction mixture was then lyophilized to dryness, dissolved in H_2O, and purified by semipreparative HPLC (retention time: 15.3 min) in 56% yield. Analytical HPLC-MS trace of the purified product is found in Fig. S1B. ESI-MS m/z observed: 1003.4, calculated: 1003.19 $[M+H]^+$.

Relaxivity Measurements at 1.41 T. GP1 and **GP2**, and **1** were dissolved in 1 mL of PBS or 5 mM GSH in PBS. Each solution was serially diluted to make solutions of varying concentration. Relaxation times were measured on a Bruker mq60 NMR analyzer equipped with Minispec v 2.51 Rev.00/NT software (Bruker Biospin, Billerica, MA, USA) operating at 1.41 T (60MHz) and 37 °C. Measurements were made using an inversion recovery pulse sequence (T_1_ir_mb) using the following parameters: 4 scans per point, 10 data points, monoexponential curve fitting, phase cycling, 10 ms first pulse separation, and a recycle delay and final pulse separation ≥ 5 T_1. 10 μL aliquots of each solution were taken for ICP-MS analysis to determine the concentration of Gd(III).

Relaxivity Measurements at 7 T. GP1 and **GP2** and **1** were dissolved in 200 μL PBS or 5 mM

GSH and each solution was serially diluted to make solutions of varying concentration. 25 μL of

each solution were pipetted into flame sealed Pasteur pipettes. The pipette tips containing solution

were scored, separated, and sealed with parafilm to make small capillaries containing solution.

These capillaries were imaged using a Bruker PharmaScan 7 T MR imaging spectrometer (Bruker

BioSpin, Billerica, MA, USA). T_1 relaxation times were measured using a rapid-acquisition rapid-

echo (RARE-VTR) T_1-map pulse sequence with static T_E (10 ms) and variable T_R (100, 200, 400,

500, 750, 1000, 2500, 7500, and 1000 ms) values. Imaging parameters were as follows: field of

view (FOV) = 25 x 25 mm^2, matrix size (MTX) = 256 x 256, number of axial slices = 5, slice

thickness (SI) = 1.0 mm, and averages (NEX) = 4. T_1 analysis was carried out using the image

sequence analysis tool in Paravision 5.0 pl2 software (Bruker, Billerica, MA, USA) with

monoexponential curve-fitting of image intensities of selected regions of interest (ROIs) for each

axial slice.

Stability of GP1 and GP2 in various aqueous media. Aliquots of **GP1** and **GP2** were prepared

from a stock with known mass checked by ICP-MS. An aliquot of each was dissolved in H_2O and

analyzed by HPLC-MS using an Atlantis C18 column (4.6 × 250 mm, 5 μm) and the following

method: MeCN held at 0% for 3 min followed by a 15 min ramp to 100% MeCN (**GP1** retention

time: 10.9 min, **GP2** retention time: 11.6 min). Aliquots of both were additionally dissolved in

PBS, MEM, RPMI-1640, pH 5 H_2O, PBS with 10 units/mL porcine liver esterase, 5 mM

glutathione, and 5 mM sodium ascorbate, incubated in a shaker at 37 °C, and were analyzed by HPLC-MS at different time points using the same method. At each time point, the area of the peak of **GP1** or **GP2** was determined by integration and compared to the area of the peaks in H_2O. Difference in peak area was used as a means of determining the percentage of agent remaining in solution.

Cell Lines and Culture. A2780 cells were cultured using RPMI-1640 supplemented with 10% FBS. HeLa cells were cultured using phenol red free DMEM supplemented with 10% FBS. MCF-7 cells were cultured using phenol-red free MEM supplemented with 10% FBS. All three cell lines were grown in a humidified incubator at 37 °C and 5% CO_2 and were harvested using 0.25% TrypLE. Cells were grown for 24 hours after plating before each experiment. All solutions were filtered through 0.2 μL sterile filters before use.

Viability Assays. A2780, HeLa, and MCF-7 cells were plated at a density of 3,000 cells per well (100 μL) in an opaque white 96-well plate. Cells were dosed with 100 μL of solutions of **GP1**, **GP2**, cisplatin, or carboplatin in MEM and incubated for 48 hours (**GP1** or cisplatin) or 72 hours (**GP2** or carboplatin). After incubation, 50 μL CellTiter-Glo 2.0 (Promega, Madison, WI) was added to each well and the assay was carried out following the manufacturer's protocol. Luminescence of the wells was measured using a Synergy H1 microplate reader (BioTek, Winooski, VT). Viability was determined by comparing luminescence readings of the cells treated with agent to untreated control cells.

Concentration-dependent Cell Uptake. A2780 and HeLa cells were plated at a density of 40,000 cells per well (500 μL) in a 24-well plate. Cells were incubated with **GP1**, **GP2**, **1**, cisplatin or carboplatin at varying concentrations in MEM (300 μL) for 24 hours. After 24 hours, the media was aspirated and the cells were washed twice with 500 μL of PBS, harvested, and centrifuged at 500 rpm for 5 minutes at 4°C. The media was aspirated and the cells were resuspended in 200 μL of media. A 50 μL aliquot was taken for cell counting using a Guava PCA system using the Guava Viacount protocol provided by the manufacturer. An additional 100 μL aliquot was used for ICP-MS analysis of Gd and Pt in the cells.

Cell fractionation experiments were performed using a cytosol/particulate rapid separation kit (BioVision, Milpitas, CA). Uptake experiments were performed in the same way, following the manufacturer's protocol after the first centrifugation. Gd and Pt content in each fraction was determined by ICP-MS and the total uptake for a given set of cells was taken to be the sum of the cytosol and particulate fractions.

Time-dependent Cellular Uptake. A2780 cells were plated at a density of 40,000 cells per well (500 μL) in a 24-well plate. Cells were incubated with 300 μL of 65 μM **GP1** or 62.5 μM **GP2** in MEM for variable amounts of time (0.5, 1, 2, 3, 6, 24 h). At each timepoint, the media was aspirated and the cells were washed twice with 500 μL of PBS, harvested, and centrifuged at 500 rpm for 5 minutes at 4°C. The media was aspirated and the cells were resuspended in 200 μL of media. A 50

µL aliquot was taken for cell counting using a Guava PCA system using the Guava Viacount protocol provided by the manufacturer. An additional 100 µL aliquot was used for ICP-MS analysis of Gd and Pt in the cells.

MR Imaging of Cell Pellets at 7 T. A2780 and HeLa cells were grown to ~60% confluency in T-75 flasks. A2780 cells were dosed with 5 mL of 30 µM **GP1**, 60 µM **GP2**, 100 µM **1**, 7.5 µM, or vehicle (MEM) and HeLa cells were dosed with 5 mL of 60 µM **GP1**, 250 µM **GP2**, 100 µM **1**, 15 µM, or vehicle (MEM). Cells were incubated for 6 hours. After incubation, the media was aspirated and the cells were washed twice with 5 mL PBS, harvested, and centrifuged at 500 rpm for 5 min at 4 °C. The cells were resuspended in 1 mL of media and 950 µL of the suspension was added to flame-sealed Pasteur pipettes while the rest was used for cell counting and ICP-MS. The pipettes were centrifuged at 200 rpm for 5 minutes and were separated to form small capillaries containing the cell pellets. The capillaries were sealed with parafilm and imaged using a Bruker PharmaScan 7 T MR imaging spectrometer following the same imaging protocol previously described.

Cell Counting with a Guava EasyCyte Mini Personal Cell Analyzer (PCA) System. Aliquots of cell suspensions were mixed with the Guava ViaCount Reagent and allowed to stain for 5 minutes. The samples were vortexed for 20 seconds and cell count was determined via manual analysis using a Guava EasyCyte Mini PCA and ViaCount software. 1000 events were acquired for each sample and dilutions were performed to assure the cell count was in the optimal range for

instrument performance (10-100 cells/µL). Performance of the instrument was assessed daily using Guava-Check Beads and the manufacturer's protocol and Daily Check software.

Quantification of Gadolinium and Platinum with Inductively Coupled Plasma Mass Spectrometry. Quantification of Gd and Pt was accomplished using ICP-MS of acid digested samples. Specifically, samples were digested in concentrated trace nitric acid (> 69%, Thermo Fisher Scientific, Waltham, MA, USA) and trace hydrochloric acid (> 34%, Thermo Fisher Scientific, Waltham, MA, USA) and placed at 65 °C for at least 4 hours to allow for complete sample digestion. Ultra-pure H_2O (18.2 MΩ·cm) was then added to produce a final solution of 2.0% nitric acid and 2.0% hydrochloric acid (v/v) in a total sample volume of 10 mL. Quantitative standards were made using a 10,000 µg/mL Gd elemental standard and a 1,000 ug/mL Pt elemental standard (Inorganic Ventures, Christiansburg, VA, USA) which were used to create a 200 ng/g mixed element standard and a 2 ng/g mixed element standard in 2.0% nitric acid and 2.0% hydrochloric acid (v/v) in a total sample volume of 50 mL. A solution of 2.0% nitric acid and 2.0% hydrochloric acid (v/v) was used as the calibration blank.

ICP-MS was performed on a computer-controlled (QTEGRA software) Thermo iCapQ ICP-MS (Thermo Fisher Scientific, Waltham, MA, USA) operating in STD mode and equipped with a ESI SC-2DX PrepFAST autosampler (Omaha, NE, USA). Internal standard was added inline using the prepFAST system and consisted of 1 ng/mL of a mixed element solution containing Bi, In, ^{6}Li, Sc, Tb, Y (IV-ICPMS-71D from Inorganic Ventures). Online dilution was also carried out by the prepFAST system and used to generate a calibration curve consisting of 200, 100, 50, 20, 10, 2 ppb Gd and Pt and a calibration curve consisting of 2000, 1000, 500, 200, 100, and 20 ppt Gd and

Pt. Each sample was acquired using 1 survey run (10 sweeps) and 3 main (peak jumping) runs (40 sweeps). The isotopes selected for analysis were ^{194,195}Pt, ^{56,57}Gd, and ^{115}In, ^{159}Tb, ^{209}Bi (chosen as internal standards for data interpolation and machine stability). Instrument performance is optimized daily through autotuning followed by verification via a performance report (passing manufacturer specifications).

Figure A.2.1 (A) HPLC-MS trace of **GP1** purified by semipreparative HPLC. The reported Gd:Pt ratio was determined by ICP-MS analysis of all batches of **GP1**. (B) HPLC-MS of **GP2** purified by semipreparative HPLC. The reported Gd:Pt ratio was determined by ICP-MS analysis of all batches of **GP2**. (C) ESI-MS spectrum of purified **GP1**. (D) ESI-MS spectrum of purified **GP2**. (E) Predicted mass spectrum isotope pattern of **GP1**. (F) Predicted mass spectrum isotope pattern of **GP2**.
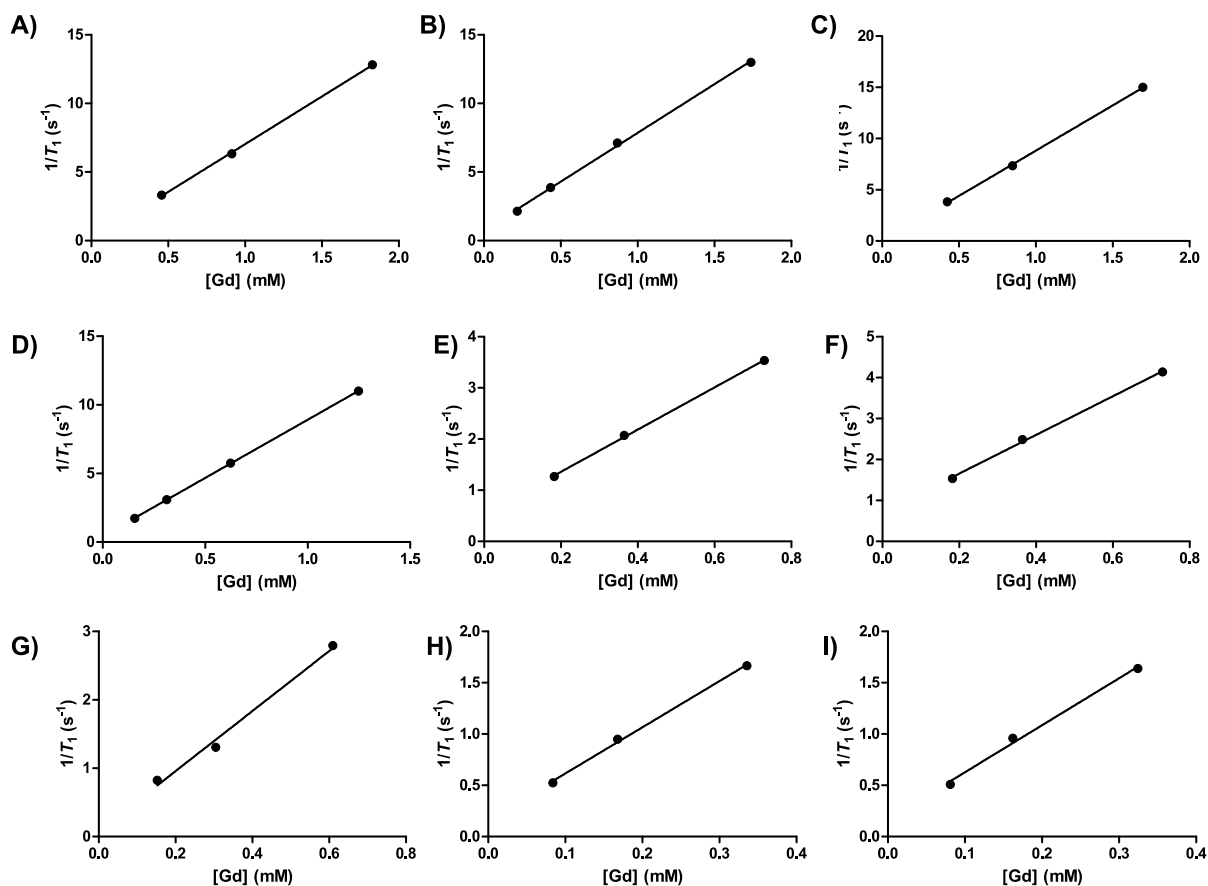
Figure A.2.2. Graph of r_1 of (A) **GP1** measured at 1.41 T (B) **GP1** measured at 7 T (C) **GP2** measured at 1.41 T (D) **GP2** measured at 7 T (E) **1** measured at 1.41 T (F) **1** measured at 7 T. All measurements were taken in PBS at 37 °C (G) **1** measured at 1.41 T with 5 mM GSH (H) **GP1** measured at 1.41 T with 5 mM GSH and (I) **GP2** measured at 1.41 T with 5 mM GSH.

Table A.2.1. r_1 of **GP1**, **GP2**, and **1** in PBS with 5 mM glutathione at 37 °C

	GP1 (5 mM GSH)	GP2 (5 mM GSH)	1 (5 mM GSH)
r_1 (mM^{-1}s^{-1}) at 1.41 T	4.5	4.6	4.4
r_2 (mM^{-1}s^{-1}) at 1.41 T	5.1	5.0	4.9

C) GP1 in MEM

0 h
48 h
MEM

D) GP1 in RPMI-1640

0 h
48 h
RPMI-1640

E) GP1 in pH 5.0 H_2O

0 h
48 h
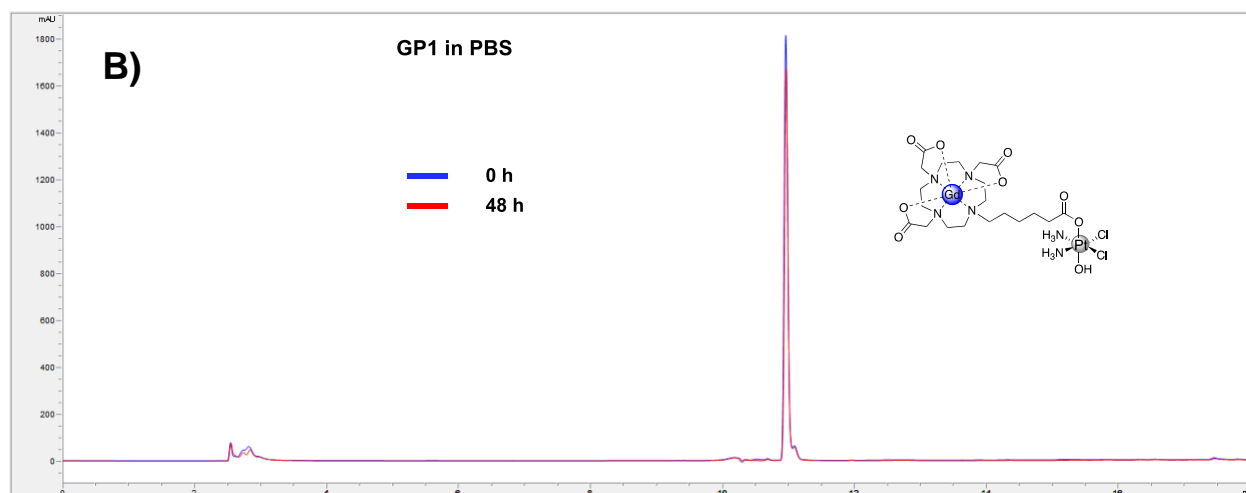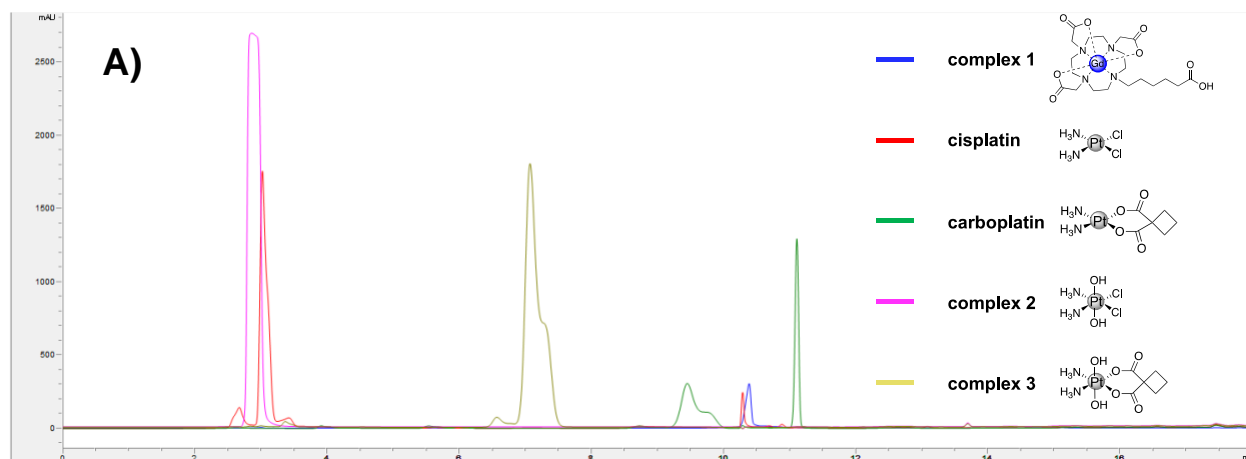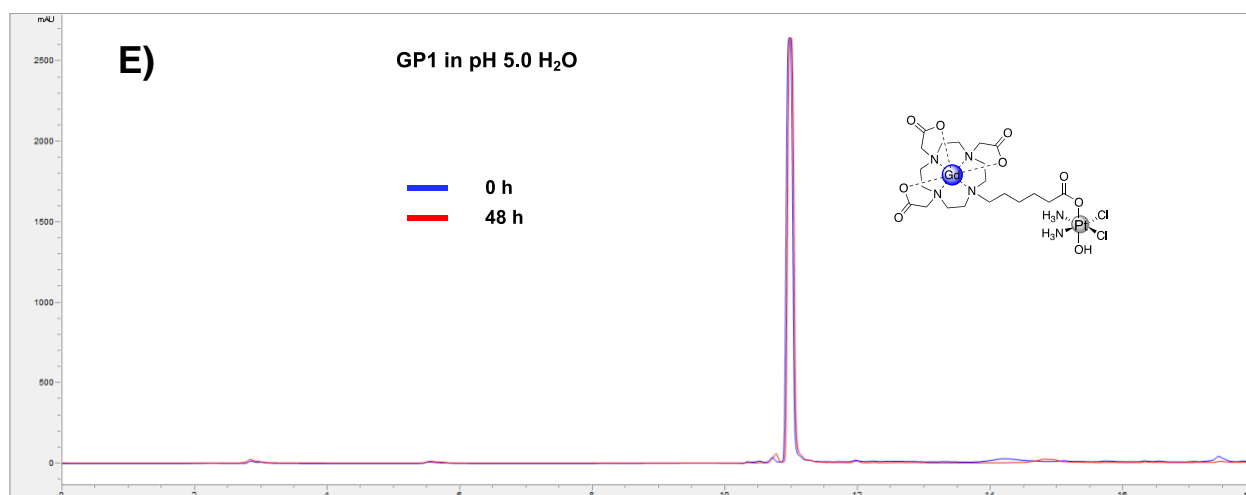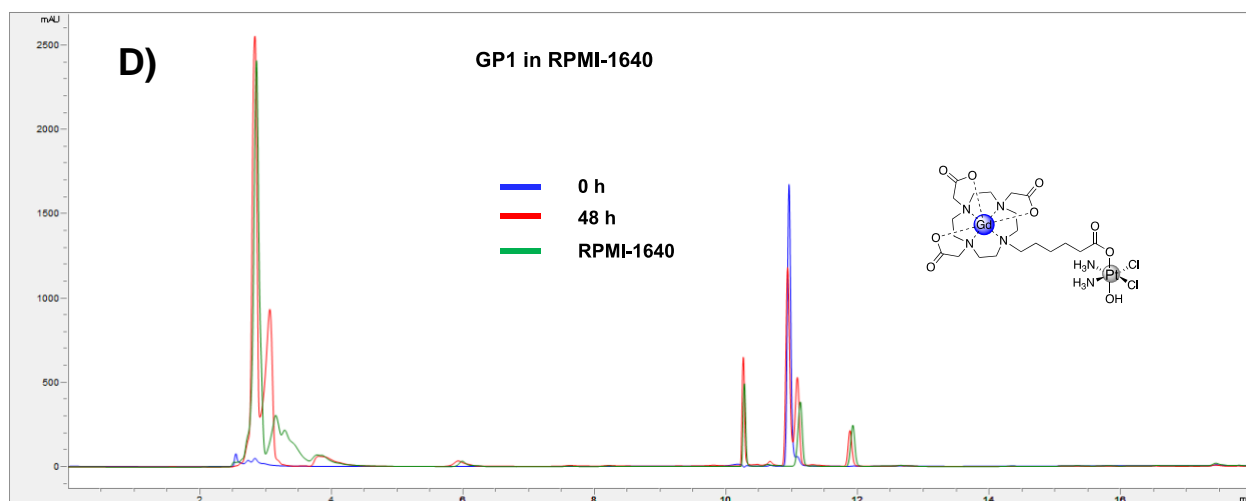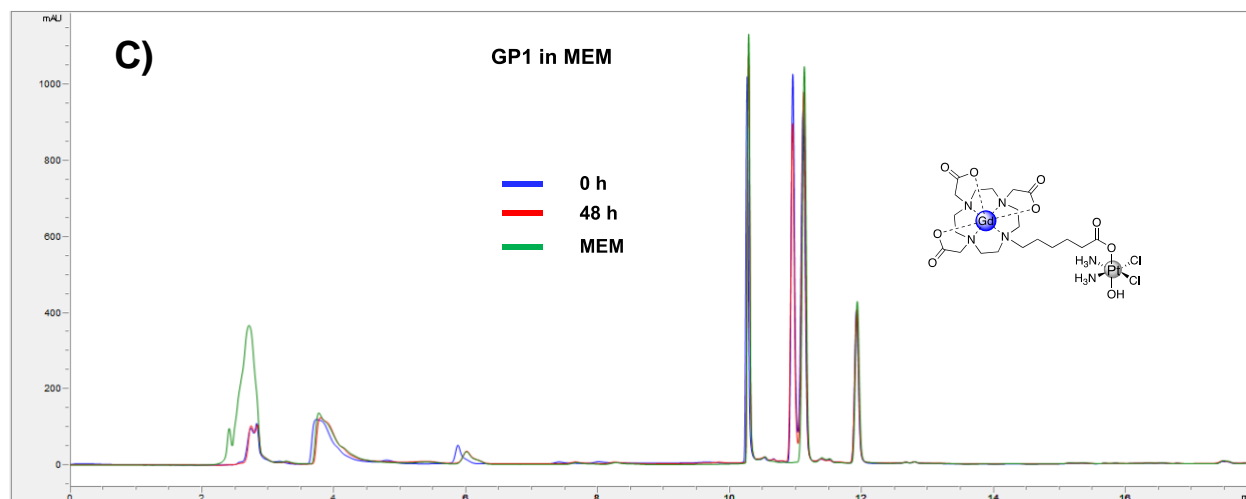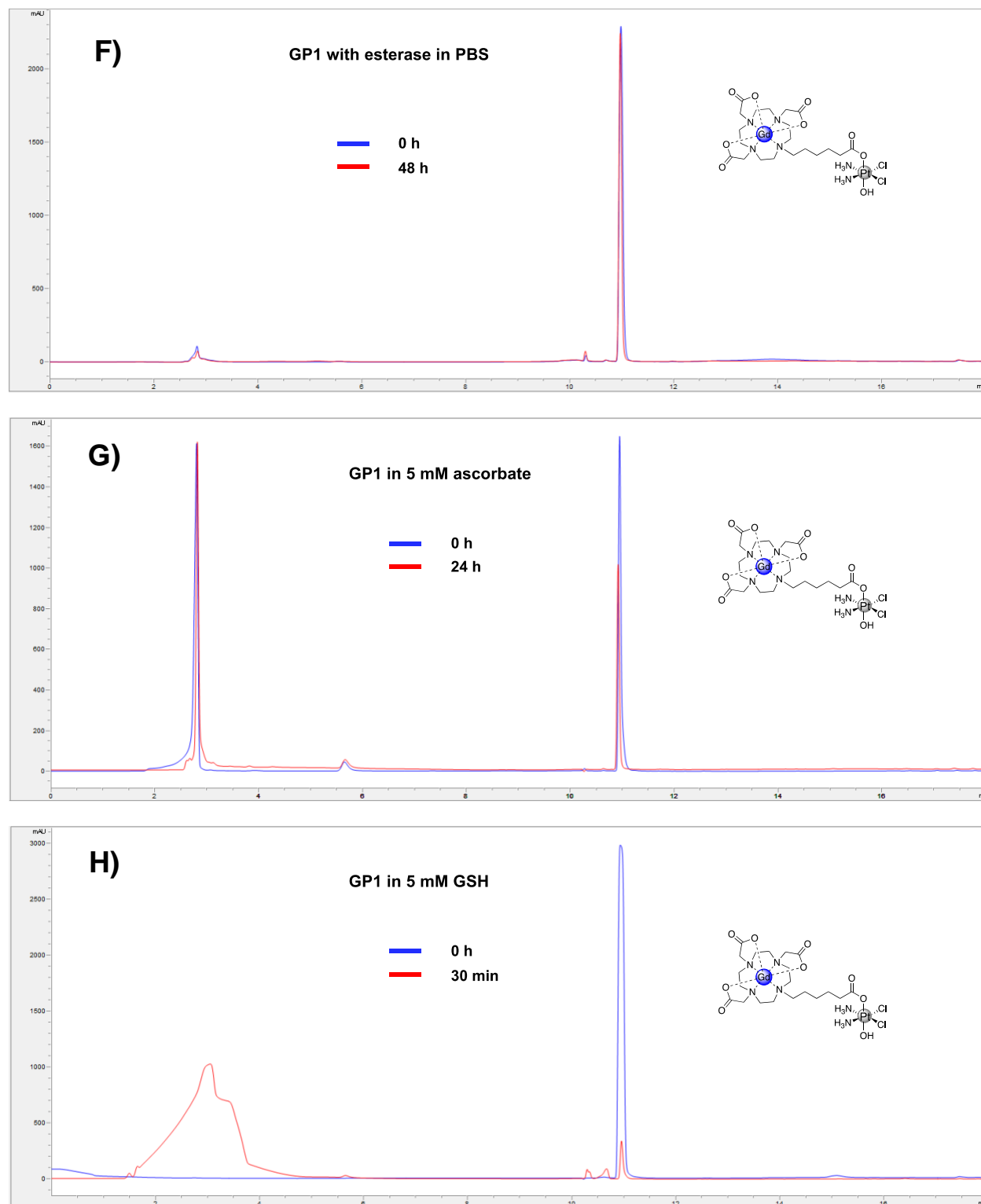
Figure A.2.3. Analytical HPLC chromatograms of (A) cisplatin, carboplatin, **1**, **2**, and **3** in H_2O (B) **GP1** in PBS over time (C) **GP1** in MEM over time (D) **GP1** in RPMI-1640 over time (E) **GP1**

in pH 5 H_2O over time (F) **GP1** in PBS with porcine liver esterase (PLE) over time (G) **GP1** in 5 mM ascorbate over time and (H) **GP1** in 5 mM glutathione (GSH) over time. All HPLC runs used the same method (0-3 min 100% H_2O followed by a 15 min ramp to 100% MeCN). These data demonstrate in non-reducing conditions, **GP1** is largely stable over long periods of time, but can be quickly reduced under intracellularly relevant conditions.

A) GP2 in PBS
— 0 h
— 48 h

B) GP2 in MEM
— 0 h
— 48 h
— MEM

C) GP2 in RPMI-1640
— 0 h
— 48 h
— RPMI-1640

D) GP2 in pH 5.0 H₂O
0 h
48 h

E) GP2 with esterase in PBS
0 h
48 h

F) GP2 in 5 mM ascorbate
0 h
24 h
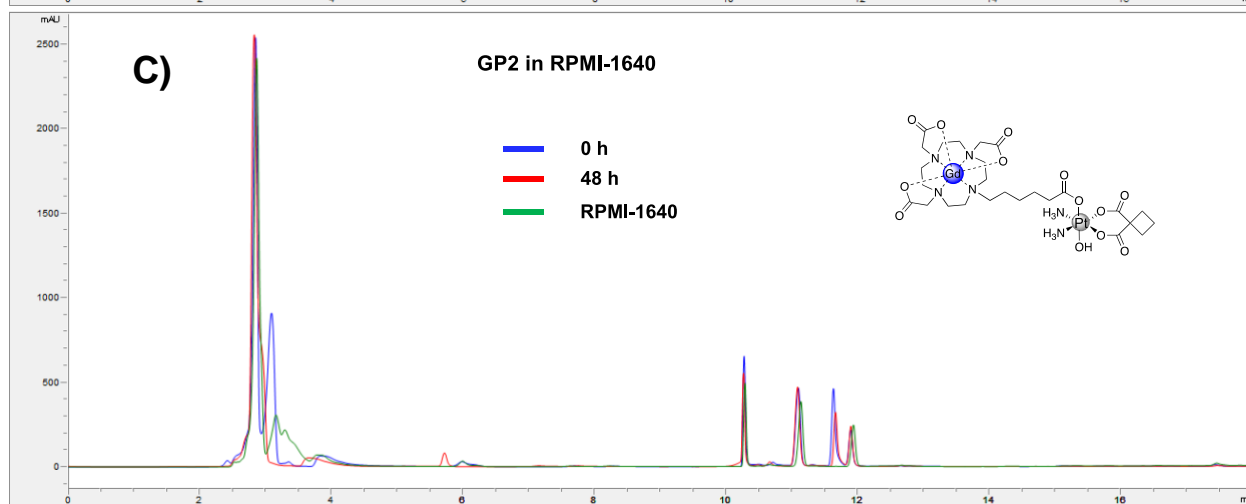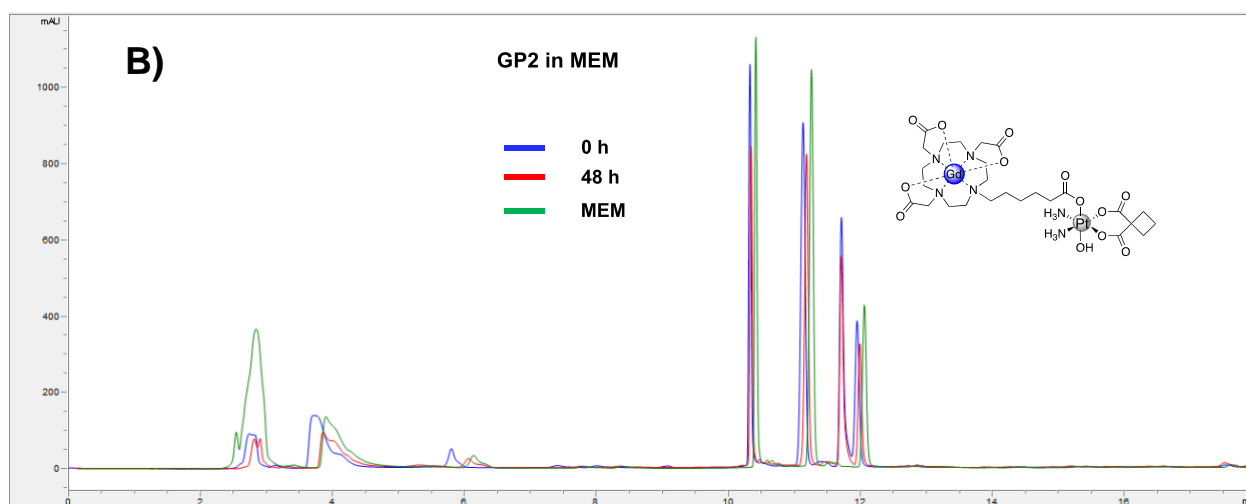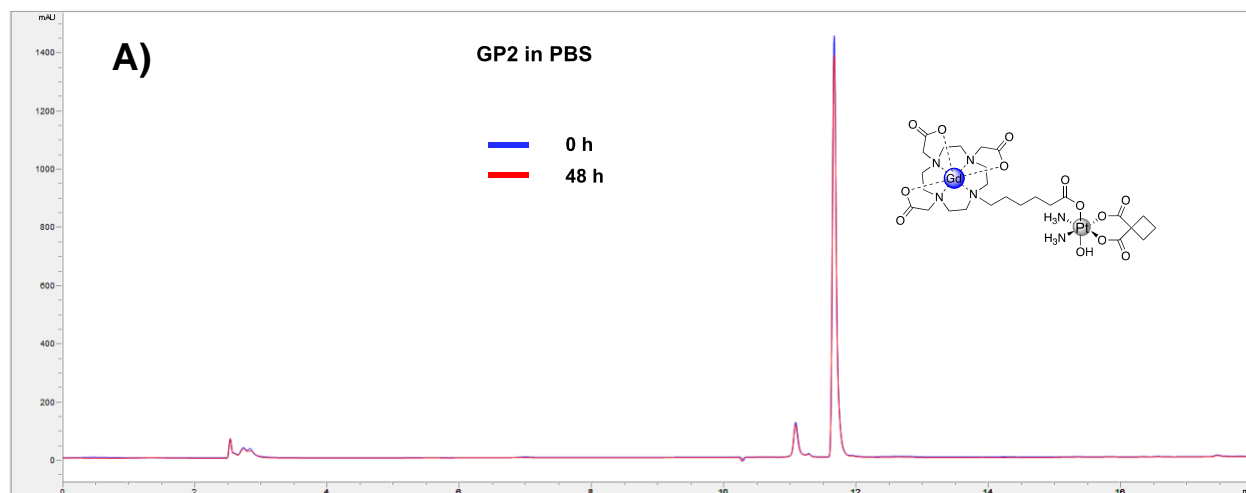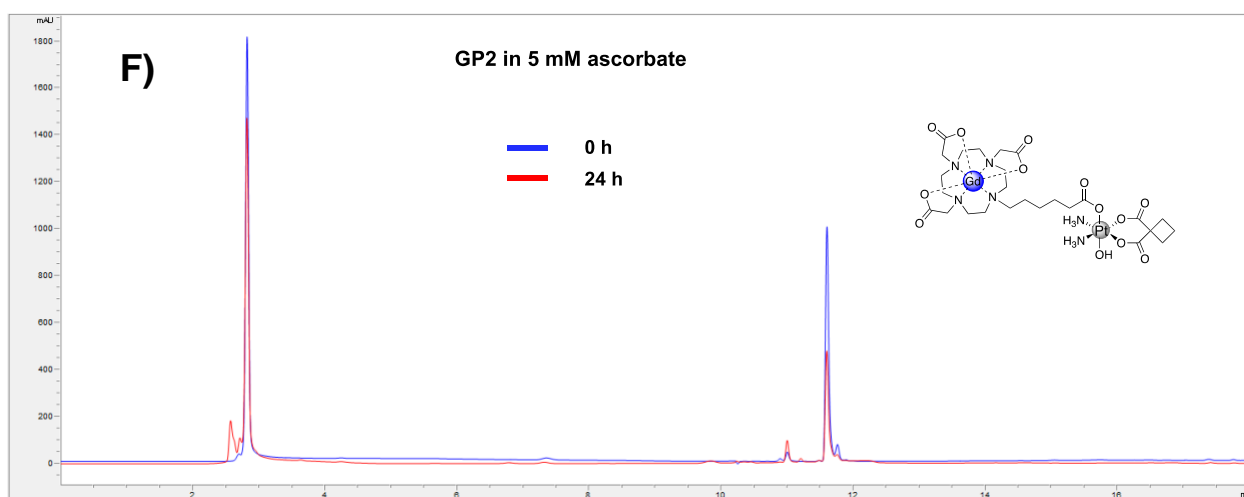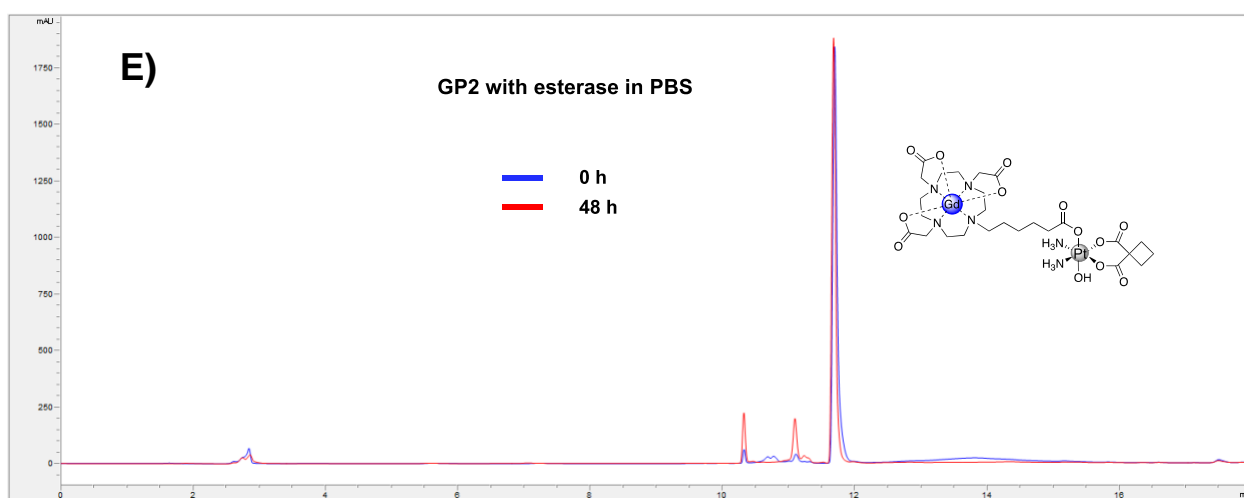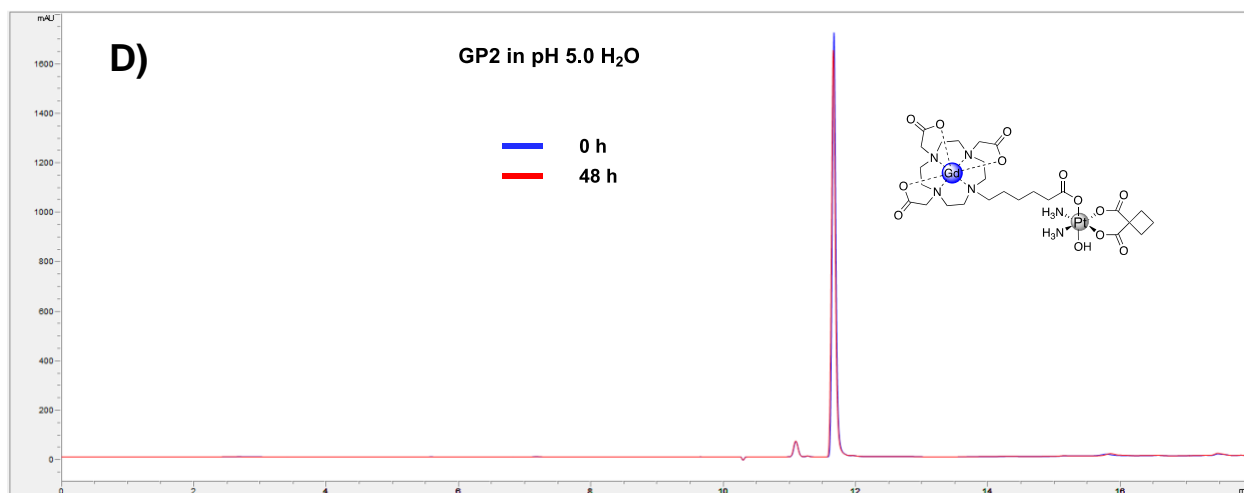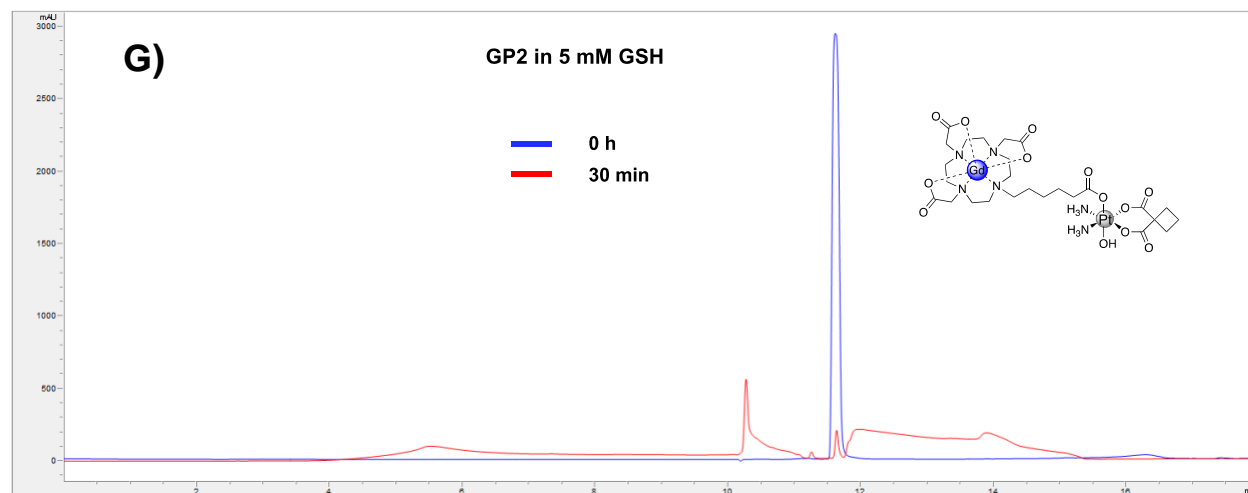
Figure A.2.4. Analytical HPLC chromatograms of **GP2** in (A) PBS over time (B) MEM over time (C) RPMI-1640 over time (D) pH 5 H$_2$O over time (E) PBS with porcine liver esterase (PLE) over time (F) 5 mM ascorbate over time and (G) 5 mM glutathione (GSH) over time. All HPLC runs used the same method (0-3 min 100% H$_2$O followed by a 15 min ramp to 100% MeCN). These data demonstrate that like **GP1**, **GP2** is largely stable over long periods of time in non-reducing conditions, but can be quickly reduced under intracellularly relevant conditions.
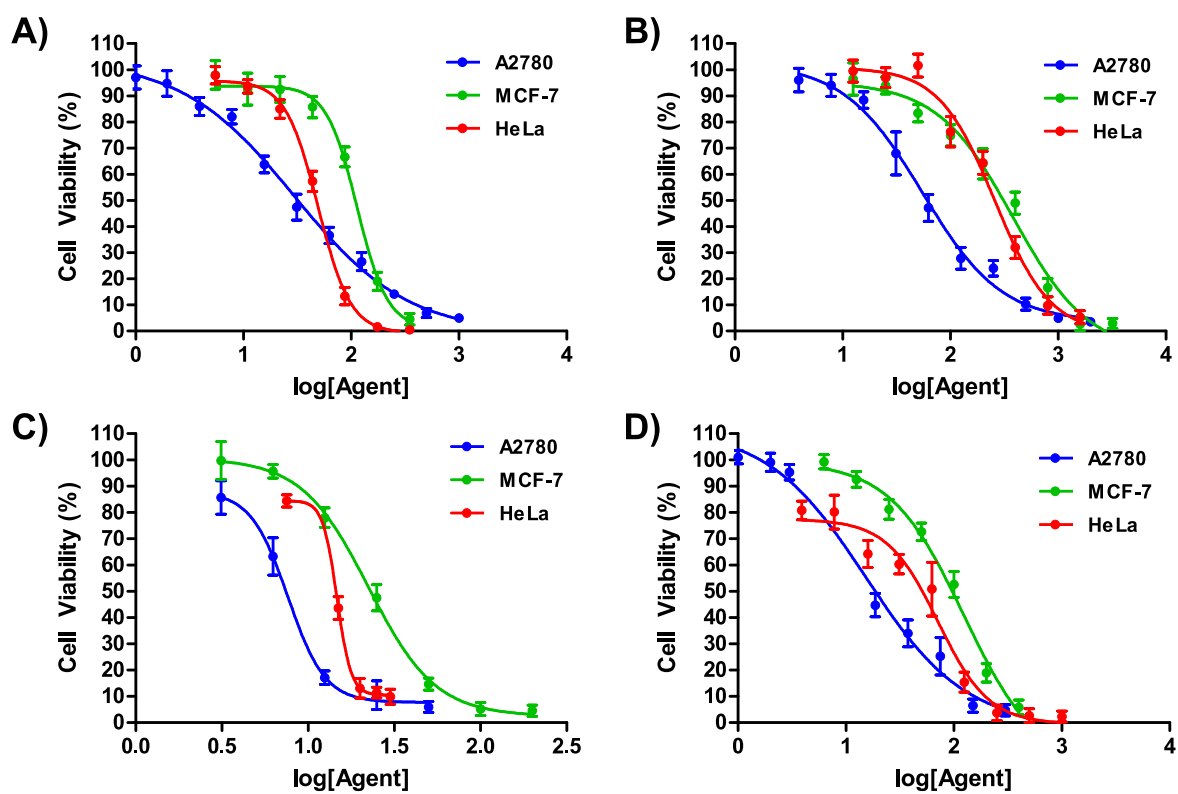
Figure A.2.5. (A) IC$_{50}$ curves of **GP1** in A2780, MCF-7, and HeLa cells. (B) IC$_{50}$ curves of **GP2** in A2780, MCF-7, and HeLa cells. (C) IC$_{50}$ curves of cisplatin in A2780, MCF-7, and HeLa cells. (D) IC$_{50}$ curves of carboplatin in A2780, MCF-7, and HeLa cells.
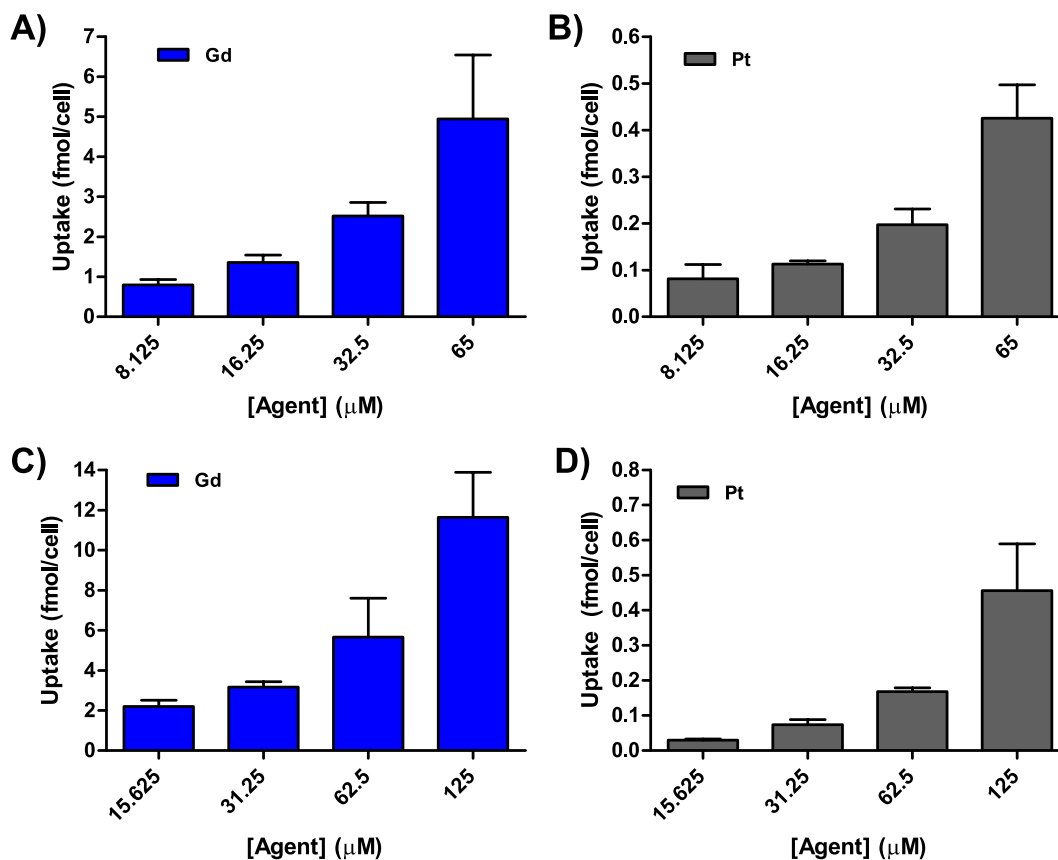
Figure A.2.6. (A) Accumulation of Gd in A2780 cells dosed with varying concentrations of **GP1** for 24 h. (B) Accumulation of Pt in A2780 cells dosed with varying concentrations of **GP1** for 24 h. (C) Accumulation of Gd in HeLa cells dosed with varying concentrations of **GP1** for 24 h. (D) Accumulation of Pt in HeLa cells dosed with varying concentrations of **GP1** for 24 h.
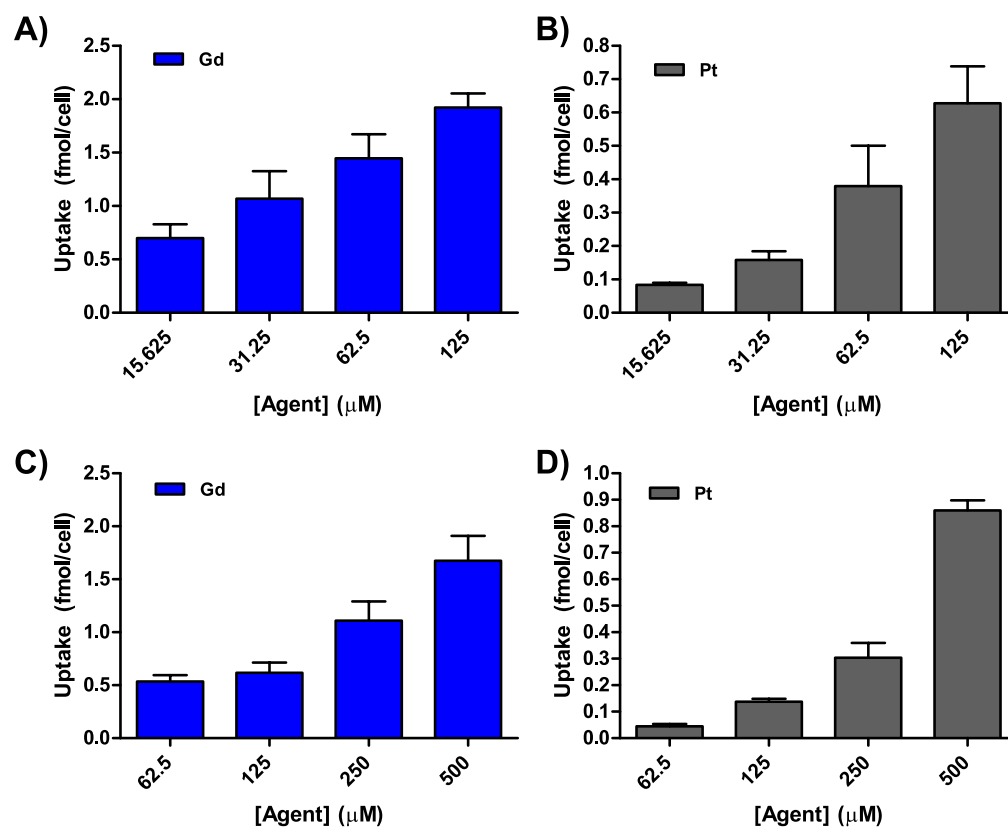
Figure A.2.7. (A) Accumulation of Gd in A2780 cells dosed with varying concentrations of **GP2** for 24 h. (B) Accumulation of Pt in A2780 cells dosed with varying concentrations of **GP2** for 24 h. (C) Accumulation of Gd in HeLa cells dosed with varying concentrations of **GP2** for 24 h. (D) Accumulation of Pt in HeLa cells dosed with varying concentrations of **GP2** for 24 h.
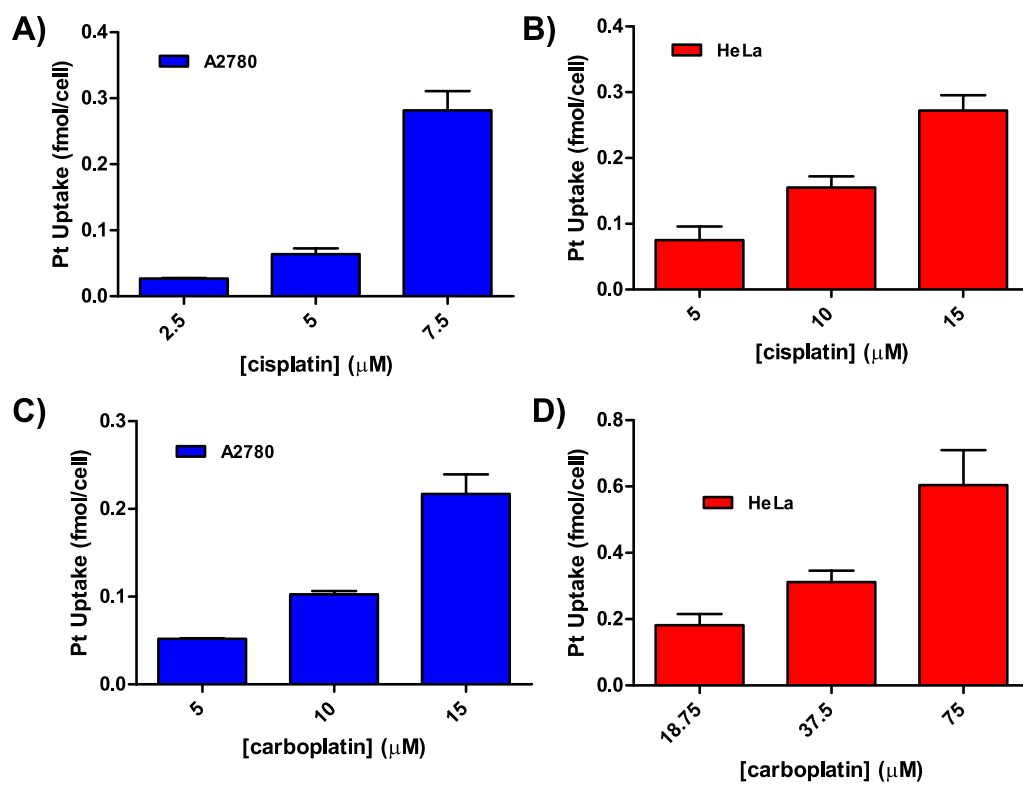
Figure A.2.8. (A) Accumulation of Pt in A2780 cells dosed with varying concentrations of cisplatin for 24 h. (B) Accumulation of Pt in HeLa cells dosed with varying concentrations of cisplatin for 24 h. (C) Accumulation of Pt in A2780 cells dosed with varying concentrations of carboplatin for 24 h. (D) Accumulation of Pt in HeLa cells dosed with varying concentrations of carboplatin for 24 h.
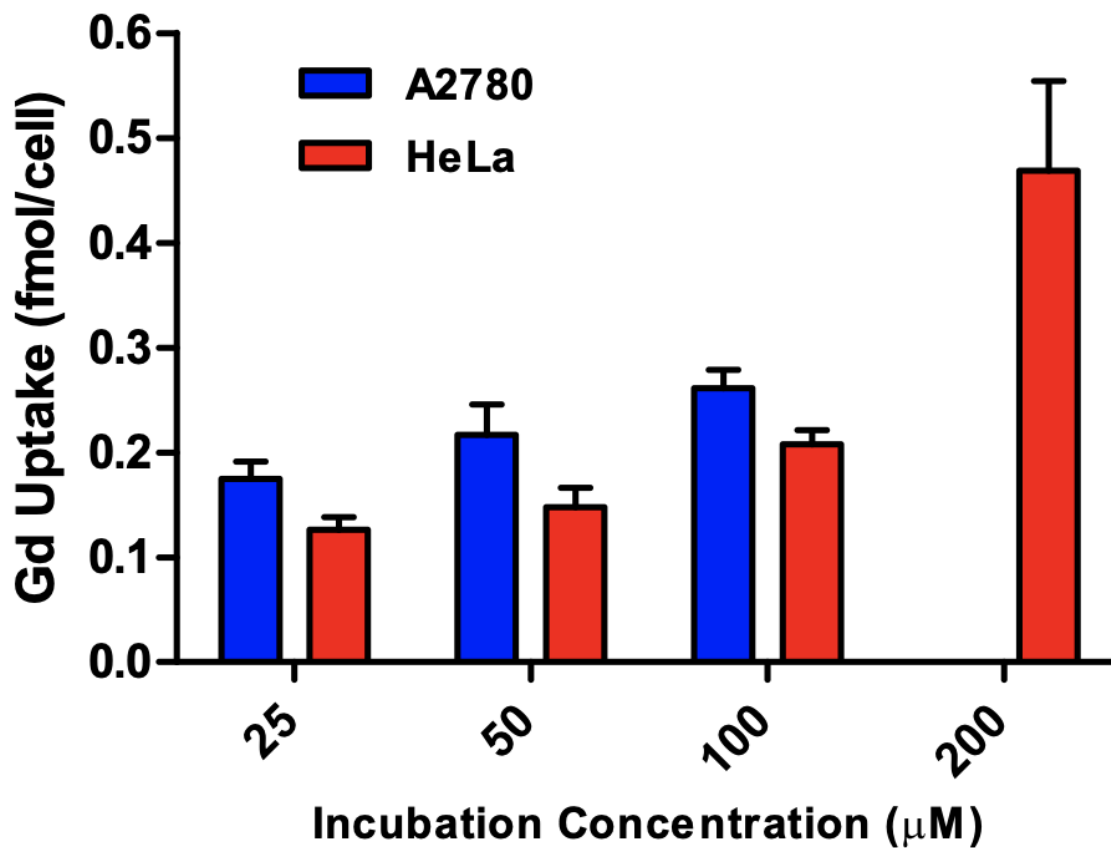
Figure A.2.9. Concentration dependent uptake of complex **1** in A2780 and HeLa cells after 24 hours. At incubation concentrations similar to **GP1** and **GP2**, **1** had significantly lower accumulation in both A2780 and HeLa cells. This supports that the Pt(IV) complexes are responsible for the higher uptake of **GP1** and **GP2** compared to complex **1**.
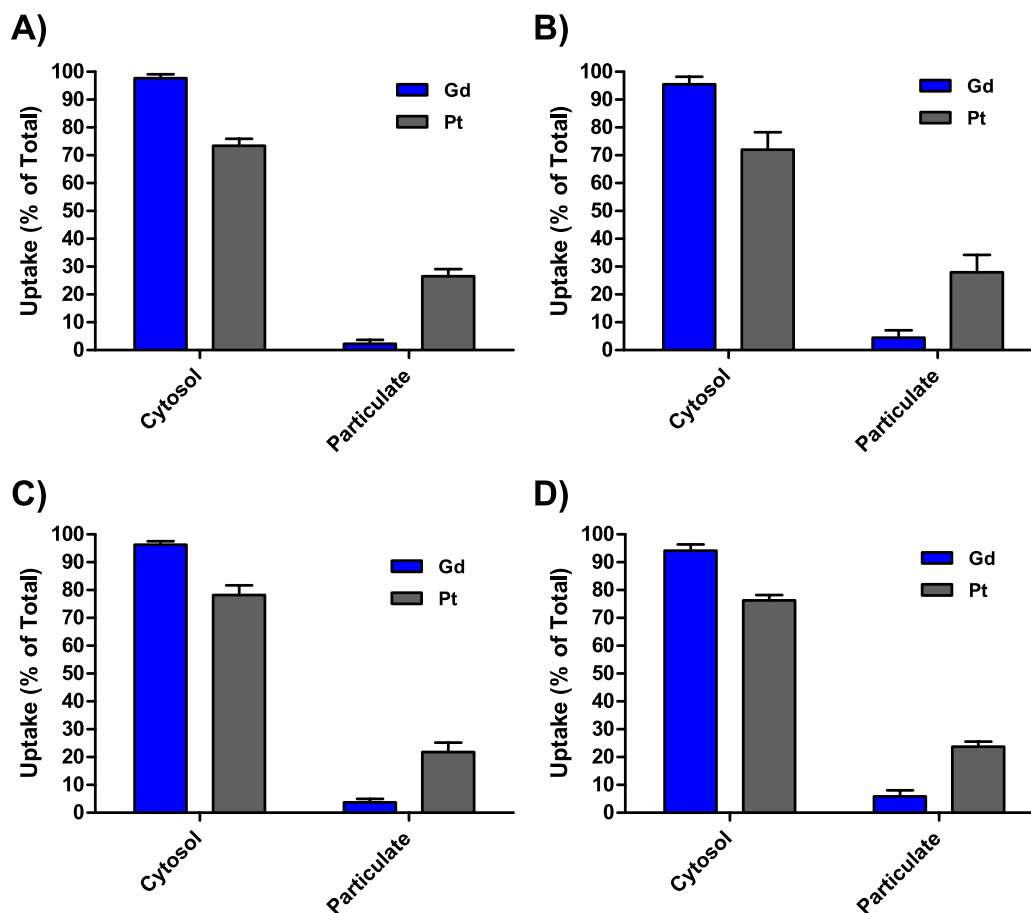
Figure A.2.10 Subcellular localization of Gd and Pt in cytosolic and particulate (membrane, organelles, cytoskeleton) cellular fractions. (A) A2780 cells incubated with 32.5 μM **GP1** for 24 h. (B) HeLa cells incubated with 50 μM **GP1** for 24 h. (C) A2780 cells incubated with 50 μM **GP2** for 24 h. (D) HeLa cells incubated with 250 μM **GP2** for 24 h. In all cases, ≥94% of Gd localized in the cytosol. The majority of Pt localized in the cytosol, but significant amounts were also found in particulate fractions. The differences in subcellular localization between Gd and Pt supports that **GP1** and **GP2** dissociate intracellularly.

APPENDIX 3

SUPPORTING INFORMATION FOR CHAPTER 4

General Methods. Unless otherwise indicated, all reactions were performed under a nitrogen atmosphere in oven-dried glassware. Anhydrous solvents were used in all reactions and obtained from a J.C. Meyer solvent system (Laguna Beach, CA). Thin-layer chromatography (TLC) was performed on EMD 60 F254 silica gel plates. Standard grade 60 Å 230–400 mesh silica gel was used for normal-phase column chromatography. Unless otherwise stated, all silica gel columns were flashed with air. 1H and 13C NMR spectra were obtained on a Bruker 500 MHz Avance III NMR spectrometer. MALDI-MS was performed on a Bruker AutoFlex III, using 2,5-dihydroxybenzoic acid as the matrix. ESI-MS was performed on a Bruker AmaZonSL spectrometer.

Cyclen was obtained from Strem Chemical, while all other reagents were purchased from Sigma Aldrich or Fisher Scientific and used without purification. Analytical HPLC-MS was performed on an Agilent 1260 Infinity II HPLC system with an in-line Agilent 6120 Quad mass spectrometer. Semi-preparative HPLC was performed on an Agilent PrepStar 218 equipped with an Agilent 1260 Infinity diode array detector. HPLC purifications utilized deionized water (18.2 MΩ·cm) obtained from a Millipore Q-Guard System and HPLC grade MeCN, formic acid, and ammonium hydroxide (all obtained from Fisher Scientific). Analytical HPLC used either a Waters Atlantis C18 column (4.6 × 250 mm, 5 µm) or an XBridge C18 column (4.6 × 150 mm, 5 µm). Semipreparative HPLC used either a Waters XBridge C18 column (19 × 250 mm, 10 µm) or a Phenomenex Synergi Polar RP column (21.2 × 150 mm, 4 µm). Compounds were purified using one of the following methods. Method A: MeCN held at 15% for 5 min followed by a 5 min ramp to 35% and a 15 min ramp to 45%. Method B: MeCN held at 0% for 5 min followed by a 2 min ramp to 15% and a 23 min ramp to 35%. Method C: MeCN held at 0% for 5 min followed by a 2

min ramp to 15% and a 33 min ramp to 35%. Method D: MeCN held at 0% for 5 min followed by a 15 min ramp to 50%. Method E: MeCN held at 0% for 5 min followed by a 7 min ramp to 15% and a 23 min ramp to 35%.

Chemical Synthesis. tetra-tert-butyl-2,2',2'',2'''-((((((ethane-1,2-diylbis(oxy))bis(2-(bis(2-(tert-butoxy)-2-oxoethyl)amino)-3,1-phenylene))bis(oxy))bis(propane-3,1-diyl))bis(1,4,7,10-tetraazacyclododecane-4,1,7-triyl))tetraacetate, **7**. 640 mg of bis-t-butyl-DO2A (1.6 mmol) and 308 mg K_2CO_3 (2.24 mmol) were dissolved in 75 mL MeCN. 311 mg of **6** (0.319 mmol) was added and the reaction was stirred at 60 ˚C with a condenser under nitrogen for 24 h, at which point analytical HPLC-MS indicated completion. The crude product was filtered and concentrated for HPLC purification. A semi- preparative Polar RP column and Method A (0.1%) formic acid additive; retention time = 18 min) were used to purify the product as a pale glass in 30% yield. Analytical HPLC-MS traces are found in Figure A.3.1 ESI-MS m/z observed: 807.71, calculated: 807.53 $[M+2H]^{2+}$.

tetra-tert-butyl-2,2',2'',2'''-((((((ethane-1,2-diylbis(oxy))bis(2-(bis(2-(tert-butoxy)-2-oxoethyl)amino)-3,1-phenylene))bis(oxy))bis(propane-3,1-diyl))bis(4-(1-(tert-butoxy)-6-((tert-butoxycarbonyl)amino)-1-oxohexan-2-yl)-1,4,7,10-tetraazacyclododecane-10,1,7-triyl))tetraacetate, **9**. 60 mg of **7** (0.037 mmol) and 51 mg K_2CO_3 (0.37 mmol) were dissolved in 30 mL MeCN. 51 mg of **8** (0.37 mmol) were added and the reaction was stirred at 50 ˚C with a condenser under nitrogen for 48 h, at which point ESI-MS indicated completion. The crude product was filtered and concentrated. Silica gel chromatography with a gradient of 10-15% MeOH in

CH$_2$Cl$_2$ yielded product as a pale oil. ESI-MS m/z observed: 1092.85, calculated: 1092.95 [M+H]$^{2+}$.

2,2',2'',2'''-((((((ethane-1,2-diylbis(oxy))bis(2-(bis(carboxymethyl)amino)-3,1-phenylene))bis(oxy))bis(propane-3,1-diyl))bis(4-(5-amino-1-carboxypentyl)-1,4,7,10-tetraazacyclododecane-10,1,7-triyl))tetraacetate-gadolinium(III), **10**. 42 mg of **9** (.019 mmol) were dissolved in 10 mL of formic acid and the reaction was stirred at 40 ˚C with a condenser under nitrogen for 48 h, at which point analytical HPLC-MS indicated the deprotection was complete. Formic acid was removed in vacuo and the crude product was co-evaporated twice with 10 mL CH$_2$Cl$_2$. A semi-preparative Atlantis C18 column and Method D (0.1% formic acid additive; retention time = 16 min) were used to purify the product as a pale glass in 75% yield (over 2 steps). Analytical HPLC-MS traces are found in Figure A.3.1. ESI-MS m/z observed: 712.36, calculated: 712.37 [M]$^{2+}$.

54 mg of deprotected compound (0.030 mmol) were dissolved in 15 mL H$_2$O and pH was adjusted to 6.5 with dilute NaOH. 41 mg of GdCl$_3$·6H2O (0.150 mmol) were added and the pH readjusted to 6.5. The reaction was stirred at 40 ˚C under nitrogen for 18hrs, at which point MALDI-MS and analytical HPLC-MS indicated metalation was complete. The reaction was adjusted to pH 9 and filtered to remove excess Gd(III) as Gd(OH)$_3$ and lyophilized. **10** was used without further purification in the next step. MALDI-TOF-MS m/z observed: 1777.331, calculated 1777.50 [M+2Na]$^+$.

4,4'-((2E,2'E)-((2E,2'E)-((((((((((((ethane-1,2-diylbis(oxy))bis(2-(bis(carboxymethyl)amino)-3,1-phenylene))bis(oxy))bis(propane-3,1-diyl))bis(4,10-bis(carboxymethyl)-1,4,7,10-tetraazacyclododecane-7,1-diyl))bis(5-carboxypentane-5,1-diyl))bis(azanediyl))bis(carbonothioyl))bis(azanediyl))bis(4,1-phenylene))bis(oxy))bis(3-((E)-2-(3,3-dimethyl-1-(4-sulfonatobutyl)-3H-indol-1-ium-2-yl)vinyl)cyclohex-2-en-2-yl-1-ylidene))bis(ethane-2,1-diylidene))bis(3,3-dimethylindoline-1-yl-2-ylidene))bis(butane-1-sulfonate)-gadolinium(III), **1**. **10** (assumed 0.0043 mmol) was dissolved in 2 mL of 100 mM Na_2CO_3 and 1.6 mL MeCN. 8.3 mg of **5** (0.0086 mmol) was dissolved in 0.4 mL DMSO and added to the reaction mixture. The reaction was stirred under nitrogen for 18 h in the dark. The MeCN was removed in vacuo and the reaction was lyophilized to dryness in the dark for HPLC purification. A semi-preparative X-Bridge C18 column and Method B (0.1% NH_4OH additive; retention time = 22 min) were used to purify the product as a green fluffy solid in 14% yield (over 2 steps) after lyophilization. Analytical HPLC traces (210 and 700 nm λabs) of purified **1** are found in Figure A.3.2. ESI-MS m/z observed: 1727.1, calculated: 1727.02 $[M+2Na]^{2+}$.

tert-butyl-2-bromo-6-((tert-butoxycarbonyl)amino)hexanoate, **8**. 1.5 g Nε-Boc-D-lysine (6.09 mmol) were dissolved in 110 mL CH_2Cl_2 and chilled to 0 ˚C under nitrogen. 1.5 mL Br_2 (30.45 mmol) were added followed by slow addition of isopentyl nitrite over 5 min. The reaction was stirred for 90 min until the starting material had dissolved (indicating reaction of the amine). CH_2Cl_2 and Br_2 were removed in vacuo and the residue co-evaporated twice with CH_2Cl_2. After removal of Br_2, the crude product was taken up in EtOAc and washed (2x) with 0.25 M $Na_2S_2O_3$ followed by 0.1 M HCl (2x). The organic phase was dried over Na_2SO_4 and concentrated. Silica

gel chromatography with a gradient of 7:3-1:1 hexanes/EtOAc yielded the brominated product as a pale yellow oil in 52% yield. 1H NMR (500 MHz, CDCl$_3$) δ 6.35 (br s, 1H), 4.24 (dd, J = 7.2 Hz, 1H), 3.13 (dd, J = 6.4, 0.3, 0.2 Hz, 2H), 2.2-2 (m, 2H), 1.58-1.38 (m, 11H).

To 1.07 g of purified compound (3.44 mmol) in 125 mL CHCl$_3$ were added 2.45 mL *t*-butyl-2,2,2-trichloroacetimidate (13.76 mmol) in 25 mL CHCl$_3$ via a drop-funnel. After 18 h the crude product was concentrated and dry-loaded onto a silica gel column. A gradient of 9:1-5:1 hexanes/EtOAc yielded **8** as a pale yellow oil in 83% yield. 1H NMR (500 MHz, Chloroform-d) δ 4.10 (dd, J = 7.8, 6.8 Hz, 1H), 3.12 (dd, J = 6.7, 6.2 Hz, 3H), 2.14 – 1.86 (m, 2H), 1.48 (s, 9H), 1.46-1.34 (m, 2H), 1.44 (s, 9H).

Triethyl-2,2',2''-(10-(3-(2-(bis(2-ethoxy-2-oxoethyl)amino)-3-(2-(2-(bis(2-ethoxy-2-oxoethyl)amino)-3-(3-bromopropoxy)phenoxy)ethoxy)phenoxy)propyl)-1,4,7,10-tetraazacyclododecane-1,4,7-triyl)triacetate, S2. 802 mg of **S1** (0.93 mmol) and 308 mg K$_2$CO$_3$ (2.23 mmol) were dissolved in 1200 mL MeCN. 488 mg of tris-ethyl DO3A (1.11 mmol) was added and the reaction was stirred at 60 ˚C under nitrogen for 40 h, at which point ESI-MS indicated consumption of the tris-ethyl-DO3A. The crude was filtered and concentrated. Silica gel chromatography (gravity) with a very slow gradient of 2.5-7.5% MeOH in CH$_2$Cl$_2$ yielded product as a pale oil. ESI-MS m/z observed: 1211.66, calculated: 1211.53 [M + H]$^+$.

Diethyl-2,2'-(4-(1-ethoxy-1-oxo-6-(2,2,2-trifluoroacetamido)hexan-2-yl)-1,4,7,10-tetraazacyclododecane-1,7-diyl)diacetate, S3. 1.08g of bis-ethyl-DO2A (3.24 mmol) and 750 mg K$_2$CO$_3$ (5.4 mmol) were dissolved in 150 mL MeCN. 549 mg of trifluoroacetyl-Nε-L-lysine α-bromo ethyl ester (1.8 mmol) were added and the reaction was stirred under nitrogen for 40 h. The

reaction was filtered and concentrated. Silica gel chromatography in 10% MeOH/EA yielded the product as a light brown oil. ESI-MS m/z observed: 598.30, calculated: 598.33 $[M + H]^+$.

Triethyl-2,2',2''-(10-(3-(2-(bis(2-ethoxy-2-oxoethyl)amino)-3-(2-(2-(bis(2-ethoxy-2-oxoethyl)amino)-3-(3-(7-(1-ethoxy-1-oxo-6-(2,2,2-trifluoroacetamido)hexan-2-yl)-4,10-bis(2-ethoxy-2-oxoethyl)-1,4,7,10-tetraazacyclododecan-1-yl)propoxy)phenoxy)ethoxy)phenoxy)propyl)-1,4,7,10-tetraazacyclododecane-1,4,7-triyl)triacetate, S4. 352 mg of **S2** (0.29 mmol), 260 mg of compound **S3** (0.435 mmol), and 120 mg of K_2CO_3 (0.87 mmol) were dissolved in 50 mL MeCN. The reaction was stirred at 70 °C with a condenser under nitrogen for 48 h, at which point ESI-MS indicated compound **2** was largely consumed and the reaction was filtered and concentrated. Silica gel chromatography (gravity) with a very slow gradient of 2.5-15% MeOH in CH_2Cl_2 yielded product as a pale oil. ESI-MS m/z observed: 865.12, calculated: 864.97 $[M + 2H]^{2+}$.

2,2',2''-(10-(3-(3-(2-(3-(3-(7-(5-amino-1-carboxypentyl)-4,10-bis(carboxymethyl)-1,4,7,10-tetraazacyclododecan-1-yl)propoxy)-2-(bis(carboxymethyl)amino)phenoxy)ethoxy)-2-(bis(carboxymethyl)amino)phenoxy)propyl)-1,4,7,10-tetraazacyclododecane-1,4,7-triyl)triacetate-gadolinium(III), S5. 35 mg of **S4** (0.02 mmol) were dissolved in 20 mL THF. 10 mL 1 M NaOH were added and the biphasic reaction mixture was stirred at 35 °C under nitrogen for 18 h, at which point analytical HPLC-MS indicated the deprotection was complete. THF was removed in vacuo and the aqueous crude was neutralized then lyophilized for HPLC purification. A semi-preparative Polar RP column and Method E (0.1% formic acid additive; retention time =

14 min) were used to purify the product as a pale powder after lyophilization in approximately 41% yield (Figure A.3.1.) ESI-MS m/z observed: 1353.4, calculated: 1353.46 $[M + H]^+$.

11 mg of deprotected compound (0.0081 mmol) were dissolved in 15 mL H_2O and the pH was adjusted to 6.5 with 0.1 M NaOH. 10 mg of $GdCl_3 \cdot 6H2O$ (0.024 mmol) were added and the pH readjusted to 6.5. The reaction was stirred at 40 ˚C under nitrogen for 18 h, at which point MALDI-MS and analytical HPLC indicated metalation was complete. The reaction was adjusted to pH 9 and filtered to remove excess Gd(III) as $Gd(OH)_3$ and lyophilized. **S5** was used without further purification in the next step. ESI-MS m/z observed: 848.3, calculated: 848.44 $[M + K]^{2+}$.

(4-((E)-2-((E)-2-(2-(4-(3-(5-(7-(3-(2-(bis(carboxymethyl)amino)-3-(2-(2-(bis(carboxymethyl)amino)-3-(3-(4,7,10-tris(carboxymethyl)-1,4,7,10-tetraazacyclododecan-1-yl)propoxy)phenoxy)ethoxy)phenoxy)propyl)-4,10-bis(carboxymethyl)-1,4,7,10-tetraazacyclododecan-1-yl)-5-carboxypentyl)thioureido)phenoxy)-3-((E)-2-(3,3,4,5-tetramethyl-1-(4-sulfonatobutyl)-3H-pyrrol-1-ium-2-yl)vinyl)cyclohex-2-en-1-ylidene)ethylidene)-3,3-dimethylindolin-1-yl)butane-1-sulfonate)-gadolinium(III), **2**. **S5** (assumed 0.0081 mmol) was dissolved in 2.5 mL of 100 mM Na_2CO_3 and 1.6 mL MeCN. 11 mg of **5** (0.012 mmol) was dissolved in 0.5 mL DMSO and added to the reaction mixture. The reaction was stirred under nitrogen for 24 h in the dark. The MeCN was removed in vacuo and the reaction was lyophilized to dryness in the dark for HPLC purification. A semi-preparative X-Bridge C18 column and Method C (0.1% NH4OH additive; retention time = 17 min) were used to purify the product as a green fluffy solid in 17% yield (over 2 steps) after lyophilization. Analytical HPLC traces (210

and 700 nm λabs) of purified **2** are found in Figure A.3.2. ESI-MS m/z observed: 832.8, calculated: 832.90 $[M + H]^{3+}$.

Triethyl-2,2',2''-(10-(3-(3-(2-(3-(3-azidopropoxy)-2-(bis(2-ethoxy-2-oxoethyl)amino)phenoxy)ethoxy)-2-(bis(2-ethoxy-2-oxoethyl)amino)phenoxy)propyl)-1,4,7,10-tetraazacyclododecane-1,4,7-triyl)triacetate, S6. 490 mg of compound **S2** (0.404 mmol) were dissolved in 50 mL DMF. 525 mg NaN_3 (8.08 mmol) were added and the reaction was stirred at 70 °C under nitrogen for 18 h, at which point ESI-MS indicated complete conversion of the starting material. The reaction was filtered and the DMF removed in vacuo. The crude residue was taken up in $CH_2Cl_2/H2O$ and extracted into CH_2Cl_2 (3x). The combined organic phases were dried over Na_2SO_4 and concentrated. ESI-MS m/z observed: 1174.76, calculated: 1174.62 $[M + H]^+$.

2,2',2''-(10-(3-(3-(2-(3-(3-aminopropoxy)-2-(bis(carboxymethyl)amino)phenoxy)ethoxy)-2-(bis(carboxymethyl)amino)phenoxy)propyl)-1,4,7,10-tetraazacyclododecane-1,4,7-triyl)triacetate-gadolinium(III), S7. **S6** (assumed 0.4 mmol) was dissolved in 50 mL THF. 25 mL 1M NaOH were added and the biphasic reaction mixture was stirred at 35 °C under nitrogen for 24 h, at which point MALDI-MS indicated complete deprotection. THF was removed in vacuo and the residual aqueous mixture adjusted to pH 6.5 with 4M HCl. The crude was carried through without further purification. ESI-MS m/z observed: 978.65, calculated: 978.44 $[M + H]^+$.

450 mg $GdCl_3·H2O$ was added to the aqueous mixture containing the deprotected intermediate. The pH was readjusted to 6.5 with 0.1 M NaOH and 200 mg Pd/C was added. The flask was sealed with a septum and flushed with H_2. The reaction mixture was stirred 18 h, at

which point analytical HPLC indicated product had been formed. The reaction was adjusted to pH 8.5 with NaOH to precipitate residual Gd(III) as Gd(OH)$_3$, filtered, and lyophilized for HPLC purification. A semi-preparative Polar RP column and Method D (0.1% formic acid additive; retention time = 18 min) were used to purify **S7** as a pale powder after lyophilization in 18% yield (over three steps). ESI-MS m/z observed: 1107.2, calculated: 1107.18 [M+H]$^+$. (Figure A.3.1.)

(4-((E)-2-((E)-2-(2-(4-(3-(3-(2-(bis(carboxymethyl)amino)-3-(2-(2-(bis(carboxymethyl)amino)-3-(3-(4,7,10-tris(carboxymethyl)-1,4,7,10-tetraazacyclododecan-1-yl)propoxy)phenoxy)ethoxy)phenoxy)propyl)thioureido)phenoxy)-3-((E)-2-(3,3-dimethyl-1-(4-sulfonatobutyl)-3H-indol-1-ium-2-yl)vinyl)cyclohex-2-en-1-ylidene)ethylidene)-3,3-dimethylindolin-1-yl)butane-1-sulfonate)-gadolinium(III), **3**. 161 mg of **S7** (0.07 mmol) was dissolved in 5 mL of 100 mM Na$_2$CO$_3$ and 4 mL MeCN. 15 mg **5** (0.018 mmol) was dissolved in 1 mL DMSO and added to the reaction mixture. The reaction was stirred under nitrogen for 18 h in the dark. The MeCN was removed in vacuo and the reaction was lyophilized to dryness in the dark for HPLC purification. A semi-preparative X-Bridge C18 column and Method C (0.1% NH$_4$OH additive; retention time = 18 min) were used to purify the product as a green fluffy solid in 4% yield. Analytical HPLC traces (210 and 700 nm λabs) of purified **3** are found in Figure A.3.2. ESI-MS m/z observed: 974.3, calculated: 974.29 [M+H]$^{2+}$.

(4-((E)-2-((E)-2-(2-(4-(3-(5-(7-(3-(3-(2-(3-(3-(7-(5-amino-1-carboxypentyl)-4,10-bis(carboxymethyl)-1,4,7,10-tetraazacyclododecan-1-yl)propoxy)-2-(bis(carboxymethyl)amino)phenoxy)ethoxy)-2-(bis(carboxymethyl)amino)phenoxy)propyl)-4,10-

bis(carboxymethyl)-1,4,7,10-tetraazacyclododecan-1-yl)-5-carboxypentyl)thioureido)phenoxy)-3-((E)-2-(3,3-dimethyl-1-(4-sulfonatobutyl)-3H-indol-1-ium-2-yl)vinyl)cyclohex-2-en-1-ylidene)ethylidene)-3,3-dimethylindolin-1-yl)butane-1-sulfonate)-gadolinium(III), **4**. **10** (0.033 mmol) was dissolved in 5 mL of 100 mM Na_2CO_3 and 4 mL MeCN. 22 mg **5** (0.0264 mmol) was dissolved in 1 mL DMSO and added to the reaction mixture. The reaction was stirred under nitrogen for 18 h in the dark. The MeCN was removed in vacuo and the reaction was lyophilized to dryness in the dark for HPLC purification. A semi-preparative X-Bridge C18 column and Method C (1% NH_4OH additive; retention time = 18.5 min) was used to purify the product as a green fluffy solid in 3% yield (over 2 steps). Analytical HPLC traces (210 and 700 nm λabs) of purified **4** are shown in Figure A.3.2. ESI-MS m/z observed: 858.8, calculated: 858.03 $[M+H]^{3+}$.

Relaxation Time Measurements at 1.41T. 1 was dissolved in 800 μL of pH 7.40 0.1 M HEPES buffer with 0.1 M KCl, 1% DMSO, and 5% Tween 80. The solution was serially diluted to make 4 solutions of varying agent concentration for T_1 acquisition. Relaxation times were measured on a Bruker mq60 NMR analyzer equipped with Minispec v 2.51 Rev.00/NT software (Bruker Biospin, Billerica, MA, USA) operating at 1.41 T (60MHz) and 37 °C. Measurements were made using an inversion recovery pulse sequence (T_1_ir_mb) using the following parameters: 4 scans per point, 10 data points, monoexponential curve fitting, phase cycling, 10 ms first pulse separation, and a recycle delay and final pulse separation ≥ 5 T_1. 10 μL aliquots of each solution were taken for ICP-MS analysis to determine the concentration of Gd(III). Aqueous $CaCl_2$ was added such that each solution had a Ca(II) concentration of 100 μM. T_1 measurements of each solution were taken in the presence of Ca(II) and 10 μL aliquots were taken for ICP-MS analysis.

MR Imaging of Solutions at 7 T. 1 was dissolved in 100 μL of pH 7.40 0.1 M HEPES with 0.1 M KCl, 1% DMSO, and 5% Tween 80. The solution was serially diluted to make 3 solutions of varying agent concentration. 30 μL of each solution were added to flame-sealed 9" Pasteur pipettes. The tips of the pipettes were scored below the meniscus and separated to make small capillaries containing the solutions. These capillaries were sealed with parafilm and imaged using a Bruker PharmaScan 7 T MR imaging spectrometer (Bruker BioSpin, Billerica, MA, USA). T_1 relaxation times were measured using a rapid-acquisition rapid-echo (RARE-VTR) T_1-map pulse sequence with static T_E (10 ms) and variable T_R (100, 200, 400, 500, 750, 1000, 2500, 7500, and 1000 ms) values. Imaging parameters were as follows: field of view (FOV) = 25 x 25 mm^2, matrix size (MTX) = 256 x 256, number of axial slices = 5, slice thickness (SI) = 1.0 mm, and averages (NEX) = 4. T_1 analysis was carried out using the image sequence analysis tool in Paravision 5.0 pl2 software (Bruker, Billerica, MA, USA) with monoexponential curve-fitting of image intensities of selected regions of interest (ROIs) for each axial slice.

Cell Line and Culture. HT-22 hippocampal neuronal cells were obtained from Professor Schubert at Salk Institute (LaJolla, CA) and were cultured using phenol red free DMEM supplemented with 10% FBS. U-87 MG cells were purchased from ATCC and cultured using phenol red free MEM supplemented with 10% FBS. Cells were grown in a humidified incubator at 37 °C and 5% CO_2 and were harvested using 0.25% TrypLE. Cells were grown for 24 hours after plating before all experiments. All solutions were filtered through 0.2 μm sterile filters before use with cells.

Cellular Viability. HT-22 and U-87 MG cells were plated at a density of 6,000 cells per well (100 μL) on an opaque white 96-well plate. Cells were incubated with 50 μL of **1** in media with 0.5% DMSO at concentrations ranging from 0-100 μM. After 24 hours of incubation, 50 μL of CellTiter-Glo 2.0 (Promega, Madison, WI) was added to each of the wells and the assay was carried out following the manufacturer's protocol. Luminescence of the wells was measured using a Synergy H1 microplate reader (BioTek, Winooski, VT). Viability was determined by comparing luminescence of the cells incubated with agent to those incubated with vehicle (DMEM, 0.5% DMSO).

Concentration-dependent Cellular Uptake. HT-22 and U-87 MG cells were plated at a density of 40,000 cells per well (500 μL) on a 24-well plate. Cells were incubated with 300 μL of **1** in media with 0.5% DMSO at concentrations ranging from 0-20 μM. After 24 hours, the media was aspirated and the cells were washed twice with 500 μL of DPBS, harvested, and centrifuged twice at 500g for 5 minutes at 4° C. The media was aspirated and the cells were resuspended in 200 μL of media. A 40 μL aliquot was taken for cell counting using a Guava PCA system using the Guava Viacount protocol provided by the manufacturer. An additional 100 μL aliquot was used for ICP-MS analysis of Gd(III) in the cells.

Cell fractionation experiments were performed using a cytosol/particulate rapid separation kit (BioVision, Milpitas, CA). Uptake experiments were performed in the same way, following the manufacturer's protocol after the first centrifugation. Gd(III) content in each fraction was determined by ICP-MS and the total Gd(III) uptake for a given set of cells was taken to be the sum of the cytosol and particulate fractions.

Time-dependent Cellular Uptake. HT-22 cells were plated at a density of 40,000 cells per well (500 μL) on a 24-well plate. Cells were incubated with 300 μL of 10 μM **1** in media with 0.5% DMSO for variable amounts of time (0.5, 1, 2, 3, 6, 24 h). At each timepoint, the media was aspirated and the cells were washed twice with 500 μL of DPBS, harvested, and centrifuged twice at 500g for 5 minutes at 4°C. The media was aspirated and the cells were resuspended in 200 μL of media. A 40 μL aliquot was taken for cell counting using a Guava PCA system using the Guava Viacount protocol provided by the manufacturer. An additional 100 μL aliquot was used for ICP-MS analysis of Gd(III) in the cells.

Cellular Retention of Gd(III). HT-22 cells were plated at a density of 40,000 cells per well (300 μL) on a 24-well plate. Cells were incubated with 300 μL of 10 μM **1** in media with 0.5% DMSO. After 24 hours, the media was aspirated and the cells were washed twice with DPBS. 300 μL of fresh media was added to the cells and the agent was allowed to leach for 0, 3, 6, 12, and 24 hours. At these time points, 200 μL of media was collected for ICP-MS analysis of Gd(III) content. Additionally, cells at the 0 time point were harvested for counting using a Guava PCA system and analysis by ICP-MS to ensure adequate initial uptake of the agent. Cellular retention was determined by comparing the amount of leached Gd(III) in the media at the various time points to the 0 time point.

MR Imaging of Cell Pellets at 7 T. HT-22 cells were grown to ~60% confluency in T-75 flasks. Cells treated with agent were incubated with 5 mL of 10 μM **1** or **S1** in media with 0.5% DMSO while control cells were incubated with 5 mL of media containing 0.5% DMSO. After incubation, the media was aspirated and the cells were washed twice with 5 mL of DPBS, harvested, and centrifuged twice at 500g for 5 minutes at 4 °C. The cells were suspended in 1 mL of pH 7.40 0.1 M HEPES buffer with 0.1 M KCl and 2 mM $CaCl_2$ (with either 10 or 0 μM calcimycin), and 950 μL of the suspension was added to 5 ¾" flame-sealed Pasteur pipettes while the rest was used for cell counting and ICP-MS. The pipettes were centrifuged at 200g for 5 minutes at 4° C and were separated to form small capillaries containing the cell pellets. The capillaries were imaged using a Bruker PharmaScan 7 T MR imaging spectrometer following the same imaging protocol previously described.

Two-photon Confocal Microscopy. HT-22 cells were plated at a density of 50,000 cells on a 35 mm FluoroDish (World Precision Instruments, Sarasota, FL). The cells were incubated with 10 μM **1** in media with 0.5% DMSO for 24 hours. After incubation with the agent, the media was aspirated, the cells were washed three times with 1 mL of DPBS, and 1 mL of fresh media was added. The cells were imaged using a Zeiss LSM 510 confocal laser scanning inverted microscope with a mode-locked Mai Tai DeepSee Ti:sapphire two-photon laser (Spectra Physics, Mountain View, CA) at an excitation wavelength of 780 nm. All images were acquired using a Plan-Appochromat 40x/1.20NA water immersion Korr UV-vis-IR M27 objective lens.

***In Vitro* IVIS Imaging.** Plated HT-22 cells used for confocal microscopy and cell pellets used for MR imaging were additionally imaged using an IVIS Spectrum Imaging System (PerkinElmer, Waltham, MA). An excitation wavelength of 745 nm and emission wavelength of 810 nm was used.

Cell Counting with a Guava EasyCyte Mini Personal Cell Analyzer (PCA) System. Aliquots of cell suspensions were mixed with the Guava ViaCount Reagent and allowed to stain for 5 minutes. The samples were vortexed for 20 seconds and cell count was determined via manual analysis using a Guava EasyCyte Mini PCA and ViaCount software. 1000 events were acquired for each sample and dilutions were performed to assure the cell count was in the optimal range for instrument performance (10-100 cells/μL). Performance of the instrument was assessed daily using Guava-Check Beads and the manufacturer's protocol and Daily Check software.

Quantification of Gd(III) with Inductively Coupled Plasma Mass Spectrometry. Gd(III) content was quantified through ICP-MS analysis of acid digested samples. Samples were digested in 300 μL of ACS reagent grade nitric acid (70%, Sigma, St. Louis, MO) for 3 hours in a 70 °C water bath. After digestion, the volume was diluted up to 10 mL with Milli-Q water. ICP-MS was performed on a computer-controlled (Plasma-lab software) Thermo X series II ICP-MS (Thermo Fisher Scientific, Waltham, MA) operating in standard mode equipped with an ESI SC-2 autosampler (Omaha, NE). Each sample was acquired using 1 survey run and 3 main runs. ^{157}Gd and ^{158}Gd were selected for analysis with ^{115}In and ^{165}Ho as internal standards.
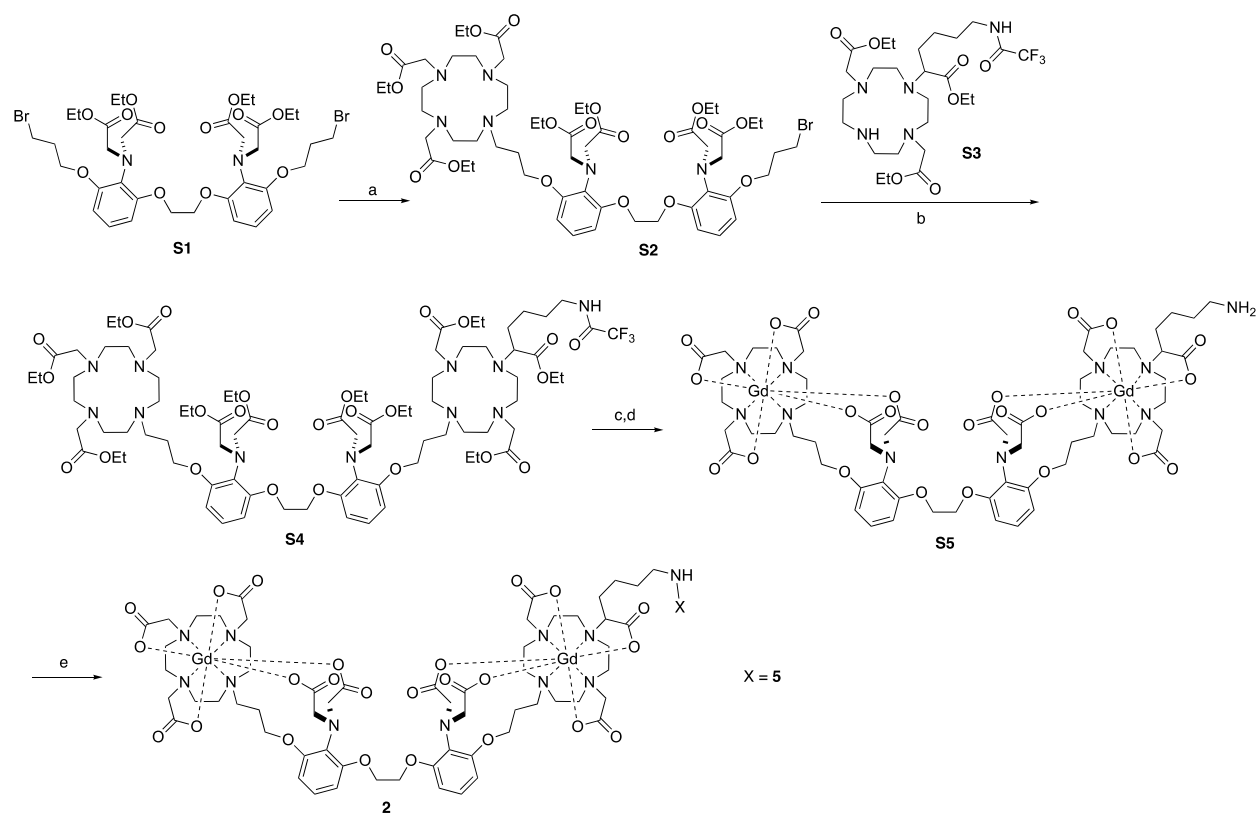
Scheme A.3.1. Synthetic Scheme of 2. (a) Tris-ethyl DO3A, K_2CO_3, MeCN, 60 °C, 43%. (b) **S3**, K_2CO_3, MeCN, 70 °C, 7%. (c) 1 M NaOH, THF, 35 °C, 41%. (d) $GdCl_3$, NaOH, pH 5-6.5, 40 °C. (e) **5**, DMSO/MeCN/100 mM Na_2CO_3.
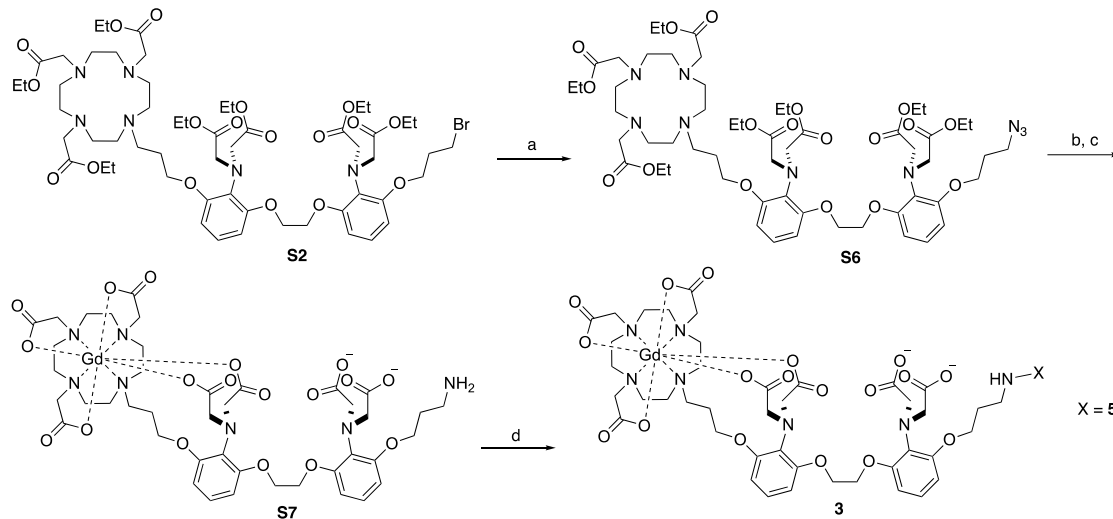
Scheme A.3.2. Synthetic scheme of 3. (a) NaN$_3$, DMF, 70 °C. (b) 1 M NaOH, THF, 35 °C. (c) GdCl$_3$, NaOH, pH 5-6.5, Pd/C, H$_2$. (d) **5**, DMSO/MeCN/100 mM Na$_2$CO$_3$.
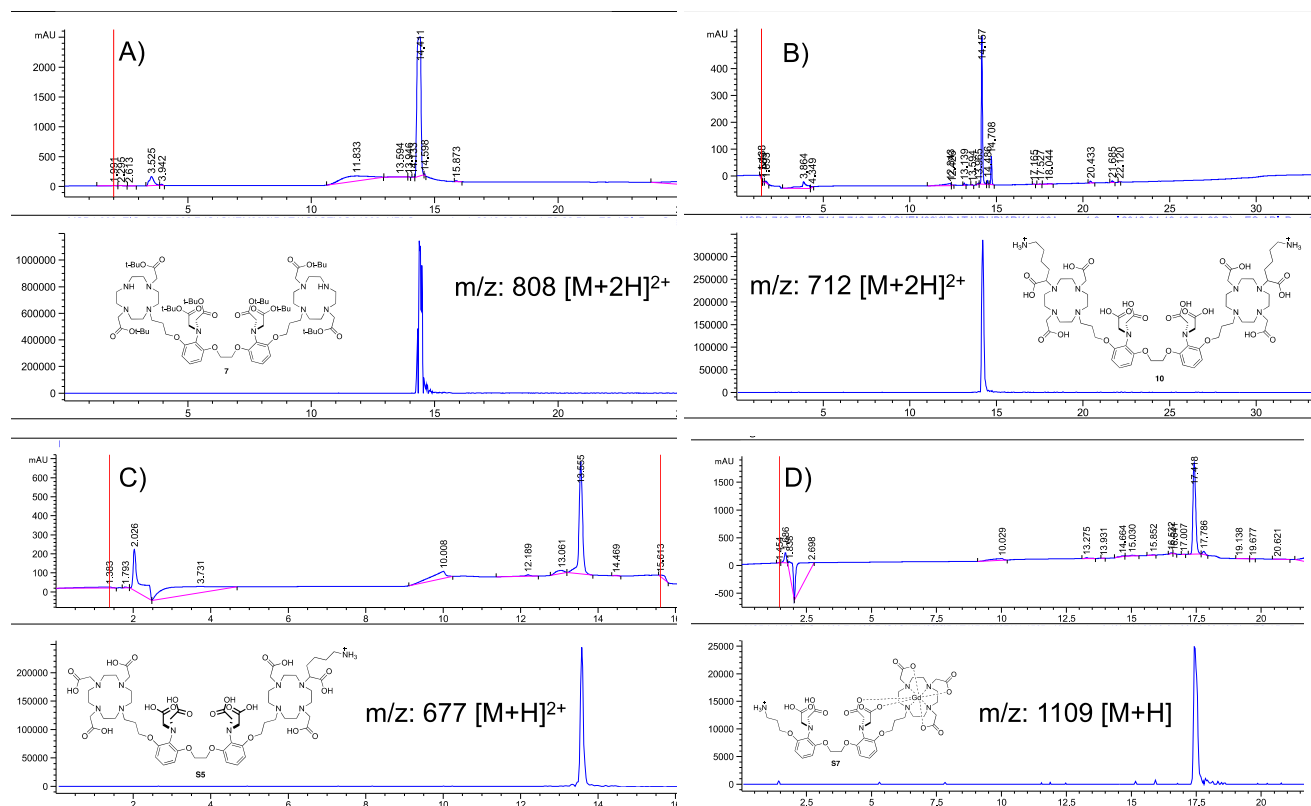
Figure A.3.1. Analytical HPLC traces of intermediate compounds **7** (A), unmetalated **10** (B), unmetalated **S5** (C), and **S7** (D) with the corresponding product mass extractions.
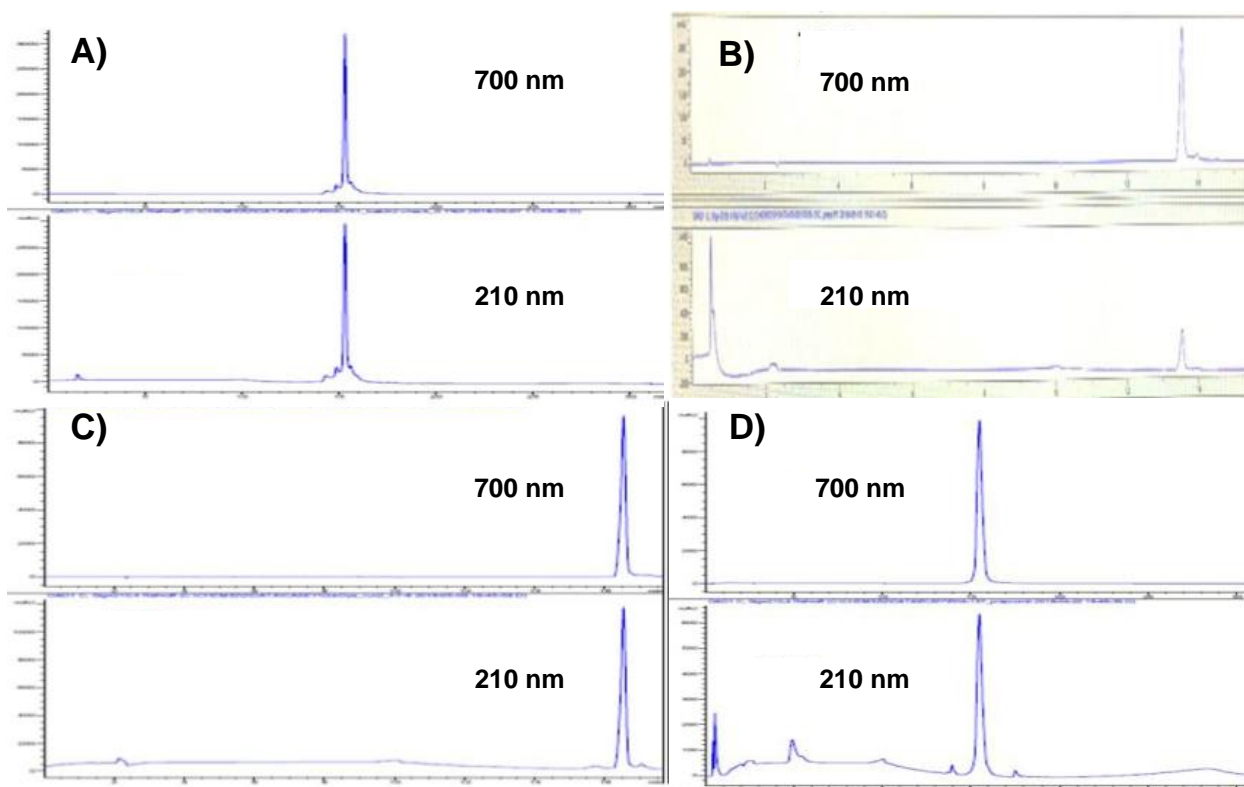
Figure A.3.2. Analytical HPLC traces of purified final compounds **1** (A), **2** (B), **3** (C), and **4** (D) using 210 nm and 700 nm UV-vis channels. Each analytical trace shows one species that absorbs at 210 nm and 700 nm, indicating IR-783 was attached and each compound was successfully purified. These traces along with MS data indicate the purity and identity of final compounds **1**-**4**.
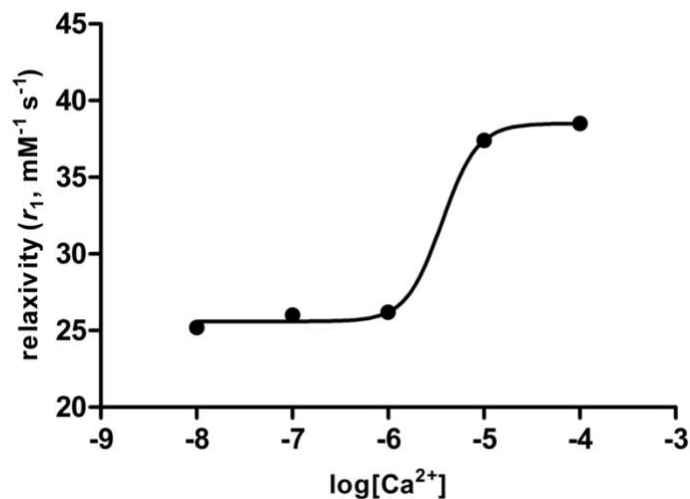
Figure A.3.3. Relaxivity (r_1) at 1.41 T of **1** upon addition of $CaCl_2$ in pH 7.40 0.1 M HEPES buffer with 0.1 M KCl, 1% DMSO, and 5% Tween 80 at 37 °C. For each data point, Ca(II) response was measured at 0, 0.4 and 0.8 mM **1**. The r_1 of **1** increases in response to Ca(II) in the range of 1-10 µM, with an EC50 of 3.6 µM and is therefore activated at biologically relevant concentrations of Ca(II).
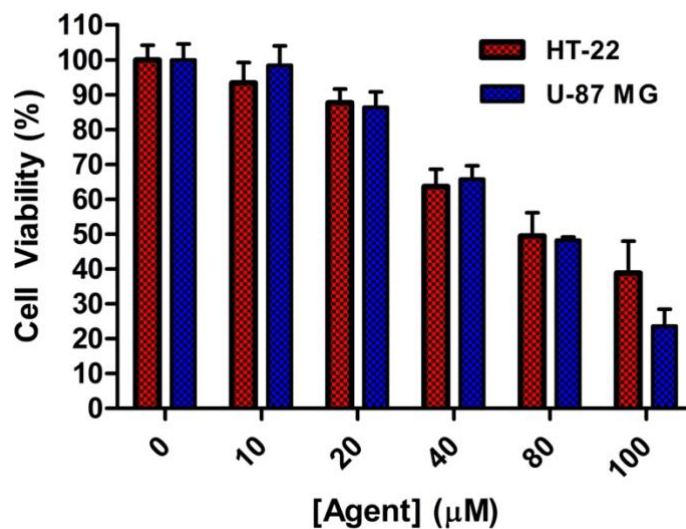
Figure A.3.4. Viability of HT-22 and U-87 MG cells incubated with **1** for 24 h. Data are presented as the average ± one standard deviation of at least three assays. **1** is well tolerated in both cell lines up to 20 µM.
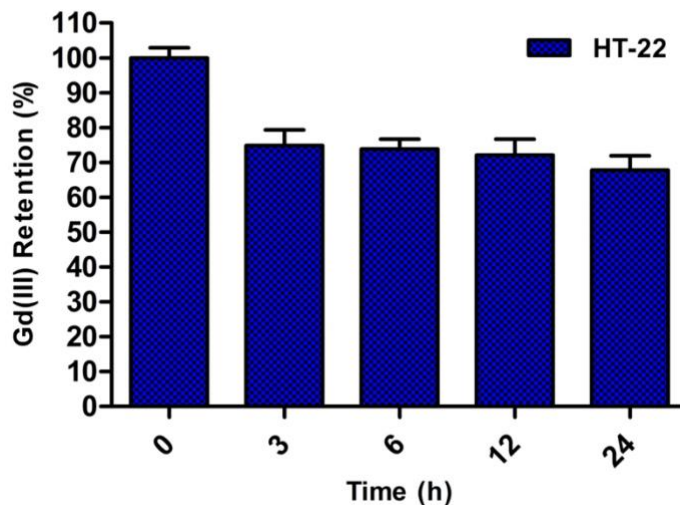
Figure A.3.5. Time-dependent leaching of Gd(III) in HT-22 cells over 24 h after incubation with 10 μM **1** for 24 h. Data are the mean ± one standard deviation of three runs.

	Control	Control + calcimycin	1	1 + calcimycin
T_1 (ms):	2051 ± 15	2066 ± 17	987 ± 12	925 ± 13
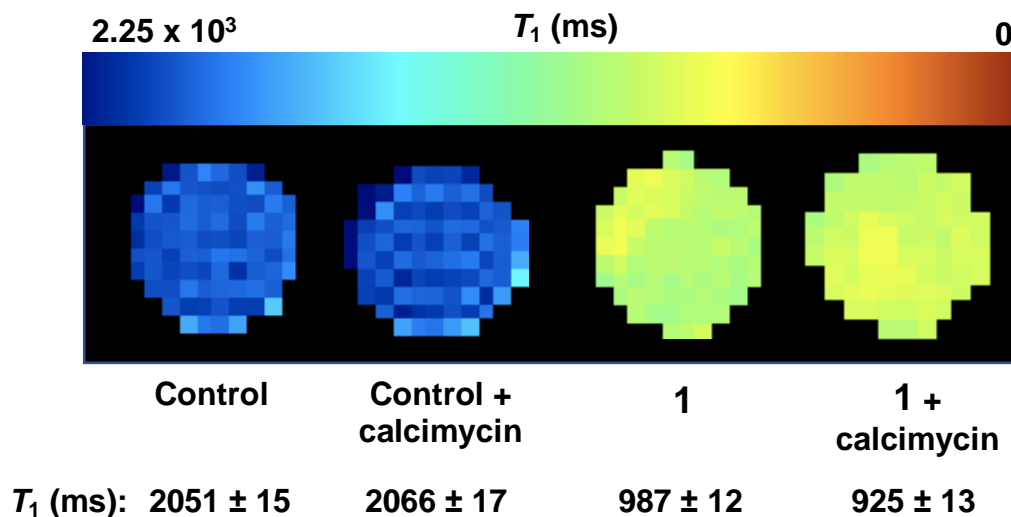
Figure A.3.6. T_1 map of untreated HT-22 cells (control), control cells treated with 10 μM calcimycin, cells incubated with 10 μM **1** for 24 h, and cells incubated with 10 μM **1** for 24 h treated with 10 μM calcimycin. Control cells treated with calcimycin did not have a significant change in T_1; however, cells incubated with **1** for 24 h showed a drastic decrease in T_1 and cells incubated with **1** that were treated with calcimycin had a significant decrease in T_1 ($p < 0.01$) compared to cells incubated with **1** that were not treated with calcimycin.
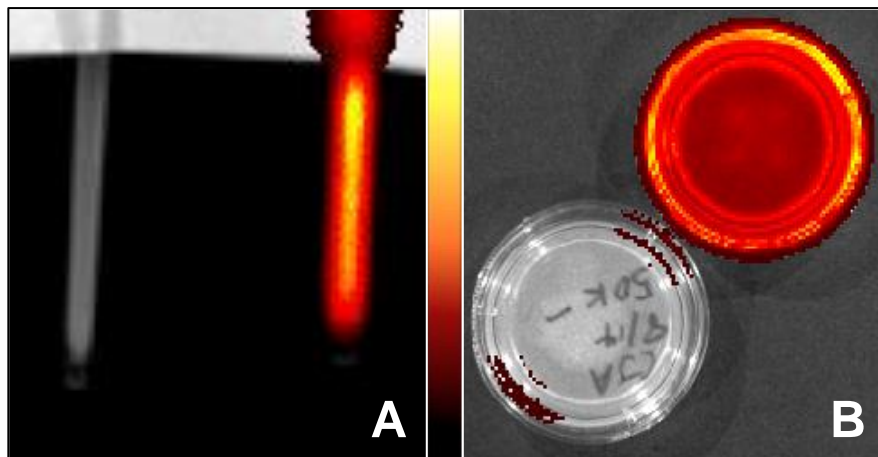
Figure A.3.7. IVIS imaging of HT-22 cells untreated (control) and incubated with 10 μM **1** for 24 h. A) IVIS images of the same HT-22 cell pellet capillaries used for *in vitro* MR imaging. B) IVIS images of the same HT-22 cells used for confocal microscopy. In both A and B, the controls (left) show no fluorescence while cells treated with **1** (right) show fluorescence. In both cases the excitation and emission wavelengths were 745 and 810 nm respectively.
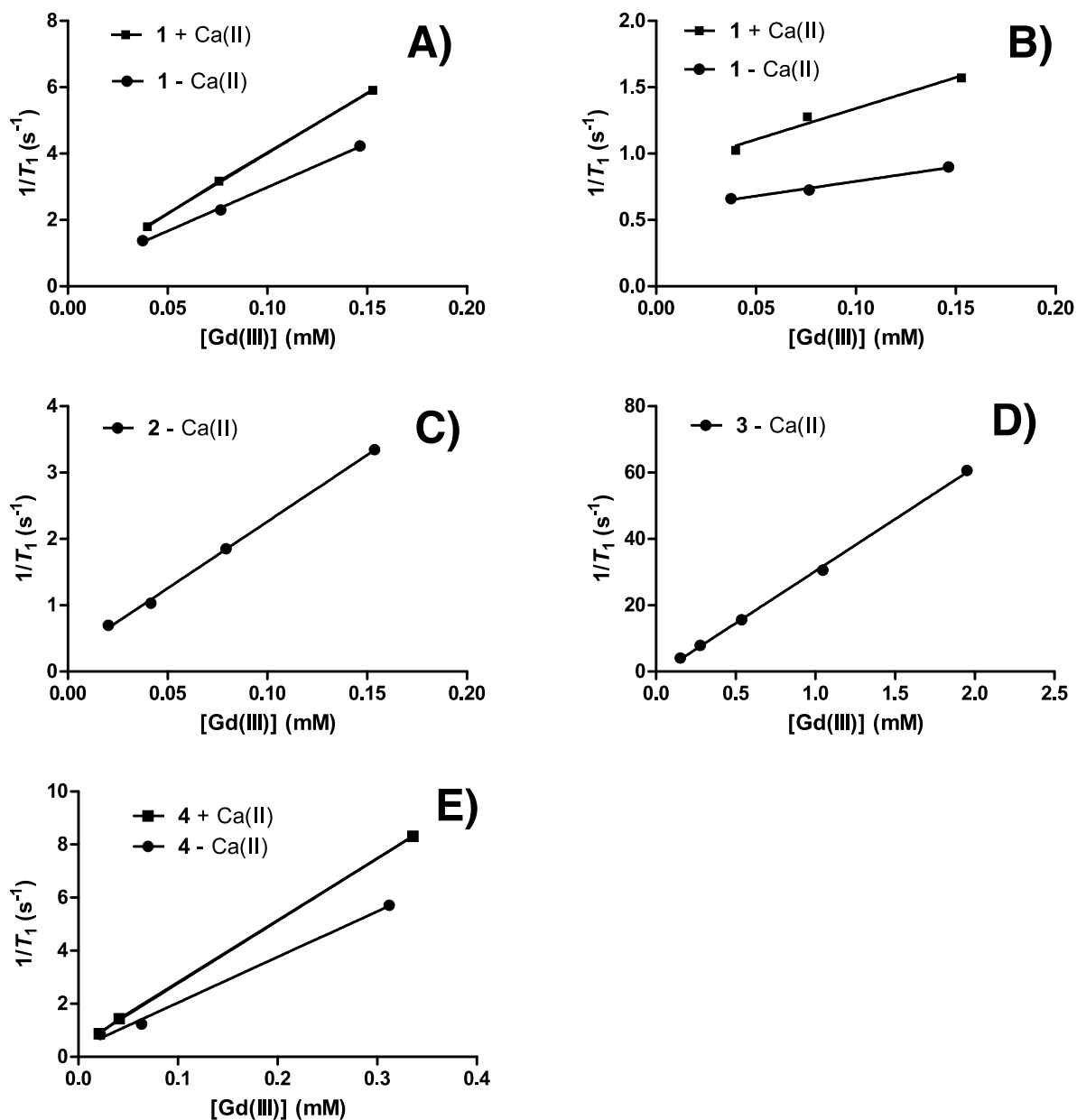
Figure A.3.8. T_1 relaxivity (r_1) graphs of **1** at 1.41 T with and without 0.1 mM Ca(II) (A), **1** at 7 T with and without 0.1 mM Ca(II) (B), **2** at 1.41 T in the absence of Ca(II) (C), **3** at 1.41 T in the absence of Ca(II) (D), and **4** at 1.41 T with and without 0.1 mM Ca(II) (E). All measurements were made in pH 7.40 100 mM HEPES buffer with 100 mM KCl, 1% DMSO and 5% Tween 80 at 37 °C. The r_1 values reported in Table A.3.1 were found by determining the slope of each line.
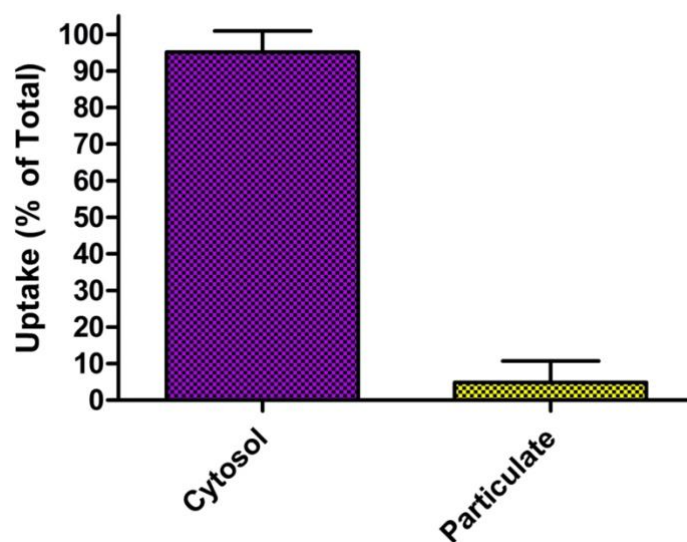
Figure A.3.9. Uptake of **1** in cytosolic and particulate (non-cytosolic components) subcellular fractions of HT-22 cells. Cells were incubated with 10 μM **1** for 24 h. The data is expressed as % of Gd(III) in each subcellular fraction relative to the total Gd(III) uptake. 95% of Gd(III) was found in the cytosol whereas 5% was in other subcellular locations.

A) S8

B)

	Control	S8 (-)	S8 (+)
T_1 (ms):	2282 ± 26	1606 ± 21	1669 ± 27

C)
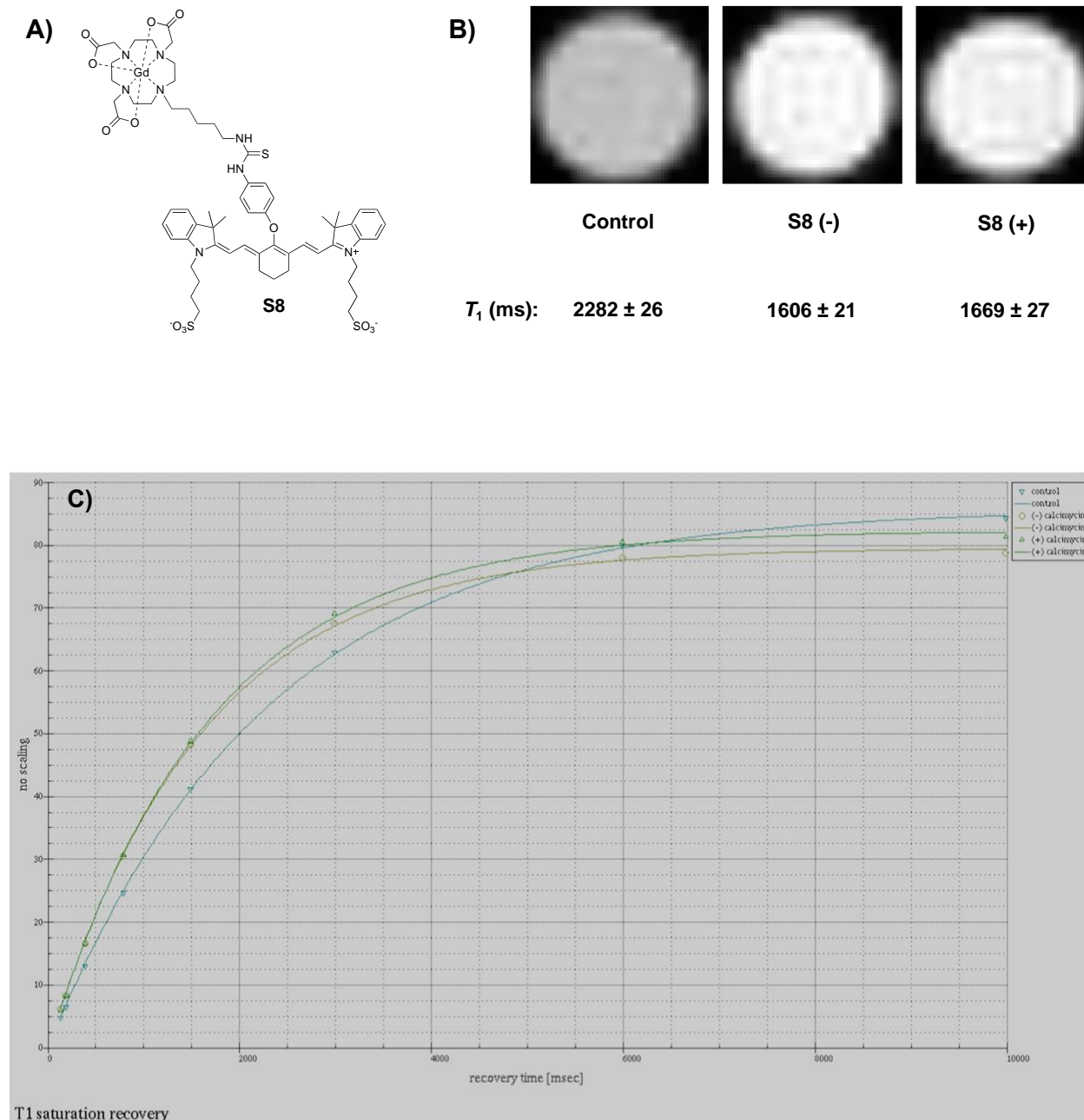
Figure A.3.10. Cell pellet MR imaging at 7 T of HT-22 cells incubated with Ca(II)-insensitive analogue, **S8**. A) Structure of agent **S8**. B) MR images of untreated HT-22 cells (control), cells incubated with 10 μM **S8** for 24 h, and cells incubated with 10 μM **S8** that were then treated with 10 μM calcimycin. All cells incubated with **S8** had shorter T_1 relaxation times compared to control. Cells incubated with **S8** that were treated with calcimycin had a longer T_1 than those that were not treated with calcimycin. C) T_1 fits of cell pellets imaged at 7 T.

Table A.3.1. T_1 relaxivity (r_1) of complexes 2-4 at 1.41 T with and without Ca(II).

Complex	r_1 (1.41 T)		r_1 (1.41 T, 100 μM Ca(II))	
	ionic (mM^{-1} s^{-1})	Molecular (mM^{-1} s^{-1})	ionic (mM^{-1} s^{-1})	Molecular (mM^{-1} s^{-1})
2	20.1 ± 0.5	40.2 ± 1.0	-	-
3	31.4 ± 0.6	31.4 ± 0.6	-	-
4	17.2 ± 1.0	34.4 ± 2.0	23.5 ± 0.3	47.0 ± 0.6

All values reported were measured in pH 7.40 0.1 M HEPES buffer with 100 mM KCl, 1% DMSO and 5% Tween 80 at 37 °C

Table A.3.2. T_2 relaxivity (r_2) of complex 1 at low (1.41 T) and high (7 T) magnetic field strength with and without Ca(II).

Complex	r_2 (1.41 T)		r_2 (1.41 T, 100 μM Ca(II))		r_2 (7 T)		r_2 (7 T, 100 μM Ca(II))	
	ionic (mM^{-1} s^{-1})	Molecular (mM^{-1} s^{-1})	ionic (mM^{-1} s^{-1})	Molecular (mM^{-1} s^{-1})	ionic (mM^{-1} s^{-1})	Molecular (mM^{-1} s^{-1})	ionic (mM^{-1} s^{-1})	Molecular (mM^{-1} s^{-1})
1	44.3	88.6	60.9	121.8	57.7	115.4	84.0	168.0

All values reported were measured in pH 7.40 0.1 M HEPES buffer with 0.1 M KCl, 1% DMSO and 5% Tween 80 at 37 °C.

Table A.3.3. T_2 relaxivity (r_2) of complexes 2-4 at 1.41 T with and without Ca(II).

Complex	r_2 (1.41 T)		r_2 (1.41 T, 100 µM Ca(II))	
	ionic (mM^{-1} s^{-1})	Molecular (mM^{-1} s^{-1})	ionic (mM^{-1} s^{-1})	Molecular (mM^{-1} s^{-1})
2	27.2	54.4	-	-
3	47.7	95.4	-	-
4	24.0	48.0	34.5	69.0

All values reported were measured in pH 7.40 0.1 M HEPES buffer with 100 mM KCl, 1% DMSO and 5% Tween 80 at 37 °C

APPENDIX 4

DEVELOPMENT OF Mn(III/II)-Pt(IV/II) THERANOSTIC AGENTS FOR TURN-ON MR CONTRAST ENHANCEMENT AND CHEMOTHERAPY

A.4.1 Introduction

Though Gd(III) is the most common paramagnetic ion used in T_1 MR contrast agents, it is not the only possible choice. As previously mentioned in Chapter 1, there is a growing body of research into utilizing Mn(II), Fe(III), and even Eu(II) as T_1 MR contrast agents.[1-8] The first two transition metals in that list, Mn and Fe, are biologically relevant, and therefore many researchers advertise them as a potential safer alternative to Gd(III). They suggest that if some of the Mn(II) or Fe(III) dissociates, the body has natural mechanisms to utilize or clear them.

Other than potential safety advantages, Mn(II) and Fe(III) have an attractive quality over Gd(III): interesting redox chemistry. Because of the stability associated with its half filled 4f subshell, Gd(III) is the only oxidation state under reasonable conditions. On the other hand, Mn and Fe (especially Mn) have a variety of accessible oxidation states, some of which are useful for paramagnetic relaxation enhancement in MRI and some of which are not. This opens the door for the ability to develop redox mediated MR contrast agents. For example, Mn(II) and Fe(III) (high spin) are both $S=5/2$ (5 unpaired electrons) and have T_{1e} around the same order of magnitude as Gd(III) ($\sim 10^{-8}$-10^{-10} s), making them effective at PRE. However, Mn(III) and Fe(II) (high spin) are both $S=2$ (less paramagnetic) and have T_{1e} several orders of magnitude faster ($\sim 10^{-11}$-10^{-13} s). The redox potential of these metal ions and electronic properties (such as T_{1e}) are significantly affected by the ligand used, therefore the ligand can be designed to tune the redox potential into a biologically relevant window.

The Caravan Lab has performed a significant amount of research into using Mn(II) as a MR contrast agent, and they have designed a series of ligands suitable for redox active Mn(II/III) agents.[2,9] One such ligand (termed Mn-HBET) has the ability to stably coordinate Mn(II) and

Mn(III) and has a redox potential (0.356 V) in the biological window (Figure A.4.1.)[2] They demonstrated that Mn(III)-HBET has a low relaxivity of ~1.2 $mM^{-1}s^{-1}$, whereas Mn(II)-HBET has a significantly higher relaxivity of ~4 $mM^{-1}s^{-1}$, an impressive turn-on response of >300%. Notably, the relaxivity of Mn(II)-HBET is similar to clinically used GBCAs.[2]

Mn-HBET

$E_{III/II} = 0.356$ V
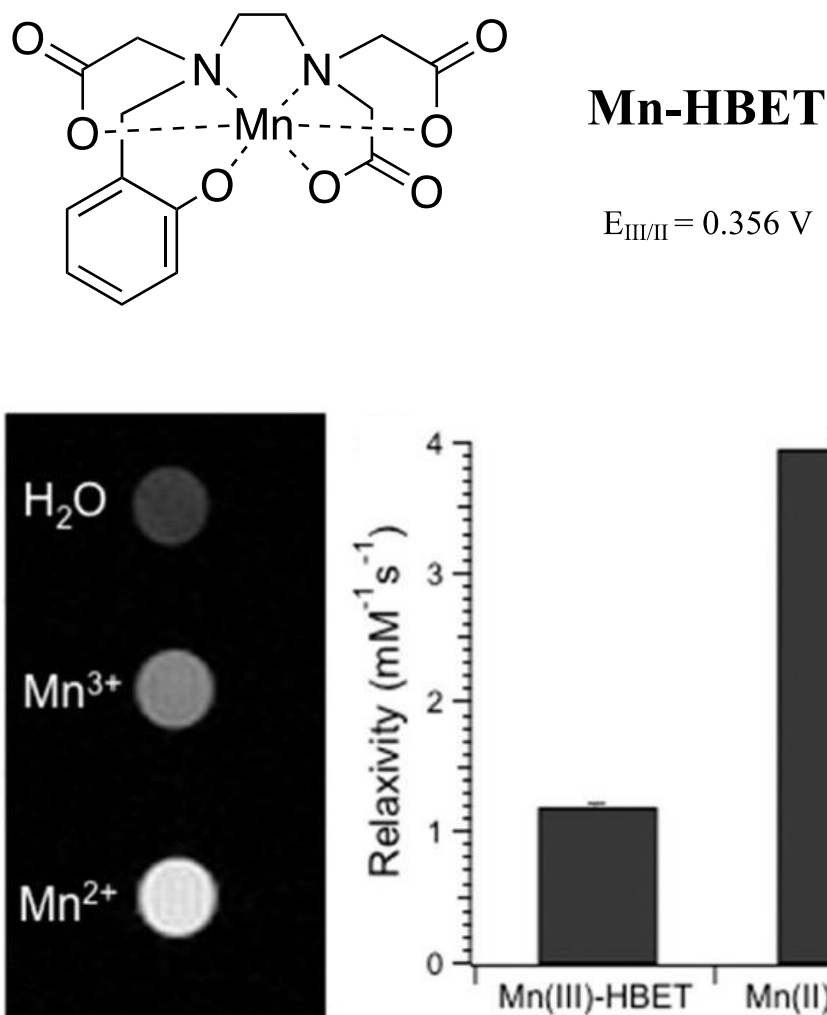
Figure A.4.1. Structure of Mn-HBET. The HBET ligand forms stable complexes with Mn(II) and Mn(III), and Mn(III/II)-HBET has a redox potential in the biologically relevant window, thus making it a promising redox-activatable MR contrast agent. The Caravan Lab demonstrated that Mn(III)-HBET has a low relaxivity of ~1.2 $mM^{-1}s^{-1}$ whereas Mn(II)-HBET has a significantly higher relaxivity of ~4 $mM^{-1}s^{-1}$, a >300% turn-on response. Figure adapted from ref 2.

We believe Mn-HBET is ideally suited to be used with a Pt(IV) prodrug to develop a theranostic platform. The Mn(III/II)-Pt(IV/II) theranostic will provide turn-on therapy as well as turn-on MR contrast enhancement. Our prior work has demonstrated the utility of Gd(III)-Pt(IV) theranostic agents, and this Mn(III)-Pt(IV) agent has the added benefit of reporting on the reduction event via MR contrast enhancement.[10] In other words, the Gd(III)-Pt(IV) agent shows where the agent is in the body, but the Mn(III)-Pt(IV) agent will show exactly when the active Pt(II) drug is released (Scheme A.4.1.)
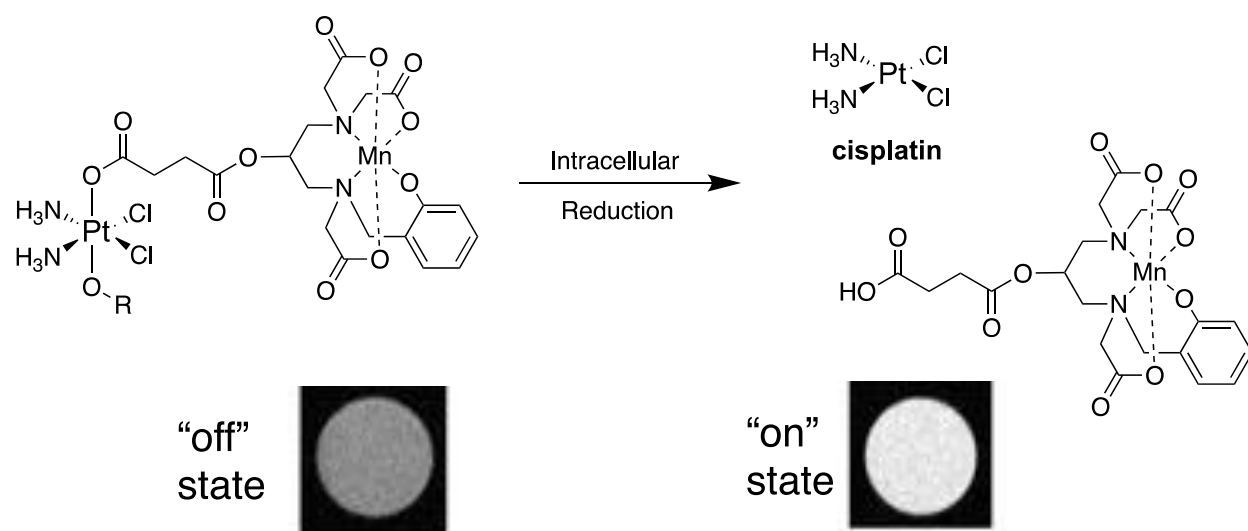
Scheme A.4.1. Proposed Mn(III/II)-Pt(IV/II) theranostic agent. The agent will undergo intracellular reduction (or reduction in the tumor microenvironment) to produce cisplatin and a higher relaxivity Mn(II) complex.

A.4.2 Preliminary Results

The Mn-HBET complex developed in the Caravan Lab lacks a functional handle through which the complex can be coupled to a Pt(IV) prodrug. Therefore, we designed a slightly modified version of the complex that has a hydroxyl group on the ligand backbone (Scheme A.4.2.) Using the available hydroxyl group, we will couple the Mn complex to a Pt(IV) prodrug to synthesize the Mn-Pt agent, **MP1**. Thus far, we have been able to synthesize the Mn(III) complex (**6**). Synthetic procedures for the reactions completed to date are listed below.
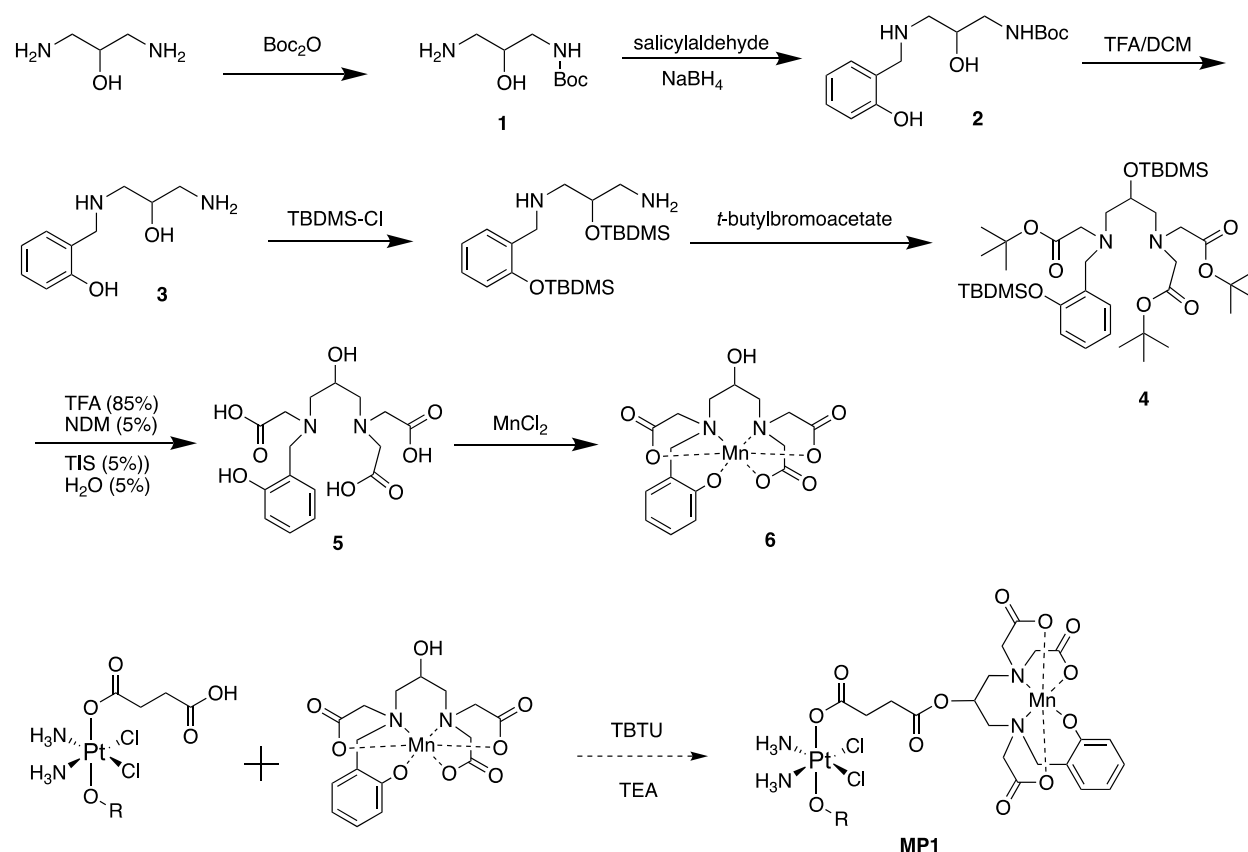
Scheme A.4.2. Proposed synthetic scheme of **MP1**, a Mn(III/II)-Pt(IV/II) theranostic agent. The agent will be synthesized by coupling a Mn complex (**6**) with a Pt(IV) prodrug. Solid synthetic arrows indicate steps that have been completed, whereas dashed lines are planned synthetic steps.

t*ert-butyl (3-amino-2-hydroxypropyl)carbamate*, **1**.

5 grams of 1,3-diamino-2-propanol (0.0555 mol) was dissolved in 100 mL of MeOH and 12.11 grams Di-tert-butyl decarbonate (0.02775 mol) was dissolved in 25 mL MeOH. The Di-tert-butyl solution was added to the 1,3-diamino-2-propanol and stirred at room temperature for 24 hours. The solvent was removed under reduced pressure. The crude product was dissolved in saturated NaCl H_2O solution and subsequently acidified to pH of 5 using 1 M HCl and washed with DCM (3 x 50 mL). The aqueous fraction was basified to pH of 12 using 1 M NaOH and the product was extracted using chloroform (5 x 100 mL) and dried over $NaSO_4$. The solvent was evaporated under reduced pressure yielding a white solid (2.5262 g, 22.85%), which was used in the next step without further purification.

ESI-MS m/z observed: 190.83, 212.85, 381.05; calculated: 191.13 [M + H]+, 213.13 [M+Na]+, 381.26 [2M+H]+.

tert-Butyl (2-((2-hydroxybenzyl)amino)2-hydroxypropyl)carbamate, **2**.

2.5262 grams of **1** (0.0133 mol) was dissolved in 100 mL^2 of MeOH. To this solution, 1.7037 grams/1.46 mL of salicylaldehyde (0.0140 mol) wad added and resulted in color change to yellow. After 1 hour of stirring at room temperature, 0.5026 gram of $NaBH_4$ (0.0133 mol) was added. Gas evolution was observed, and the solution changed from yellow to colorless. The reaction stirred at room temperature for 24 hours and the solvent was removed under reduced pressure. The crude product was dissolved in 100 mL DCM and washed with saturated $NaHCO_3$ H_2O solution (1 x 100 mL). The aqueous fraction was washed with DCM (2 x100 mL). All the DCM fractions were combined and washed with saturated NaCl H_2O solution (1 x 100 mL) and subsequently dried over $NaSO_4$. The solvent was evaporated under reduced pressure yielding a

yellow oil/white solid. The product was further purified with a silica column (eluant 19:1 DCM/MeOH, ramped up to 9:1 DCM/MeOH). This yielded a white solid (2.299 grams, 48.58%).

^{1}H NMR (500 MHz, CDCl3) δ (ppm): 7.14 (t, J = 7.75 Hz, 1 H), 6.97 (d, J = 5.65, 1H), 6.80 (d, J = 8.15 Hz, 1H), 6.76 (t, J = 7.4 Hz, 1H), 3.99 (q, J = 13.85 Hz, 1H), 3.89-3.85 (m, 1H), 3.25-3.16 (m, 2H), 2.70-2.60 (m, 2H)

ESI-MS m/z observed: 296.98; calculated: 297.17 [M+H]+

2-(((3-amino-2-hydroxypropyl)amino)methyl)phenol, **3**.

2.299 grams of **2** was dissolved in 25 mL of DCM. To this solution, 25 mL of trifluoroacetic acid was added, resulting in gas formation. The solution slowly changed from colorless to slight yellow to deep red. After 4 hours of stirring at room temperature, the solvent was removed under reduced pressure, yielding a red oil. The crude product was dissolved in 40 mL of H_2O and washed with ether (3 x 40 mL). The aqueous fraction was lyophilized forming a white solid (3.19 g assumed 100% yield), which was used in the next reaction with no further purification.

ESI-MS m/z observed: 425.24; calculated: 425.16 [M+H]+

- TFA salt version (196.12 + 114.02 +114.02)

di-*tert*-butyl 2,2'-((3-((2-(*tert*-butoxy)-2-oxoethyl)(2-((*tert*butyldimethylsilyl)oxy)benzyl)amino)-2-((*tert*-butyldimethylsilyl)oxy)propyl)azanediyl)diacetate, **4**.

Under the flow of nitrogen gas, 3.19 grams of **3** (0.00752 mol of protonated TFA salt version) were dissolved in 50 mL of DCM and the solution was cooled to 0°C in an ice bath. 7.87 mL of N, N-diisopropylethylamine (0.0452 mol) was added to the solution. Subsequently, grams

tert-butyldimethylsilyl chloride (0.0226 mol) was added and the solution was stirred for 5 hours as it returned to room temperature. The solution was cooled to 0°C in an ice bath and followed by the dropwise addition of 5.56 mL of tert-butyl bromoacetate (0.0376 mol) under nitrogen flow. Following 18 hours of stirring, the solution was diluted with DCM (200 mL) and washed with saturated $NaHCO_3$ (3 x 200 mL) and saturated NaCl (1 x 200 mL). The DCM fraction was collected and dried with $NaSO_4$ and the solvent was removed under vacuum, yielding a yellow oil. The crude oil was further purified using a silica column, yielding a colorless oil (1.4754 grams, 25.56%).

ESI-MS m/z observed: 767.60; calculated 767.50 [M+H]+

2,2'-((3-((carboxymethyl)(2-hydroxybenzyl)amino)-2-hydroxypropyl)azanediyl)diacetic acid, **5**.

4 (1.4754 g, 0.00192 mol) was dissolved in 40 mL of in trifluoracetic acid. 2.35 mL of each triisopropylsilane, 1-dodecanethiol, and water were subsequently added (85:5:5:5 solution). The reaction was stirred at room temperature for 5 hours and the solvent was removed under reduced pressure. The crude product was dissolved in water and washed with ether (3 x 40 mL). The aqueous fraction was lyophilized forming **5** as a powder, which was used in the next reaction with no further purification.

Mn(III)-2,2'-((3-((carboxymethyl)(2-hydroxybenzyl)amino)-2-hydroxypropyl)azanediyl)diacetic acid, **6**.

10 mg (0.027 mmol) of **5** was dissolved in 1 mL of water. The pH was adjusted to 8 using 0.1 M NaOH solution. $MnCl_2$ tetrahydrate (0.03 mmol, 6 mg) was added to the solution and the

pH was adjusted to 12. The solution was stirred for 1 h and was then filtered through a 0.2 µm filter. The pH was adjusted to 11 and the solution was stirred for an additional 18 h. The reaction was checked by analytical HPLC-MS in water/acetonitrile with 0.1% NH4OH using a 20 minute ramp from 0-100% acetonitrile. The presence of **6** was confirmed, but the crude product was not purified.
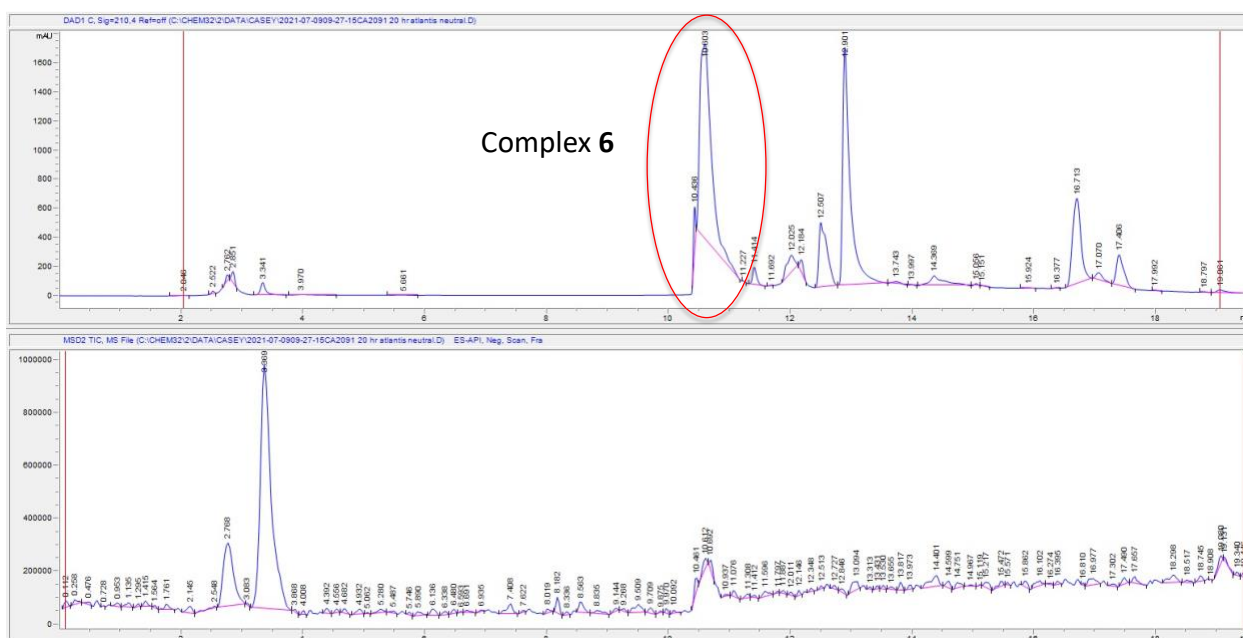
Figure A.4.2. Analytical HPLC trace (top) and corresponding ESI-MS spectrum (bottom) showing the presence of complex **6** during the metalation reaction. The complex will next be purified using preparatory HPLC.

A.4.3 Conclusions and Future Directions

A Mn(III) complex (**6**) has been synthesized but not yet purified. The complex will be purified by preparatory HPLC and characterized to ensure it behaves similarly to Mn-HBET. Complex **6** will then be coupled to a Pt(IV) prodrug, which will be synthesized following literature protocols. Once the final complex (**MP1**) is synthesized and purified, it will be characterized by measuring the redox potential of both the Mn and Pt complexes. The relaxivity of the agent will be measured before and after reduction to determine the MR turn-on response. Cell studies will be performed in cancer cell lines to determine the IC_{50} of the agent and the cellular accumulation, and *in vivo* experiments in mice will be performed to demonstrate the ability of the agent to provide simultaneous chemotherapy and contrast enhanced MR imaging.

A.4.4. References for Appendix 4

1.   Morrow, J. R., Modulating the Properties of Fe(III) Macrocyclic MRI Contrast Agents by Appending Sulfonate or Hydroxyl Groups. *Molecules* **2020,** *25* (10).

2.   Gale, E. M.; Atanasova, I. P.; Blasi, F.; Ay, I.; Caravan, P., A Manganese Alternative to Gadolinium for MRI Contrast. *Journal of the American Chemical Society* **2015,** *137* (49), 15548-15557.

3.   Kálmán, F. K.; Nagy, V.; Váradi, B.; Garda, Z.; Molnár, E.; Trencsényi, G.; Kiss, J.; Même, S.; Même, W.; Tóth, É.; Tircsó, G., Mn(II)-Based MRI Contrast Agent Candidate for Vascular Imaging. *J Med Chem* **2020,** *63* (11), 6057-6065.

4.   Loving, G. S.; Mukherjee, S.; Caravan, P., Redox-activated manganese-based MR contrast agent. *J Am Chem Soc* **2013,** *135* (12), 4620-3.

5.   Snyder, E. M.; Asik, D.; Abozeid, S. M.; Burgio, A.; Bateman, G.; Turowski, S. G.; Spernyak, J. A.; Morrow, J. R., A Class of FeIII Macrocyclic Complexes with Alcohol Donor Groups as Effective T1 MRI Contrast Agents. *Angewandte Chemie International Edition* **2020,** *59* (6), 2414-2419.

6.   Wang, H.; Jordan, V. C.; Ramsay, I. A.; Sojoodi, M.; Fuchs, B. C.; Tanabe, K. K.; Caravan, P.; Gale, E. M., Molecular Magnetic Resonance Imaging Using a Redox-Active Iron Complex. *Journal of the American Chemical Society* **2019,** *141* (14), 5916-5925.

7.   Wang, J.; Wang, H.; Ramsay, I. A.; Erstad, D. J.; Fuchs, B. C.; Tanabe, K. K.; Caravan, P.; Gale, E. M., Manganese-Based Contrast Agents for Magnetic Resonance Imaging of Liver Tumors: Structure–Activity Relationships and Lead Candidate Evaluation. *Journal of Medicinal Chemistry* **2018,** *61* (19), 8811-8824.

8.   Han, G.; Deng, Y.; Sun, J.; Ling, J.; Shen, Z., Research into europium complexes as magnetic resonance imaging contrast agents (Review). *Exp Ther Med* **2015,** *9* (5), 1561-1566.

9.   Gale, E. M.; Mukherjee, S.; Liu, C.; Loving, G. S.; Caravan, P., Structure–Redox–Relaxivity Relationships for Redox Responsive Manganese-Based Magnetic Resonance Imaging Probes. *Inorganic Chemistry* **2014,** *53* (19), 10748-10761.

10.   Adams, C. J.; Meade, T. J., Gd(iii)–Pt(iv) theranostic contrast agents for tandem MR imaging and chemotherapy. *Chemical Science* **2020,** *11* (9), 2524-2530.

CASEY J. ADAMS

833 N. Clark St, Chicago, IL 60610
caseyadams2022@u.northwestern.edu
Phone: 978-319-2612

Education:

Sep 2017-Present	Northwestern University (NU) PhD Candidate in Chemistry Principal Investigator: Thomas J. Meade GPA: 3.97
Dec 2016	College of the Holy Cross (HC) BA in Chemistry (Departmental Honors) GPA: 3.97 (Summa Cum Laude)

Awards and Fellowships:

May 2019-Present	Ruth L. Kirschstein National Research Service Award (NIH NRSA F31 Fellowship) "*Development of Gd(III)-Pt(II) MR Probes for Tandem* *Detection and Chemotherapy*"
Mar 2020	Alumnae of Northwestern University Grant "*Development of Gd(III)-Pt(II) MRI Contrast Agents for* *Predicting Tumor Response to Pt(II) Chemotherapy*"
Nov 2019	Joseph Lambert Phi Lambda Upsilon Award "*For outstanding achievement and promise in academic* *research*"
May 2017	American Institute of Chemists Foundation Award "*For a demonstrated record of ability, leadership, and* *professional promise*"
May 2015	American Chemical Society Award in Inorganic Chemistry

<u>Professional Development</u>:

Jun 2021-Aug 2021	<u>Summer Associate, ARCH Venture Partners</u> Responsible for sourcing and analyzing early-stage biopharmaceutical investment opportunities and engaging with founders and corporate partners
Jun 2021-Aug 2021	<u>Kellogg Business Certificate Program (NU)</u> Certificate program (by application) from the Kellogg School of Management covering topics in business, finance, management, and leadership
Jan 2021-May 2021	<u>Radyus Research Internship</u> Conducted market research, analyzed pre-clinical data, and developed/streamlined processes to aid Radyus clients with drug development plans for approval and marketing
Jan 2021-Jun 2021	<u>Venture Capital Intern, Gen 1 Capital</u> Met weekly to discuss topics in venture capital, conducted due diligence, and wrote white papers on technologies and markets for proposed Gen 1 investments
Oct 2020-Jun 2021	<u>Intern, NU Innovation & New Ventures Office (INVO)</u> Worked with Invention Managers to assess new technologies from NU for patentability, marketability, and commercial readiness. Worked with the New Ventures team to conduct due diligence and compile data rooms on startups associated with Northwestern
Apr 2021-Present	<u>Reviewer for *Chemical Science*</u> Peer-review submitted articles for *Chemical Science*, the flagship journal of the Royal Society of Chemistry
Jan 2021-Apr 2021	<u>One-on-One Leadership Coaching</u> Met with a leadership coach from Kellogg School of Management biweekly to develop strategies to become a more effective leader
Apr 2020	<u>Webinar Presentation, Lurie Cancer Center CAPS Program</u> *"Gadolinium and Platinum in Tandem: Theranostic Probes for MRI and Chemotherapy"*

Jan 2013-Mar 2019	<u>Teaching Assistant (NU, HC)</u>: General Chem., Advanced Laboratory, Inorganic Chem., Analytical Chem., Calculus 1
Sep 2016	<u>Summer Research Poster Symposium (HC)</u> *"Synthesis of Novel Artificial Siderophores for Development of ImmunoPET Imaging Probes"*

Publications:

(1) Casey J. Adams, Thomas J. Meade. "Towards Imaging Pt(II) Chemoresistance Using Gd(III)-Pt(II) Theranostic MR Contrast Agents" *ChemMedChem: Metals in Medicine*, **2021**.

(2) Casey J. Adams, Thomas J. Meade. "Imaging Bacteria with Contrast-Enhanced Magnetic Resonance" *Metal Ions in Life Sciences: Metal Ions in Bio-Imaging Techniques (A. Sigel, E. Freisinger and R. Sigel, Eds.)*, **2021**, *22*, 425-435.

(3) Casey J. Adams, Thomas J. Meade. "Gd(III)-Pt(IV) theranostic contrast agents for tandem MR imaging and chemotherapy" *Chem. Sci.* **2020**, *11*, 2524-2530.

(4) Casey J. Adams, Ruby Kreuger, Thomas J. Meade. "A Multimodal Ca(II) Responsive Near IR-MR Contrast Agent Exhibiting High Cellular Uptake" *ACS Chem. Biol.* **2020**, *15*, 334-341.

(5) Casey J. Adams, Justin J. Wilson, *Eszter Boros. "Multifunctional Desferrichrome Analogues as Versatile ^{89}Zr(IV) Chelators for ImmunoPET Probe Development." Mol. Pharmaceutics*. **2017**, *14*, 2831–2842.

(6) Daniel T. Yonemoto, Jeremiah M. Sears, Jessica M. Rimsza, Diana Perales, Nelson S. Bell, LaRico J. Treadwell, Peter Renehan, Casey J. Adams, Michael T. Bender, William Crowley, Joshua Farrell, Timothy J. Boyle. "Synthesis, Characterization, and Nanomaterials Generated from 6,6'-(((2-hydroxyethyl)azanediyl)bis(methylene)bis(2,4-di-tert-butylphenol) Modified Group 4 Metal Alkoxides." *Inorg. Chem.* **2018**, *57(17)*, 11264-11274.

Research Experience:

Sep 2017-Present	<u>Graduate Research</u> Location: Northwestern University Advisor: Prof. Thomas J. Meade

Jan-May 2017 & Summer 2016	<u>Research Assistant</u> Location: A. A. Martinos Center for Biomedical Imaging Massachusetts General Hospital/Harvard Medical School Advisors: Prof. Peter Caravan, Prof. Eszter Boros
Sep 2015-Dec 2016	<u>Undergraduate Research</u> Location: College of the Holy Cross Advisor: Prof. Joshua Farrell
Summer 2015	<u>Research Experience for Undergraduates (REU)</u> Location: Sandia National Laboratories Advisor: Dr. Timothy J. Boyle